

AD-A106 762

GENERAL DYNAMICS SAN DIEGO CA ELECTRONICS DIV

F/G 17/9

WAVE PROPAGATION THROUGH AXIALLY SYMMETRIC DIELECTRIC SHELLS.(U)

JUN 81 G TRICOLES, E L ROPE, R A HAYWARD

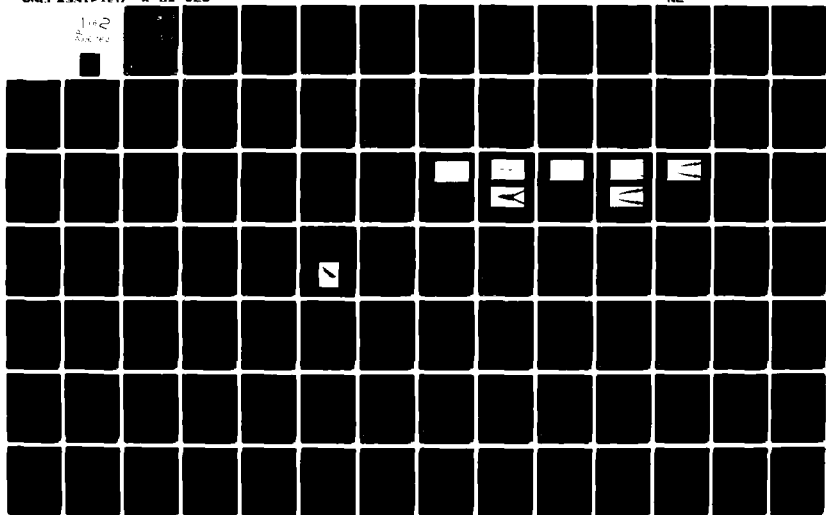
N00019-79-C-0638

R-81-125

NL

UNCLASSIFIED

1 of 2
AD-A106 762



AD A106762

Report No. R-81-125
June 1981

WAVE PROPAGATION
THROUGH
AXIALLY SYMMETRIC DIELECTRIC SHELLS

LEVEL II

12

Final Report

by

G. Tricoles, E.L. Rope, and R.A. Hayward

DTIC
ELECTE
NOV 04 1981
E

Prepared for U.S. Naval Air Systems Command

under

Contract No. N00019-79-C-0638

See 1473

APPROVED FOR PUBLIC RELEASE
DISTRIBUTION UNLIMITED

DTIC FILE COPY

GENERAL DYNAMICS
Electronics Division

81 11 02 211

Report No. R-81-125
June 1981

**WAVE PROPAGATION
THROUGH
AXIALLY SYMMETRIC DIELECTRIC SHELLS**

Final Report

by

G. Tricoles, E.L. Rope, and R.A. Hayward

Prepared for U.S. Naval Air Systems Command

under

Contract No. N00019-79-C-0638

**APPROVED FOR PUBLIC RELEASE
DISTRIBUTION UNLIMITED**

GENERAL DYNAMICS

Electronics Division

P.O. Box 81127, San Diego, California 92138 • 714-692-6111

Accession For	
NTIS GSA&I	<input checked="" type="checkbox"/>
DDIC T&B	<input type="checkbox"/>
Unannounced	<input type="checkbox"/>
Justification	
By	
Distribution/	
Availability Codes	
Dist	Avail and/or Special
A	

CONTENTS

<u>Section</u>		<u>Page</u>
INTRODUCTION		viii
SUMMARY		ix
1 GEOMETRIC DIFFRACTION THEORY FOR DIELECTRICS		1-1
1.1 Approach		1-1
1.2 Background: Analytical Methods Based on Flat Sheet Approximation		1-3
1.3 More Background: Examples of Transmittance for Axially Symmetric and Wedge Radomes		1-3
1.4 A Geometric Theory of Diffraction for Finite Dielectric Slabs		1-15
2 SCALAR GREEN'S FUNCTION FORMULATION		2-1
2.1 Integration of Maxwell's Equations		2-1
2.2 Simultaneous Algebraic Equations		2-4
2.3 Scattered Field for Diagonal Elements		2-8
2.3.1 Vector Potential		2-8
2.3.2 Scalar Potential		2-10
2.4 Scattered Field for Off Diagonal Elements		2-14
2.4.1 Vector Potential		2-14
2.4.2 Scalar Potential		2-14
2.5 External Fields		2-18
2.5.1 Measurement Average Internal Field		2-18
2.5.2 From Circumferentially Varying Internal Field		2-20
3 RESULTS FROM SCALAR GREEN'S FUNCTION METHOD		3-1
3.1 Cylinders		3-1
3.1.1 Internal Fields		3-1
3.1.2 External Field from Circumferentially Uniform Internal Fields		3-1
3.1.3 External Fields from Circumferentially Varying Internal Fields		3-6
3.1.4 Polarization Dependence of Internal Fields		3-6
3.2 Cone		3-12

CONTENTS (Continued)

<u>Section</u>		<u>Page</u>
4	MEASUREMENT	4-1
5	DISCUSSION	5-1
5.1	Cylinders	5-1
5.2	Cone	5-1
6	TENSOR GREEN'S FUNCTION FORMULATION	6-1
6.1	Integral Equation	6-1
6.2	Computational Technique	66
7	RESULTS FROM THE TENSOR GREEN'S FUNCTION FORMULATION ...	7-1
7.1	Rod	7-1
7.2	Ring	7-7
APPENDIX A - EQUIVALENCE OF TENSOR AND SCALAR FORMULATIONS ...		A-0
REFERENCES		R-1

ILLUSTRATIONS

<u>Figure</u>	<u>Title</u>	<u>Page</u>
1-1	Distorted Wavefront	1-2
1-2	Wave Mechanisms in Hollow Dielectric Shell	1-2
1-3	The Direct Ray Method	1-4
1-4	Surface Integration Method	1-4
1-5	Approximate Description of Radome at a Point by a Flat Sheet	1-5
1-6	The Variation in Direction of the Surface Normal \underline{N} Produces Transmittance That Depends on Position	1-6
1-7	Phase Delay for a Radome with Diameter 6.7 Wavelength and Length to Diameter Ratio 1.8	1-7
1-8	E-plane Boresight Error of 0.125 in. Thick Shell, Fineness Ratio 1.8, Dielectric Constant 2.5	1-8
1-9	H-plane Boresight Error of 0.125 in. Thick Shell, Fineness Ratio 1.8, Dielectric Constant 2.5	1-9
1-10	Phase Delay and Power Transmittance for Pointed Radome, Length to Diameter Ratio 1.8, Thickness: 0.125 in. Frequency: 12 GHz; E-plane; Gimbal Angle: 16°	1-10
1-11	Phase Delay and Power Transmittance for Pointed Radome, Length to Diameter Ratio 1.8	1-11
1-12	Power Transmittance at 12 GHz for a Radome with Dielectric Constant 2.6	1-12
1-13	Transmittance, from Figure 1-12 at End Points of Scans	1-13
1-14	H-plane Transmittance for a Ceramic Radome at Frequency 20% Above That for Which the Thickness is a Half Wave	1-14
1-15	E-plane Transmittance of a Curved Wall Wedge, Thickness 0.315" at 12 GHz	1-16
1-16	Computed H-plane Transmittance for a 0.25" Thick Wedge with Dielectric Constant 2.5 at 12 GHz	1-17
1-17	Coordinates for a Slab	1-18
1-18	Total Field Intensity in Slab for Grazing Incidence	1-19
1-19	Measured Intensity Near Slab	1-20
1-20	Scattered Field Magnitude Near Slab Computed by Moment Method	1-22
1-21	Computed Decay of Guided Wave Amplitude for Slab	1-23
1-22	Phase Increment for Grazing Incidence on Dielectric Slab Computed with Moment Method	1-24
1-23	Computed Scattered Field Phase Contrours Near 1/4 in. Thick, 10 in. Wide Slab with $\kappa = 2.6$; Wavelength: 1.26"	1-25
1-24	Computed Intensity in Field Scattered by Slab	1-26
1-25	Phase of Total Field for Slab	1-27
1-26	Intensity of Total Field for Slab	1-28
1-27	Computed Loci of Constructive Interference	1-29
1-28	Fields Near a Slab for Y Equal 5 in.	1-30
1-29	Computed Phases of Scattered Fields	1-31

ILLUSTRATIONS (Continued)

<u>Figure</u>	<u>Title</u>	<u>Page</u>
1-30	Constituent Fields Near a Slab for Grazing Incidence	1-31
2-1	Dielectric Ring and Coordinate System	2-5
2-2	Subdivision of Hollow Cylinder Into Rings	2-5
2-3	Coordinates for a Cell	2-6
2-4	Hollow Cone Composed of Rings	2-6
2-5	Dimensions of Rings	2-7
3-1	Phase and Amplitude of E^T for Single Ring	3-1
3-2	Phase and Amplitude of E^T for Two Rings	3-2
3-3	Total Field Behind Dielectric Ring	3-3
3-4	Total Field Outside Dielectric Ring	3-4
3-5	As in Figure 3-4 but with $\delta\rho$ Reduced by 20 Percent	3-5
3-6	Total Field Intensity for a Ring	36
3-7	Total Field Phase for a Ring like that in Figure 3-6	3-7
3-8	As in Figure 3-6 but $z = 0.75\lambda$	3-7
3-9	As in Figure 3-7 but $z = 0.75\lambda$	3-8
3-10	As in Figure 3-6, but $z = \lambda$	3-8
3-11	As in Figure 3-7 but $z = \lambda$	3-9
3-12	Total Field Phase for a Cylinder Composed of Two Rings	3-9
3-13	Total Field Intensity for a Cylinder Composed of Two Rings	3-10
3-14	As in 3-12, but $z = \lambda$	3-10
3-15	As in Figure 3-13, but $z = \lambda$	3-11
3-16	Total Field Behind Dielectric Ring with Dimensions Given in Figure 3-6	3-11
3-17	Computed Internal Values of $ E^T ^2$ for 1 and 2 Rings	3-12
3-18	Computed $ E^T ^2$ inside conical shell	3-13
3-19	Computed Internal Field Intensity for Another Subdivision of Three Smallest Rings	3-15
3-20	$ E^T ^2$ at Z One Half Wavelength Behind Largest Ring	3-16
4-1	Phase and Intensity Measured in Plane of 12th Ring, $z = 0.86\lambda$ for 13-ring core	4-2
7-1	Dielectric Rod as Approximated by 15 Dielectric Spheres	7-1
7-2	Computed Internal Field Intensity for the Dielectric Rod of Figure 7-1	7-2
7-3	Computed Internal Field Phase for the Dielectric Rod of Figure 7-1	7-2
7-4	Total Field Intensity for the Dielectric Rod of Figure 7-1 for E^I Parallel to Rod and $x = .5\lambda$	7-3
7-5	Total Field Phase for the Dielectric Rod of Figure 7-1 for E^I Parallel to Rod and $x = .5\lambda$	7-3
7-6	As in Figure 7-4, but $x = 1.5\lambda$	7-4
7-7	As in Figure 7-5, but $x = 1.5\lambda$	7-4
7-8	As in Figure 7-4, but E^I Perpendicular to Rod	7-5

ILLUSTRATIONS (Continued)

<u>Figure</u>	<u>Title</u>	<u>Page</u>
7-9	As in Figure 7-5, but E^I Perpendicular to Rod	7-5
7-10	As in Figure 7-4, but E^I Perpendicular to Rod and $x = 1.5 \lambda$	7-6
7-11	As in Figure 7-5, but E^I Perpendicular to Rod and $x = 1.5 \lambda$	7-6
7-12	Dielectric Ring (as in Figure 2-1)	7-7
7-13	Computed Internal Field Intensity as a Function of Azimuth for the Dielectric Ring of Figure 7-12	7-8
7-14	Computed Internal Field Phase as a Function of Azimuth for the Dielectric Ring of Figure 7-12	7-8
7-15	Total Field Intensity Behind Dielectric Ring	7-9
7-16	Total Field Phase Behind Dielectric Ring	7-9

TABLES

<u>Table</u>	<u>Title</u>	<u>Page</u>
1-1	Constituent Waves	1-29
3-1	Computational Parameters	3-12

INTRODUCTION

Radomes significantly reduce missile guidance accuracy by producing boresight error (BSE), an error in target direction as determined by a seeker or radar system. Despite decades of development and use, radomes are a problem because newer missiles require small angular rates of change of BSE and because newer seekers have greater frequency bandwidths. The electromagnetic design process, for boresight error and bandwidth, is largely empirical because radome shapes are non-separable, making analysis approximate. The need for improving radome performance motivates efforts to improve analytical methods.

The purpose of the research is to develop improved methods for analyzing radome electromagnetic effects. The main goals are as follows:

1. Develop a geometric theory of diffraction (GTD) for dielectrics and in particular hollow dielectric shells
2. Extend the moment method for use with hollow dielectric shells.

The GTD is intended to be relatively simple, and the moment method is intended to be accurate although more complex than the GTD.

SUMMARY

Section 1 reviews the concept of transmittance, the complex-valued wave distribution in a radome bounded volume, and give measured and computed values of transmittance for pointed, axially-symmetric radomes and for wedge radomes. The transmittance has intensity variations that are not described by analytical methods that utilize a flat sheet transmittance to locally approximate the radome. These flat sheet methods omit wave mechanisms, namely guided waves and vertex scattering. To quantify these mechanisms the moment method was applied to a finite slab for grazing incidence. We postulated guided waves and waves scattered by a slab edge. The amplitudes and phases of these waves were determined by interpreting maxima and minima computed by the moment method in terms of the postulated waves. Thus we have solved numerically a canonical problem for a geometric diffraction theory of dielectrics.

Section 2 extends the moment method to a hollow cone with a scalar Green's function approach, and Section 3 gives numerical results. Section 4 gives measured results for a hollow cone. Section 5 compares the numerical and computed results. Agreement is generally good. The shapes of measured and computed curves agree, but the maximum phase is somewhat in error. Polarization dependence is correct. The formulation decomposes the cone into cells that are sectors of annuli. This decomposition utilizes to advantage the constant values of fields in a cell.

Section 6 describes a tensor Green's function formulation for a hollow cone. The cells are spheres. This decomposition treats polarization more simply than does the annular. Section 7 compares measured and computed results for a rod and a ring.

Appendix A shows the theoretical equivalence of the two formulations.

During the coming year we plan to test further the two formulations for off-axis incidence on hollow dielectric wedges and on hollow dielectric cones. Numerical data will be generated for cover^{ed} and tested against measured values. The numerical data will be interpreted to develop geometric diffraction theory for hollow cones, which approximate radomes.

1. GEOMETRIC DIFFRACTION THEORY FOR DIELECTRICS

1.1 APPROACH

The central concept is the wavefront distribution, of phase and intensity, produced in a radome-bounded region by an externally incident plane wave. This distribution, called the transmittance T , depends on incidence direction, wavelength, and polarization, and the radome configuration and composition. The transmittance strongly influences the output voltages of an antenna enclosed by a radome. Physically, the phase variations of T are aberrations; in fact, wavefront tilts are, to a first approximation, proportional to boresight error.¹ Figure 1-1 suggests aberrations. Analytically, the transmittance T is a function that is a factor in the integrand of a diffraction integral for the patterns of an enclosed antenna. The quantities that are measured with an antenna are intensity $|E_R|^2$ and phase, $\arg E_R$, where E_R is a rectangular field component

$$E_R = TE^I F dA,$$

where E^I is the incident field component, F is the receiving near-field distribution, and the integration is over the region such that F is non-negligible.

The transmittance T helps in radome development. For externally incident waves, nearfield values of T directly link boresight error (via wavefront tilts) and the radome shape and its thickness variations. Thickness variations and shape modifications are limited in extent, but they are the main parameters available for design. The link provided by T is more direct than that between boresight error and farfield patterns because diffraction smooths phase variations. Of course, farfield patterns are significant for missile performance; in fact, boresight error and aberrations were related analytically through polynomial expansions of T in diffraction integrals.¹

We approach a GTD for T by measuring and computing transmittance near hollow dielectric shells, hollow wedges, and a flat slab. A slab is an idealized model of half of an axially-symmetric radome for high incidence angles. We seek to decompose the complicated transmittance into a sum of simpler, constituent waves, as in Figure 1-2. Identifying constituent waves and estimating their magnitudes and phases generates conical solutions, an important part of GTD. The measurements are done with a small, scanning probe antenna. The calculations are done by two radome analysis methods, one a direct ray method and the other a surface integration; in addition, we apply the moment method for infinitely long cylinders.²

The approach to the second goal, extending the moment method, is to analyze a hollow cone. Two formulations are used. One uses a scalar Green's function; the other a tensor Green's function. The two are equivalent, but the numerical procedures differ. The scalar Green's function method decomposes the cone into circular cylinders and decomposes the cylinders into angular sectors. The tensor Green's function method decomposes the cone into spheres. The formulations differ in two practical ways. One is in the number of cells because of cell size. The other difference involves polarization dependence.

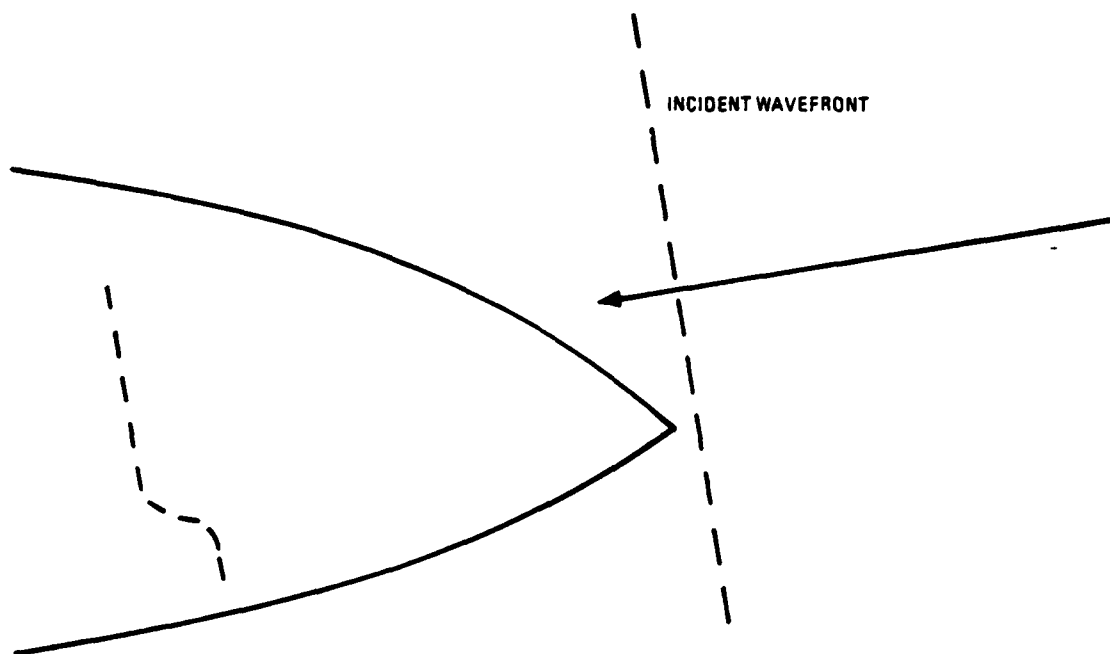
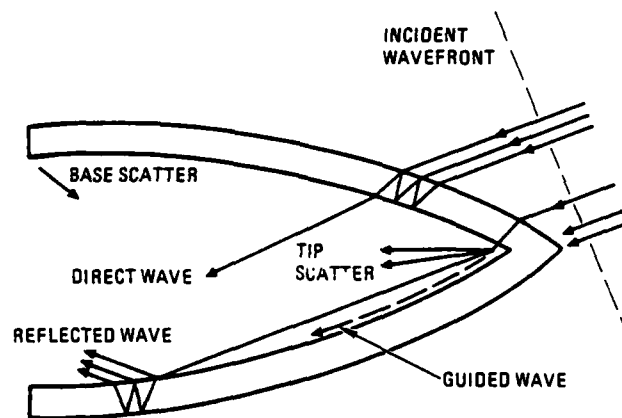


Figure 1-1. Distorted Wavefront



FL027

Figure 1-2. Wave Mechanisms in Hollow Dielectric Shell. The Fields Near a Radome Consist of Constituent Waves.

1.2 BACKGROUND: ANALYTICAL METHODS BASED ON FLAT SHEET APPROXIMATION

A simple way to analyze radomes is sketched in Figure 1-3. This direct ray method associates a single incident wave normal (ray) with a point on the receiving aperture. The method is adequate for designing radomes big enough to enclose an antenna that is an order of magnitude larger than the wavelength, provided the aperture also is considerably larger than the wavelength. However this method fails for smaller antennas and radomes; in these cases, a surface integration approach has been successful.³ Figure 1-4 suggests surface integration, which can be interpreted in terms of rays converging to an aperture point.

In both the direct ray and surface integration methods the transmittance for each ray is approximated by the values for a plane sheet that locally approximates the curved radome, as in Figure 1-5. Surface integration more densely samples the variation of the surface normal direction. Figure 1-6 shows the variation in the normal. For the simplest case of axial incidence, a converging set of rays spanning the tip has transmittance that is a sum of terms with distinct individual transmittance. One term arises from each converging ray in Figure 1-4. The value of each term depends on the direction of the surface normal for the associated ray because the normal direction determines the angle between it and the field and thus the resolution of the field into parallel and perpendicular components. The direct ray method sparsely samples the variation of the surface normal direction, but dense sampling is significant near the radome tip where the normal varies rapidly.

Note that transmittance depends on position within the radome. Figure 1-6 suggests how this variation occurs. On the Y-axis a direct ray projected from the radome gives the transmittance value for parallel polarization, and on the X-axis it gives the value for perpendicular polarization. The variation with position requires surface integration to describe accurately the mixture of terms.

In addition to position dependent polarization variation relative to the surface normal for fixed polarization direction, another variation occurs when the field orientation is changed from horizontal to vertical. Consider Figure 1-7 which compares measured phase with values computed by the direct and surface integration methods for off-axis-incidence. It shows that surface integration is more accurate than the direct ray method. It also suggests how a polarization change influences transmittance, even for a fixed point in the volume bounded by the radome.

1.3 MORE BACKGROUND: EXAMPLES OF TRANSMITTANCE FOR AXIALLY SYMMETRIC AND WEDGE RADOMES

Although Figure 1-7 and the results in Reference 3 suggest that surface integration is more accurate than the direct ray method, these results are for radomes that were, to a good approximation, a half wave thick. For wide frequency bands, surface integration, as described in Figure 1-4, also has limited accuracy. To illustrate this point, Figures 1-8 and 1-9 show boresight error of a radome with thickness 0.125 in. for frequencies from 8 GHz to 18 GHz. The antenna was an array of two horns. For 8-12 GHz each horn aperture was 1.95 in. by 1.7 in. The results show rather small

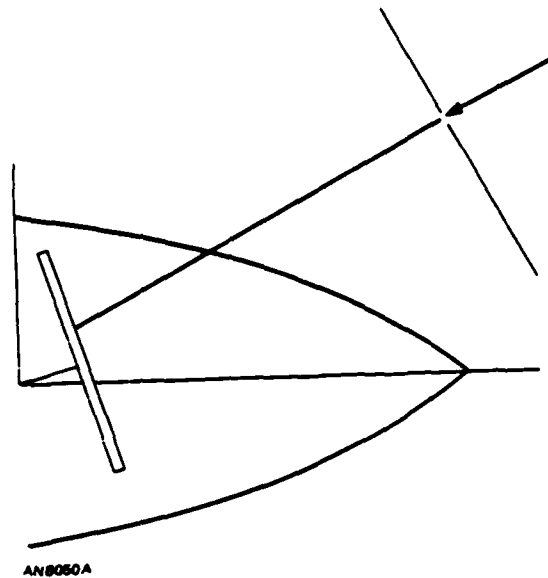


Figure 1-3. The Direct Ray Method. A Single Incident Wave Normal (or Ray) is Associated with a Point on the Receiving Aperture. The Radome is a Surface of Revolution, but only a Plane is Sketched.

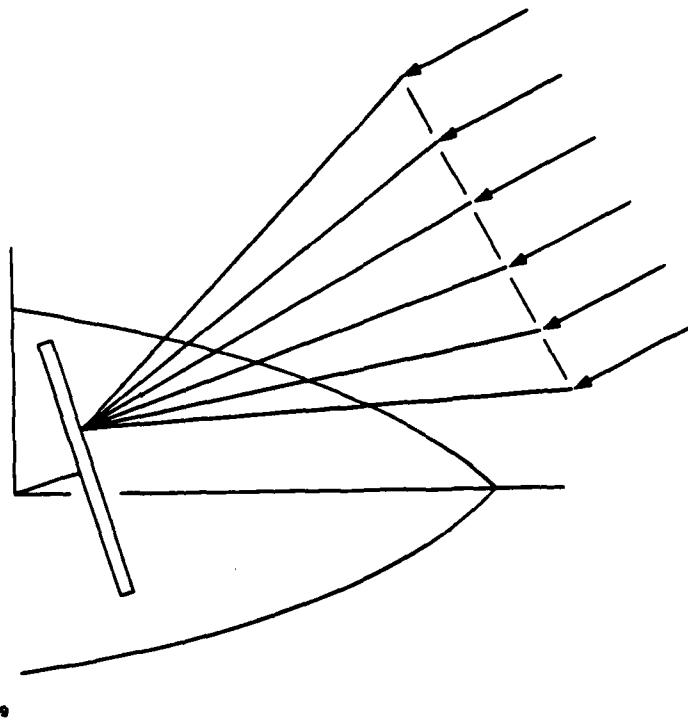


Figure 1-4. Surface Integration Method. The Radome is a Surface of Revolution. Integration is over a Portion of the Incident Wavefront.

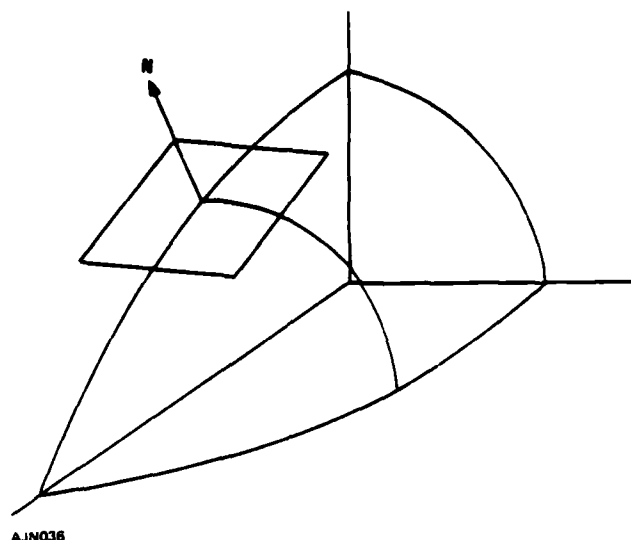


Figure 1-5. Approximate Description of Radome at a Point by a Flat Sheet.
Multiple Internal Reflections are Included.

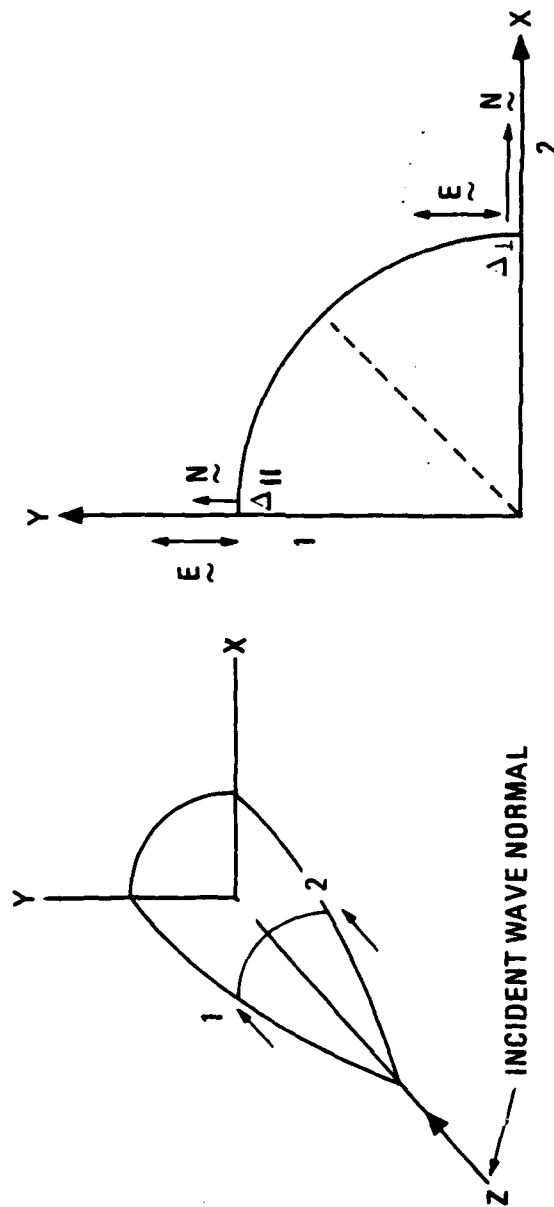
discrepancies for some frequencies but larger discrepancies at other frequencies. For example in Figure 1-8, for the E-plane, frequency 12 GHz, and gimbal angle -16° the discrepancy is 0.3° . The discrepancies for 10 and 14 GHz are smaller for the same angle, but they are larger for 8 GHz.

To understand the discrepancies in boresight error, we have compared measured and computed transmittance values for the radome of Figures 1-8 and 1-9. Figure 1-10 shows an example, for 12 GHz, 16° gimbal angle, and the E-plane. The point of this figure is that it illustrates the magnitudes of transmittance discrepancies (in Figure 1-10) that correspond to those of boresight error in Figure 1-8.

We also considered another radome, with thickness tapered between 0.45 in. and 0.40 in. This thickness is a half-wave wall at 10 GHz, but it is 20 percent greater at 12 GHz. Calculated and measured transmittance values for an axial position that would be occupied by an aperture are shown in Figure 1-11. Consider two horns centered at $X = \pm\lambda$. The phase difference between these two points is greater in Figure 1-11 than in Figure 1-10. Therefore boresight error discrepancies should be larger than for the case of Figure 1-10, and boresight error measurements have verified this expectation.

To study this radome (of Figure 1-11) further, we measured the transmittance through the radome enclosed volume. Figure 1-12 shows power transmittance (intensity) for 16° gimbal angle.

This graph shows transmittance variations between +1 dB and -4 dB. An antenna would be illuminated by a wave that is non-uniform.



AJN037

Figure 1-6. The Variation in Direction of the Surface Normal \vec{N} Produces Transmittance That Depends on Position. Even for a Fixed Incident Polarization, the Transmittance Varies with the Normal Direction from Parallel to Perpendicular.

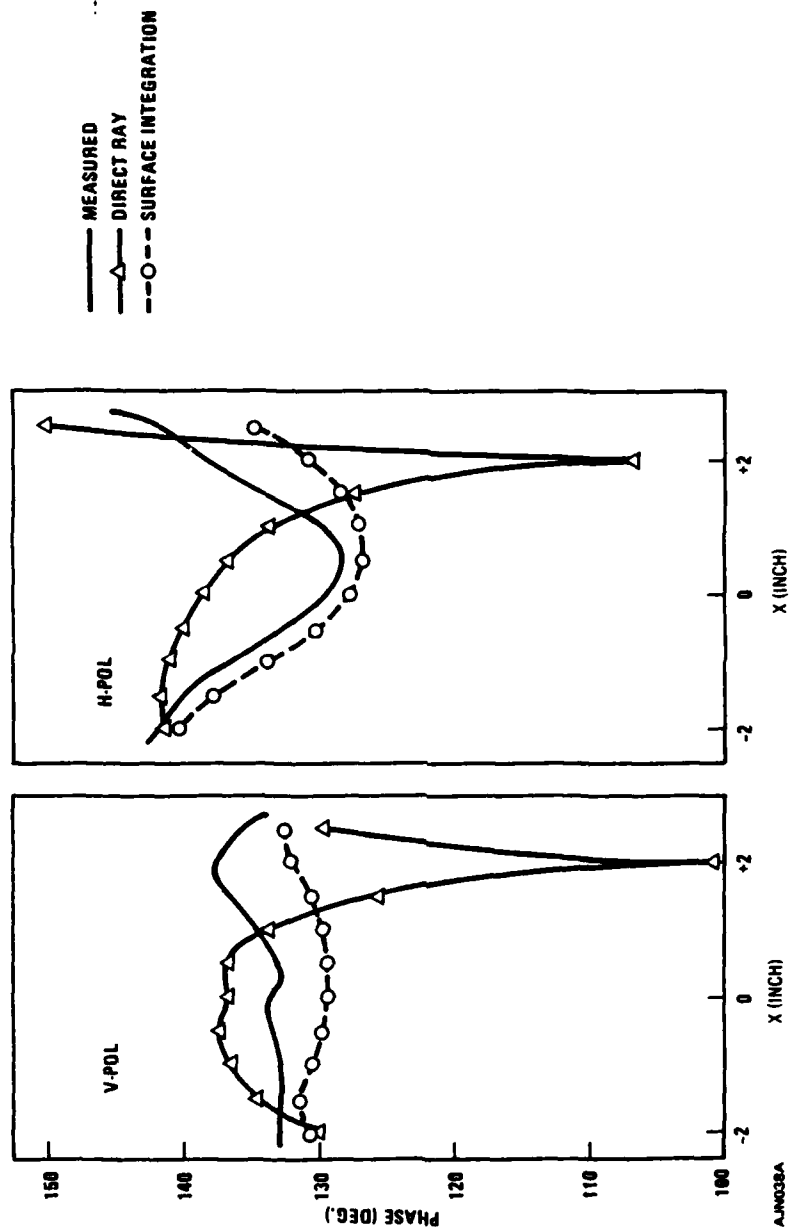


Figure 1-7. Phase Delay for a Radome with Diameter 6.7 Wavelength and Length to Diameter Ratio 1.8.

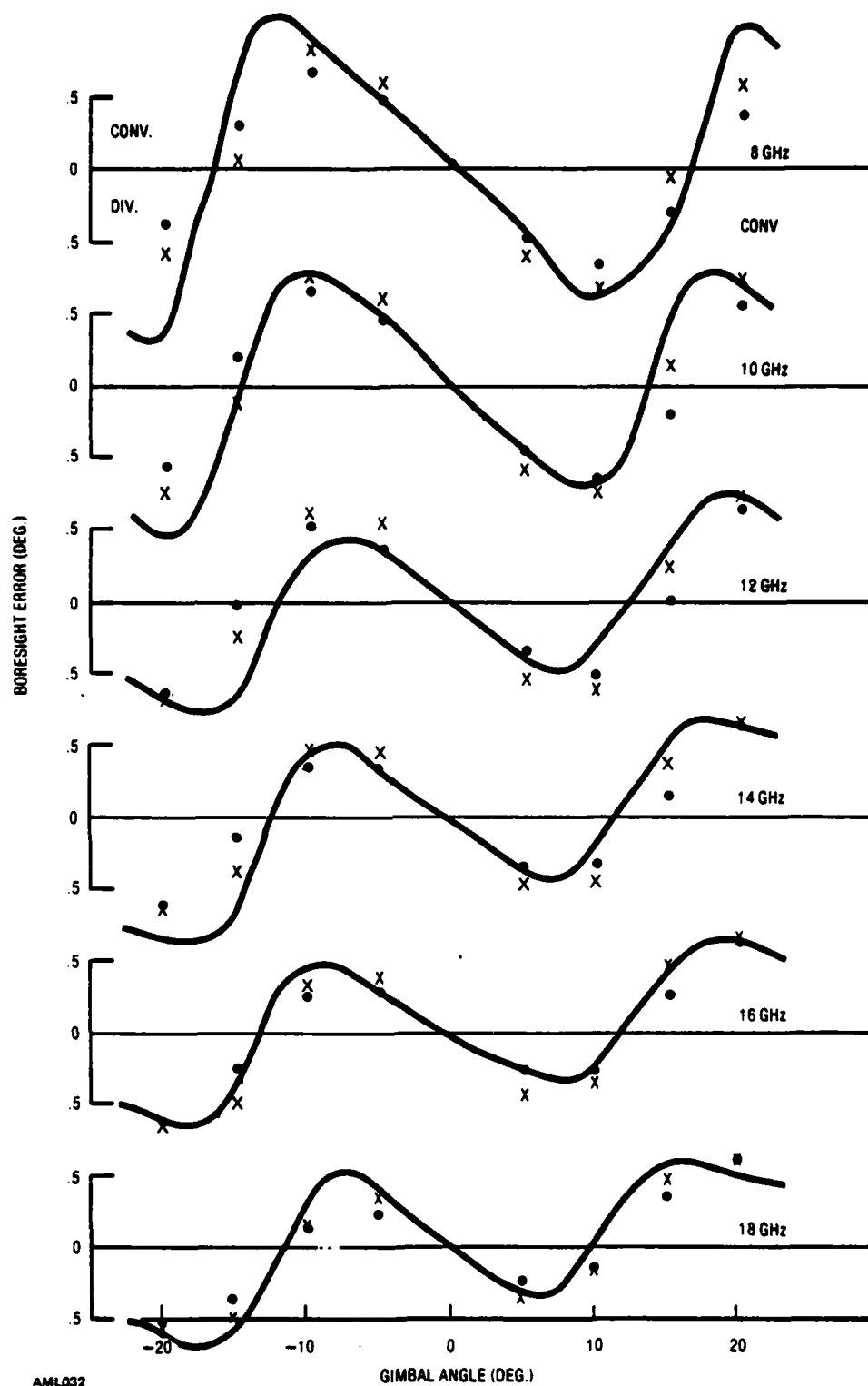


Figure 1-8. E-plane Boresight Error of 0.125 in. Thick Shell, Fineness Ratio 1.8, Dielectric Constant 2.5. Measured (—), Computed with 5 Points Representing Each Antenna (•); with 1 Point Per Antenna (x).

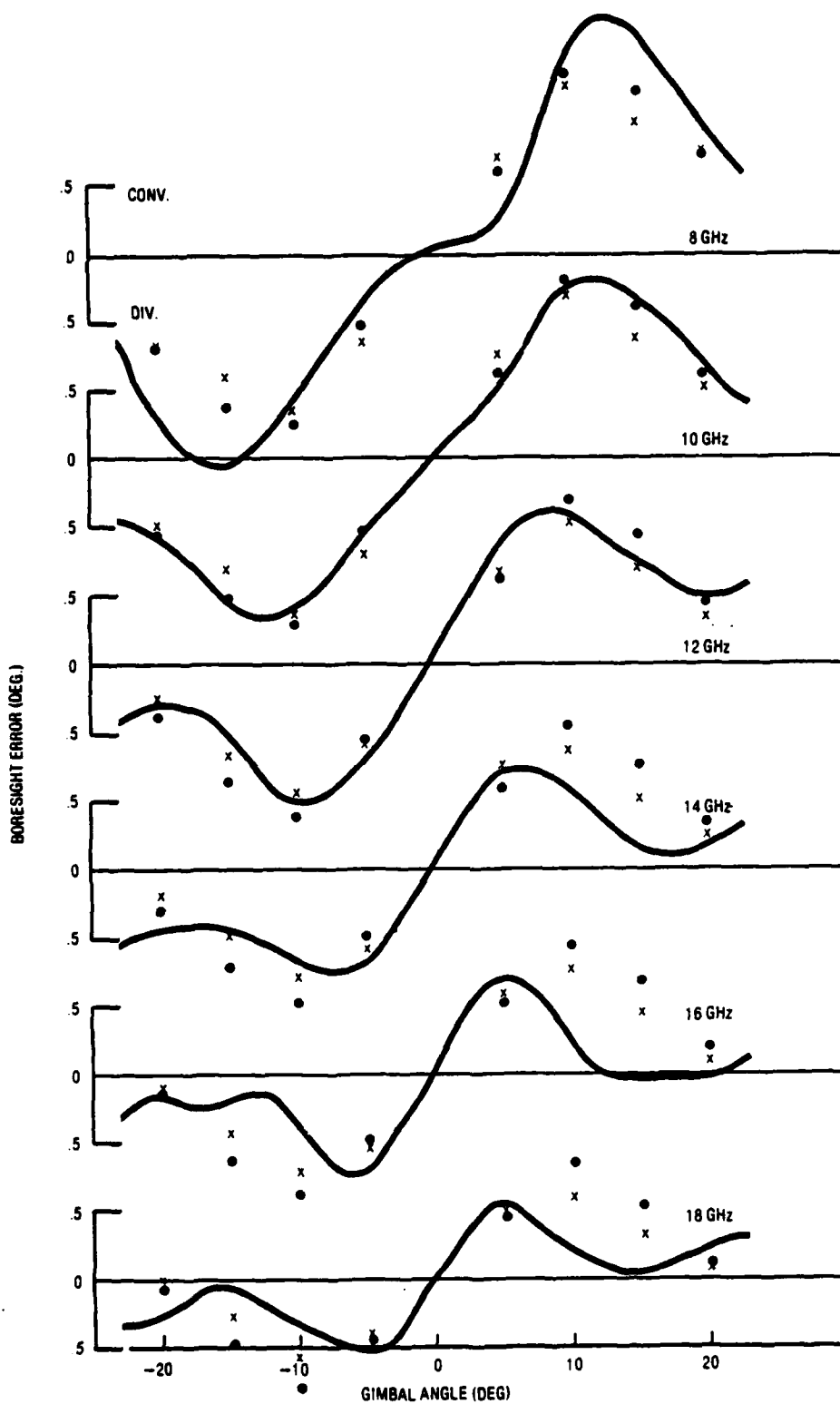


Figure 1-9. H-plane Boresight Error of 0.125 in. Thick Shell, Fineness Ratio 1.8, Dielectric Constant 2.5.

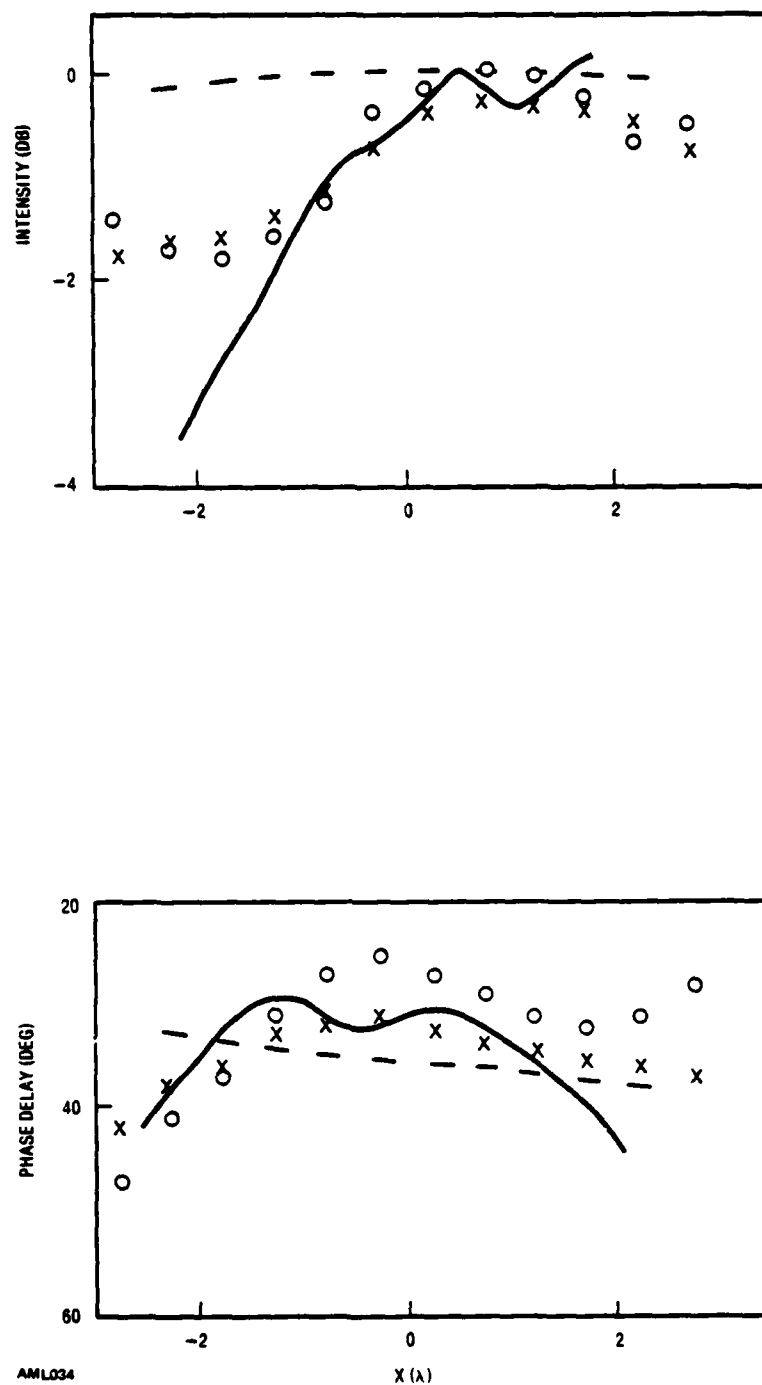
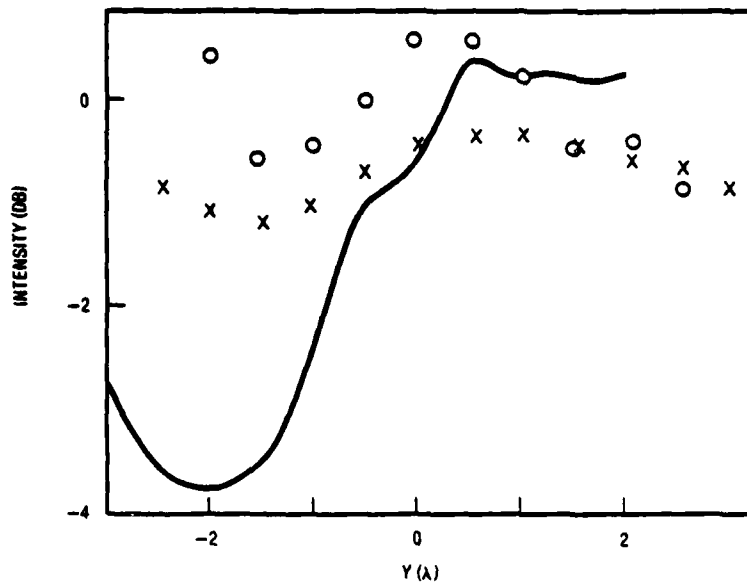
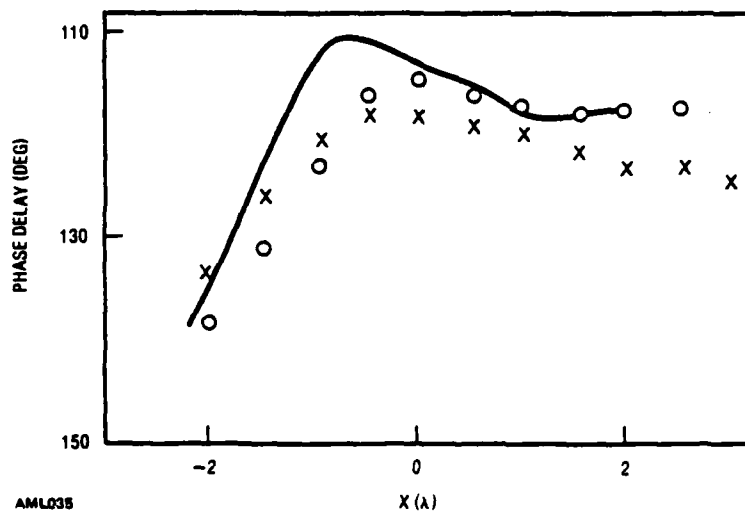


Figure 1-10. Phase Delay and Power Transmittance for Pointed Radome, Length to Diameter Ratio 1.8, Thickness: 0.125 in. Frequency: 12 GHz; E-plane; Gimbal Angle: 16°. Measured (—); Direct Ray Calculation (— —); Surface Integration with 49 Points Spaced by 0.75" (x). Surface Integration with 49 Points Spaced by 1.0" (°).

SPARROW 4" - 45" DUROID
12 GHZ E-PLANE
16° GIMBAL ANGLE



MEASURED
● DIRECT RAY
x SI 10λ 49 PT Δ = 75" 25.7°
o 10λ 49 PT Δ = 1.0" 34°
+ 10λ 49 PT Δ = 1.47" 25.3°



AML035

Figure 1-11. Phase Delay and Power Transmittance for Pointed Radome, Length to Diameter Ratio 1.8. Thickness Tapered from 0.40 in. to 0.45 in. Gimbal Angle: 16°, Frequency: 12 GHz. Measured (—). Surface Integration with 49 Points Spaced by 0.75 in. (x); with 1 in. spacing (°).

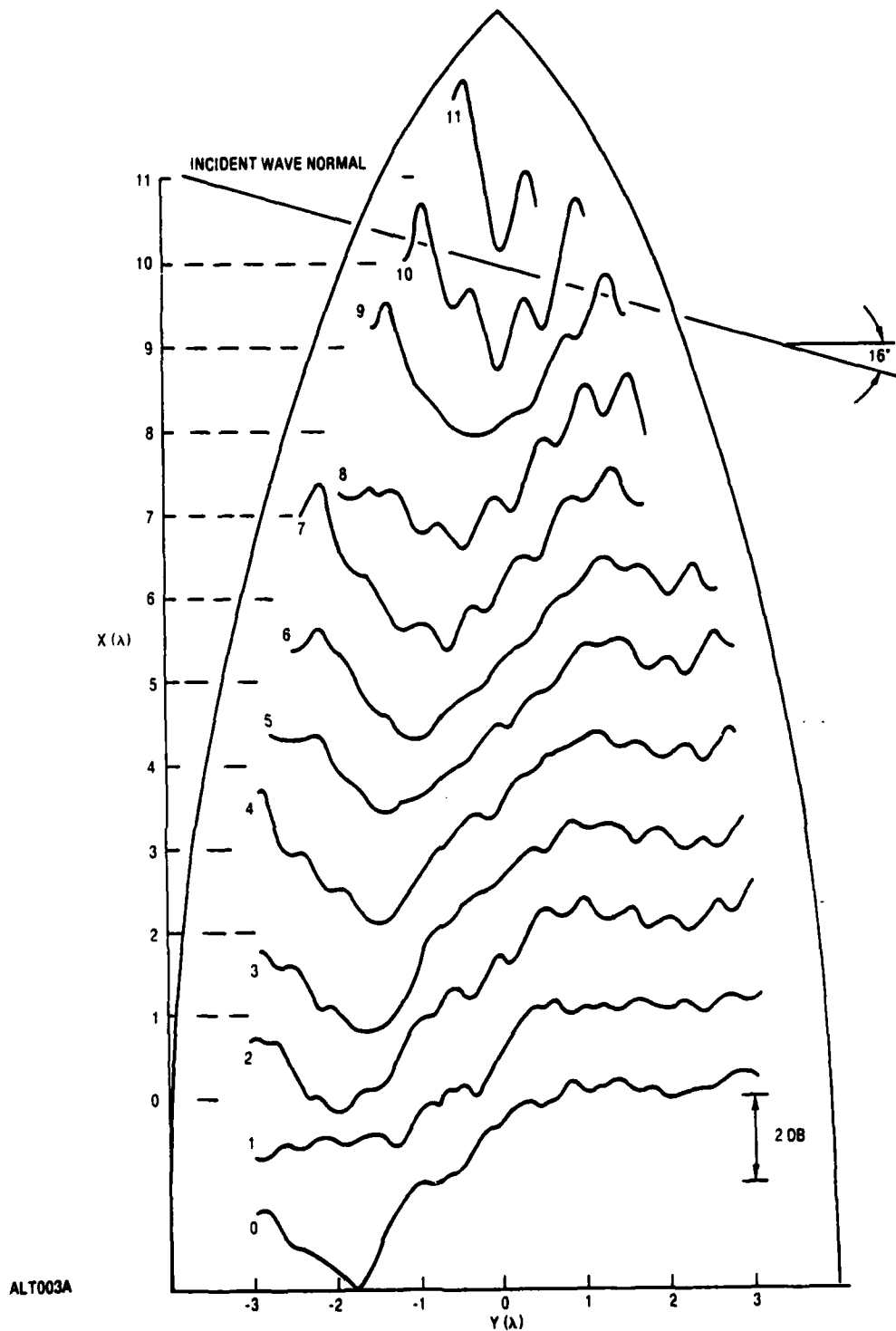


Figure 1-12. Power Transmittance at 12 GHz for a Radome with Dielectric Constant 2.6. Thickness 0.40" to 0.45", for the Field Polarized in the X-Y Plane. Each Curve is Labelled for a Particular Axial Position of the Probe Aperture and Unit Transmittance Value (0 dB) is at the Corresponding Axial Position.

In Figure 1-12 the transmittance near the wall, for $Y < 0$, is shown in Figure 1-13. This figure shows a quantity Δs , where

$$\Delta s = 2\pi (k_g - k_0 \sin)^{-1}. \quad (1-1)$$

This quantity is the spacing of fringes produced when a plane, free-space wave interferes with a coherent slab-guided wave. Therefore the transmittance in Figure 1-12 appears to result to some extent from a guided wave, as was suggested in Figure 1-2. The quantitative question of guided wave magnitude remains as does the reason for the -4 dB transmittance minima. We return to these questions subsequently.

We see that the transmittance of a radome is complicated. The direct ray and surface integration methods omit some propagation mechanisms suggested in Figure 1-2. We have seen in Figure 1-13 evidence for guided waves. Reference 4 gave evidence for guided waves in two and three dimensional radomes. In an earlier report, Reference 5, we determined guided wave amplitude on a finite slab by postulating functional forms for guided waves.

To study the effects of polarization and dielectric constant, we measured the intensity transmittance of a ceramic radome, dielectric constant 5.5, for the H-plane; see Figure 1-14. The minima are very deep so an antenna would be immersed in a very non-uniform field. However the minima spacing are irregular and do not help identify a guided wave.

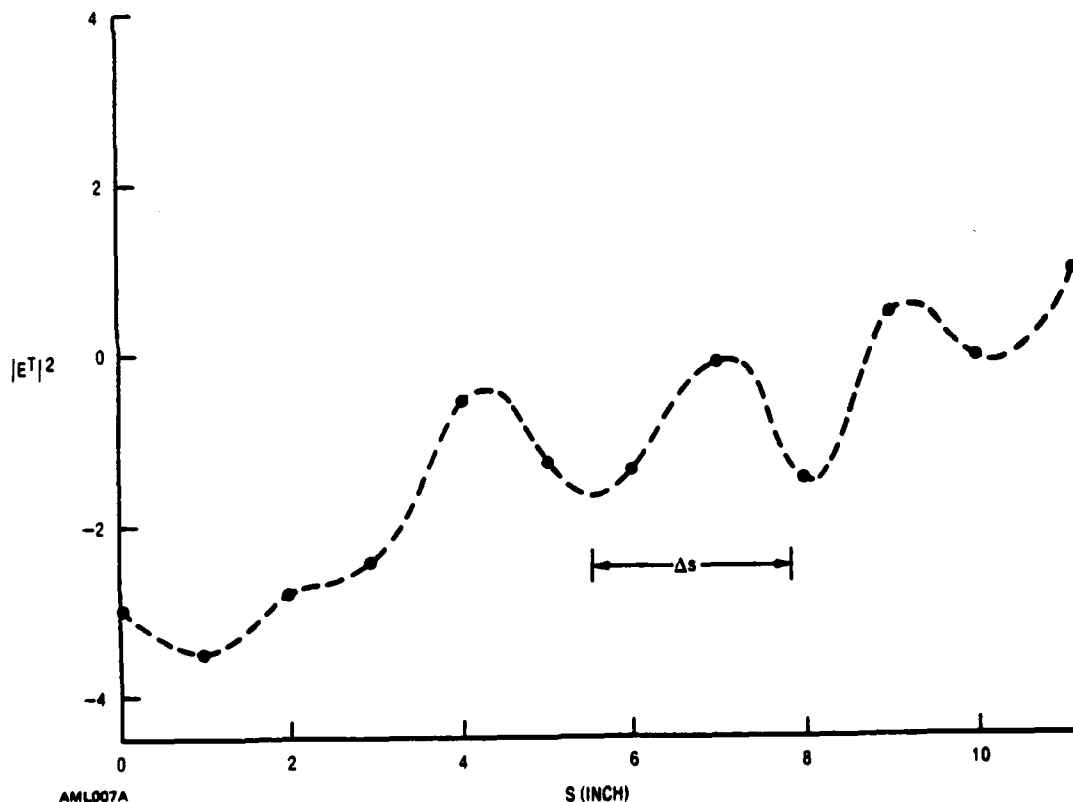


Figure 1-13. Transmittance, from Figure 1-12 at End Points of Scans

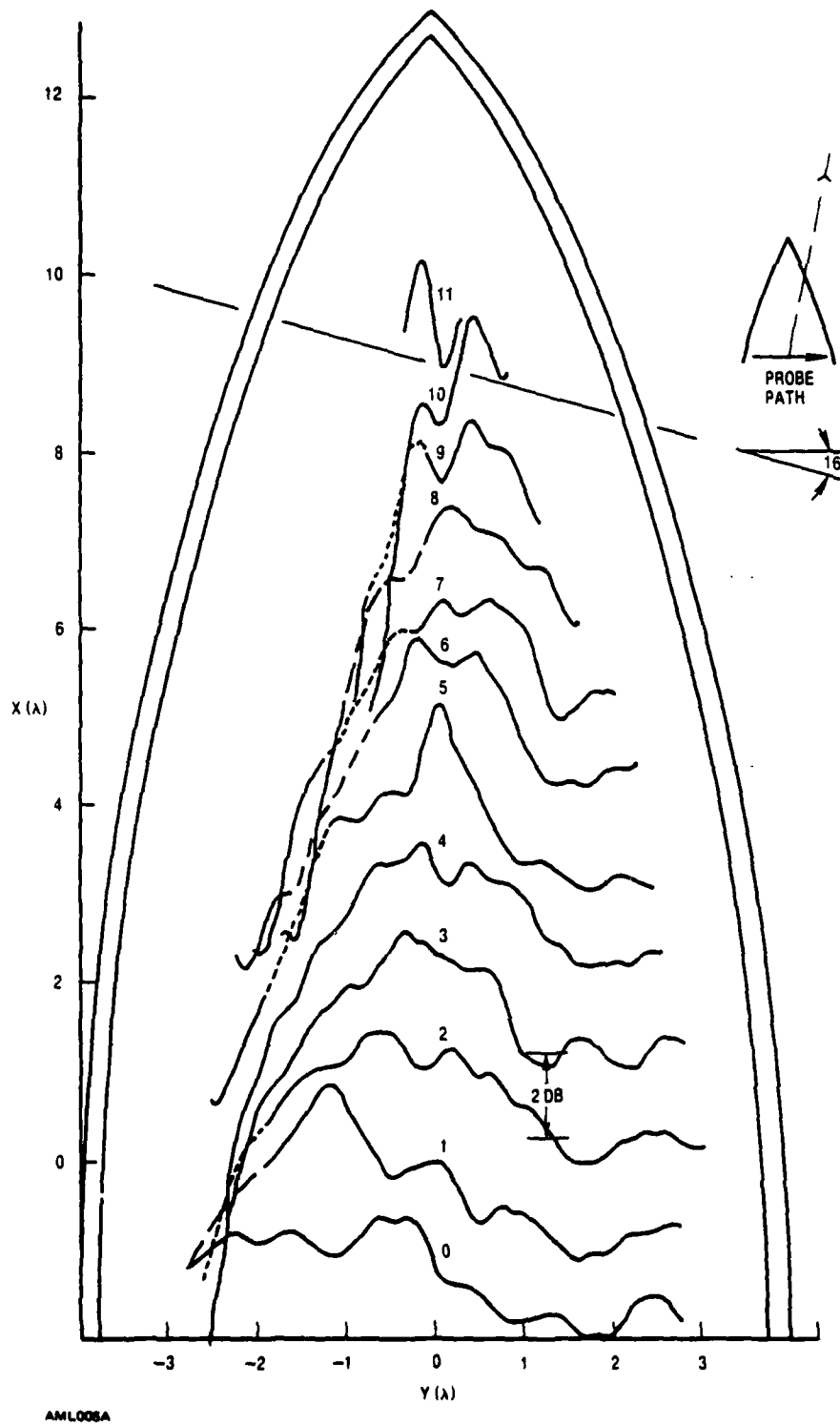


Figure 1-14. H-plane Transmittance for a Ceramic Radome at Frequency 20% Above That for Which the Thickness is a Half Wave

To separate the effects of curvature we measured the intensity behind a hollow wedge. Figure 1-15 shows $|T|^2$ for a curved wall wedge for the E-plane. Because T is high for parallel polarization, the minima are shallower than those in Figure 1-14.

Moment method calculations were made for a wedge with flat walls; see Figure 1-16. The deep minima and their spacing suggest the exponential decay (with distance from the wall) that characterizes slab-guided waves. In Figure 1-16 the decay with distance is approximately that for a slab, but only near the wall.

We conclude that guided waves exist on radomes. Their significance depends on the thickness-to-wavelength ratio because this ratio largely determines the transmittance of the direct wave. For a half-wave thickness, the direct wave transmittance magnitude is large; but at a frequency 20 percent higher than that for a half wave the direct wave transmittance is low. The perturbation caused by the guided wave depends on its own magnitude as well as that of the direct wave.

However, the guided and direct waves do not seem to be an adequate description. Guided waves are exponentially damped so they fall to small magnitudes within approximately a half-wavelength from the wall. Therefore, in Figure 1-12, guided waves do not seem to explain the transmittance minima and maxima at distances approximately a wavelength from the radome. An additional mechanism seems necessary.

A plausible mechanism is a vertex-scattered wave. Some experimental evidence exists for a vertex wave in wedge radomes.⁶ However, the situation is less clear for an axially-symmetric, pointed radome. We reduced transmittance discrepancies by adding a vertex wave to direct ray calculations⁷, but this result was obtained before surface integration was developed. The vertex wave may be a construct that corrects the direct ray method.

Because the transmittance minima and maxima in Figure 1-12 seem significant we explore a vertex wave as a possible explanation. The approach is to analyze a flat finite slab with the moment method.

1.4 A GEOMETRIC THEORY OF DIFFRACTION FOR FINITE DIELECTRIC SLABS

This section considers grazing incidence on a finite dielectric slab in order to model approximately some of the waves scattered by a hollow shell. The model is partial because the field in a shell contains a constituent wave that propagates through the illuminated side, but this wave does not occur for a slab at grazing incidence. Some or all of the other waves shown in Figure 1-2 may be present. In particular a guided wave is excited in either the slab or the shell; of course, the magnitude of the guided waves differ. The slab is an idealization also because it has not circumferential curvature; consequently, neither the incidence angle nor the polarization direction vary. Moreover, the discontinuity at the slab edge differs from that at a radome tip, but the discontinuity distinguishes both from an infinite slab. The slab approximates one side of an axially symmetric radome, and a wedge approximates both sides.

The purpose of this section is to explain power transmittance minima like those in Figure 1-12. Because of these minima a seeker antenna would be illuminated by a non-uniform field so boresight error and antenna patterns would be affected. The minima are

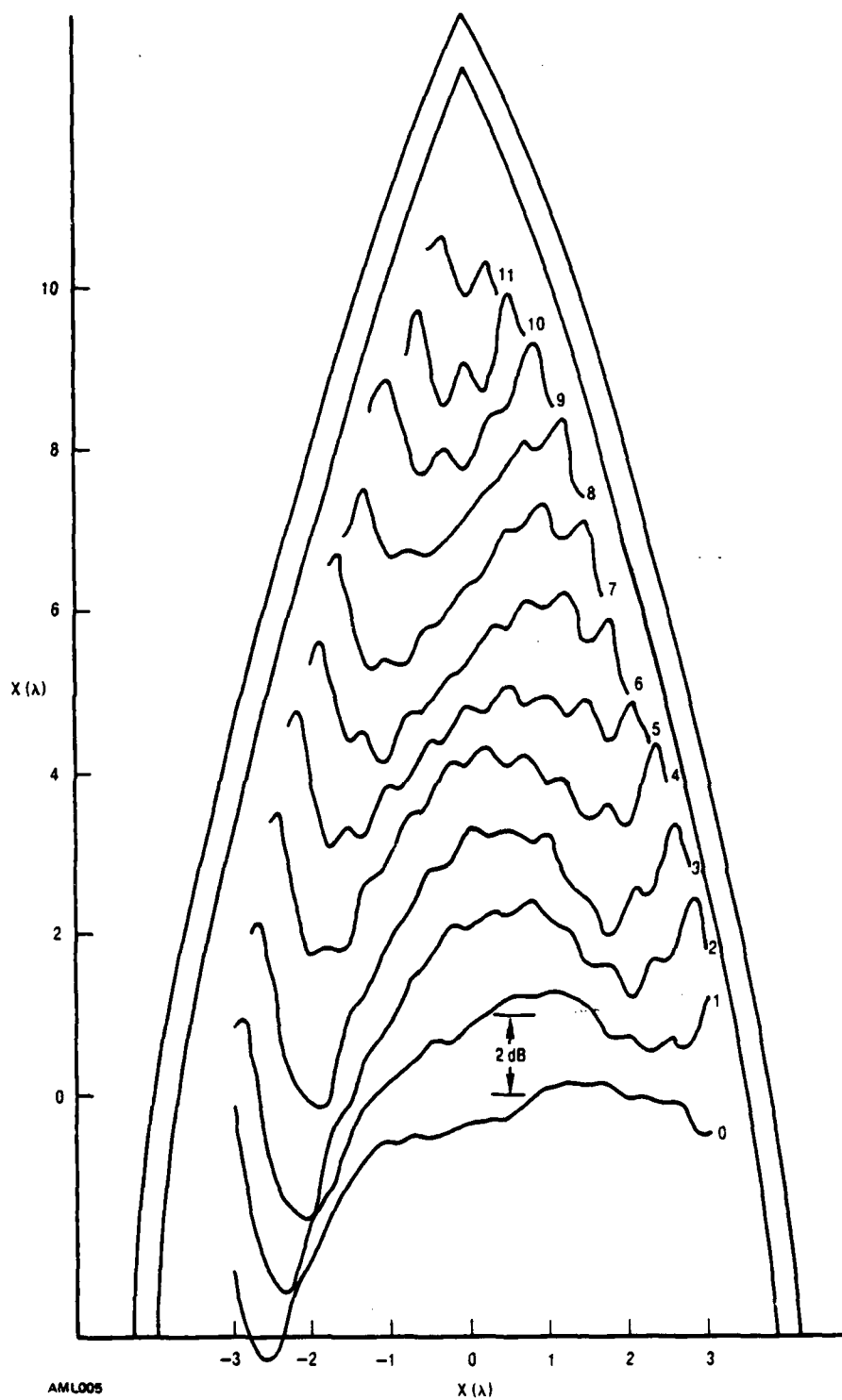


Figure 1-15. E-plane Transmittance of a Curved Wall Wedge,
Thickness 0.315" at 12 GHz

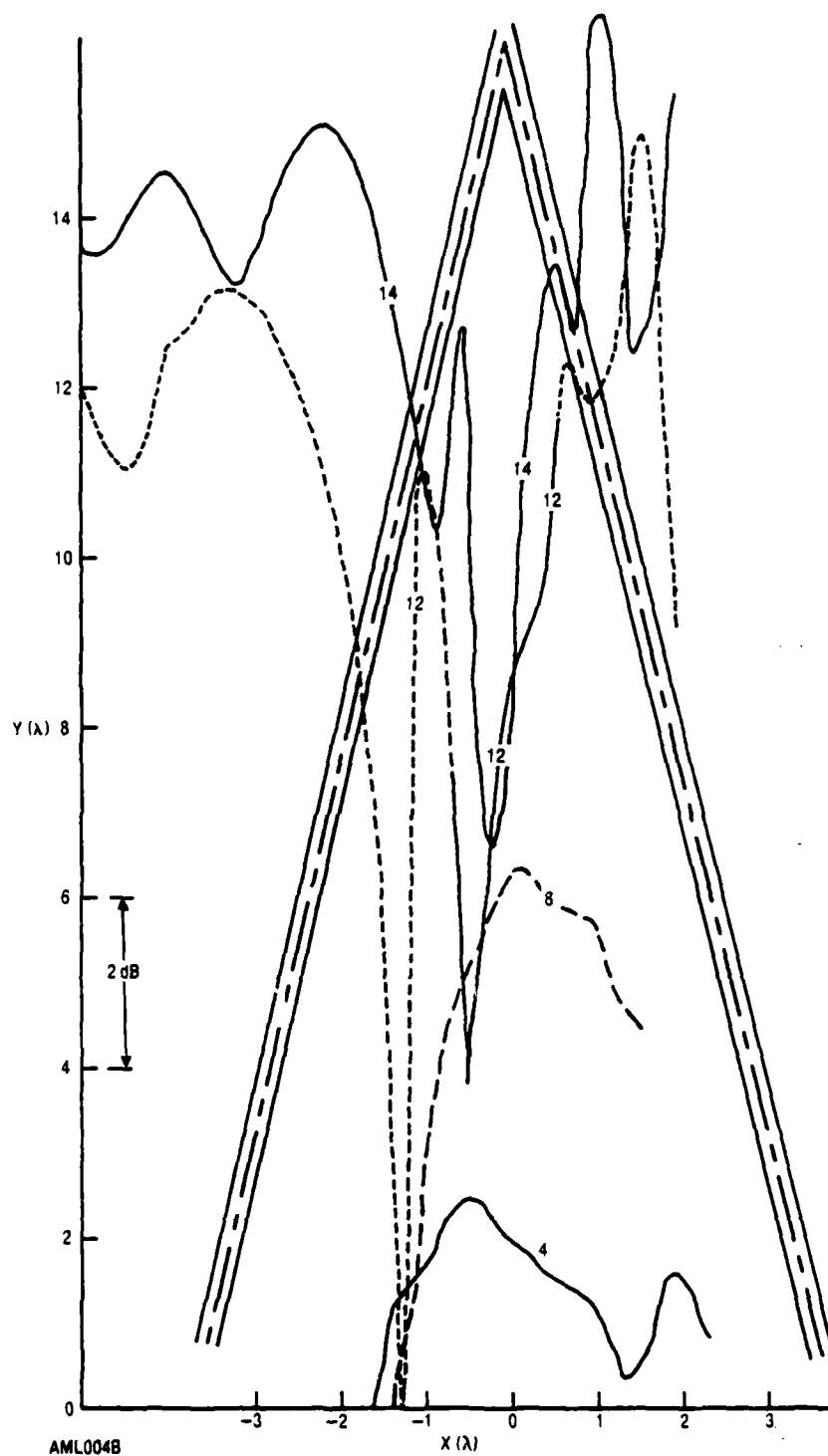


Figure 1-16. Computed H-plane Transmittance for a 0.25" Thick Wedge with Dielectric Constant 2.5 at 12 GHz

not given accurately by surface integration calculations; see Figure 1-11. Several mechanisms may exist. Reflection from the left side of the profile in Figure 1-12 is ruled out by ray diagrams. Although Figure 1-13 shows evidence for guided waves, the lowest order slab guided mode would decay to negligible values within a wavelength of the radome wall.* Therefore, another mechanism seems necessary to explain the minima, which are separated from the wall by more than a wavelength.

To study possible mechanisms we start by computing the field in and near a two-dimensional slab with the moment method of Richmond. Coordinates are shown in Figure 1-17. The slab has infinite extent in the plane orthogonal to the figure, and incidence is in the X-Y plane. The slab is approximated by a set of infinite, circular cylinders, and the fields at the centers of the cylinders are determined. Figure 1-18 shows the total field intensity at each cylinder center and the total field outside the slab.

To check the computed field, measurements were made with a dipole probe. The dipole scanned several paths parallel to the slab. Measured intensity is shown in Figure 1-19. Agreement is good. In Figure 1-18, the fringe spacing for $Y = 0.54$ in. agrees with Δs computed from Equation 1. This spacing is evidence that guided waves were excited on the slab. The shallow oscillations with period 0.5 in. result from interference of guided waves travelling in opposite directions.

*A calculation later in this section gives the decrease with distance from the wall.

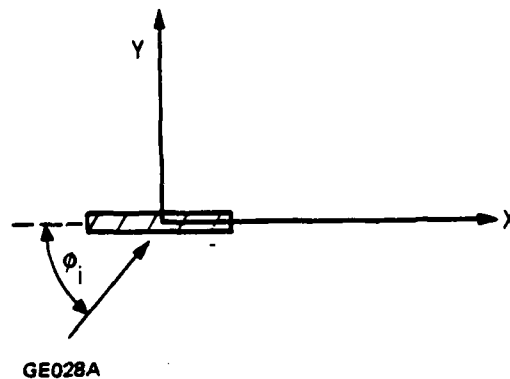
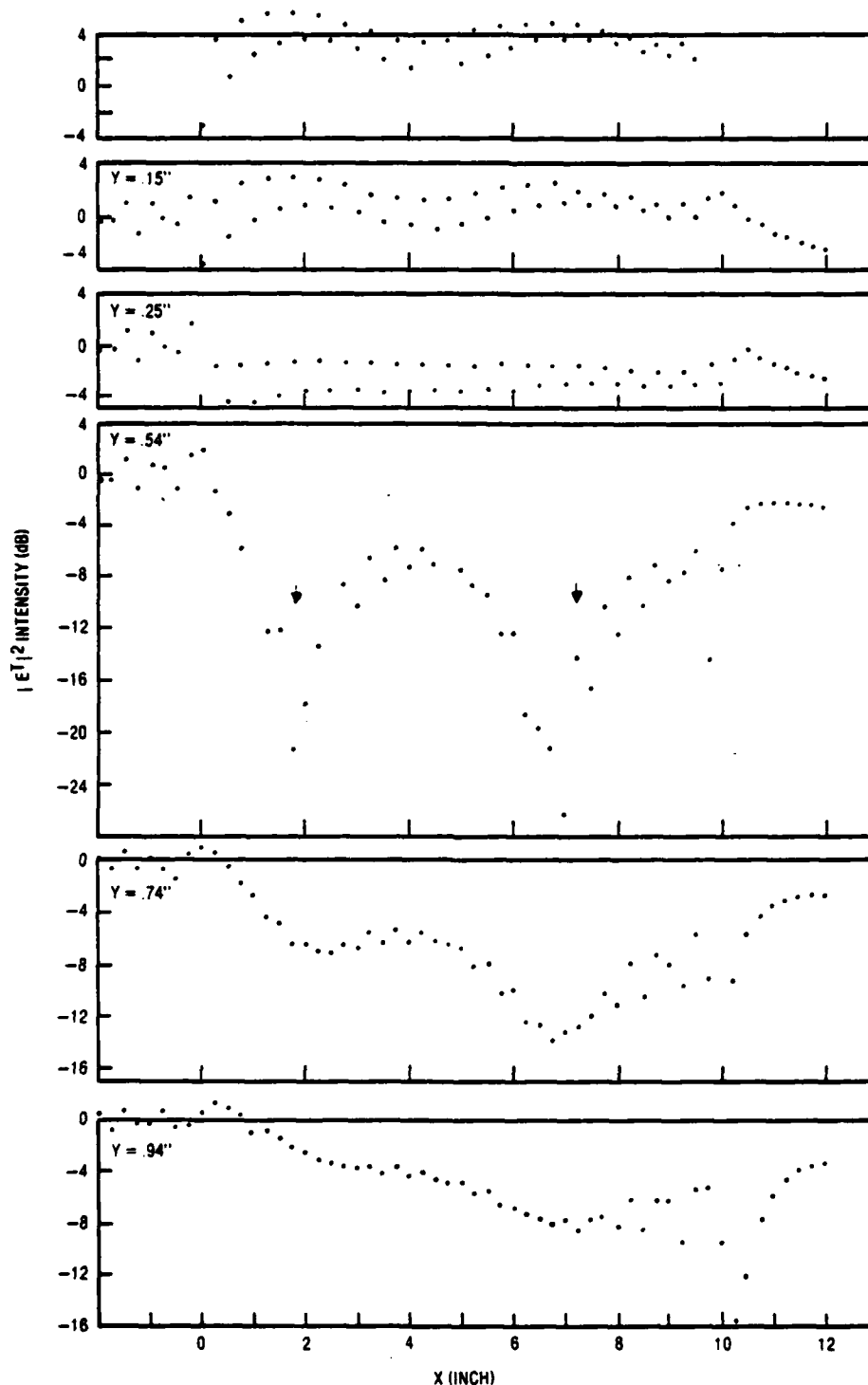


Figure 1-17. Coordinates for a Slab



AML036

Figure 1-18. Total Field Intensity in Slab for Grazing Incidence. Length 10 in.; Thickness 0.25 in.; Wavelength 1.26 in.; Polarization: Perpendicular; Dielectric Constant 2.6.

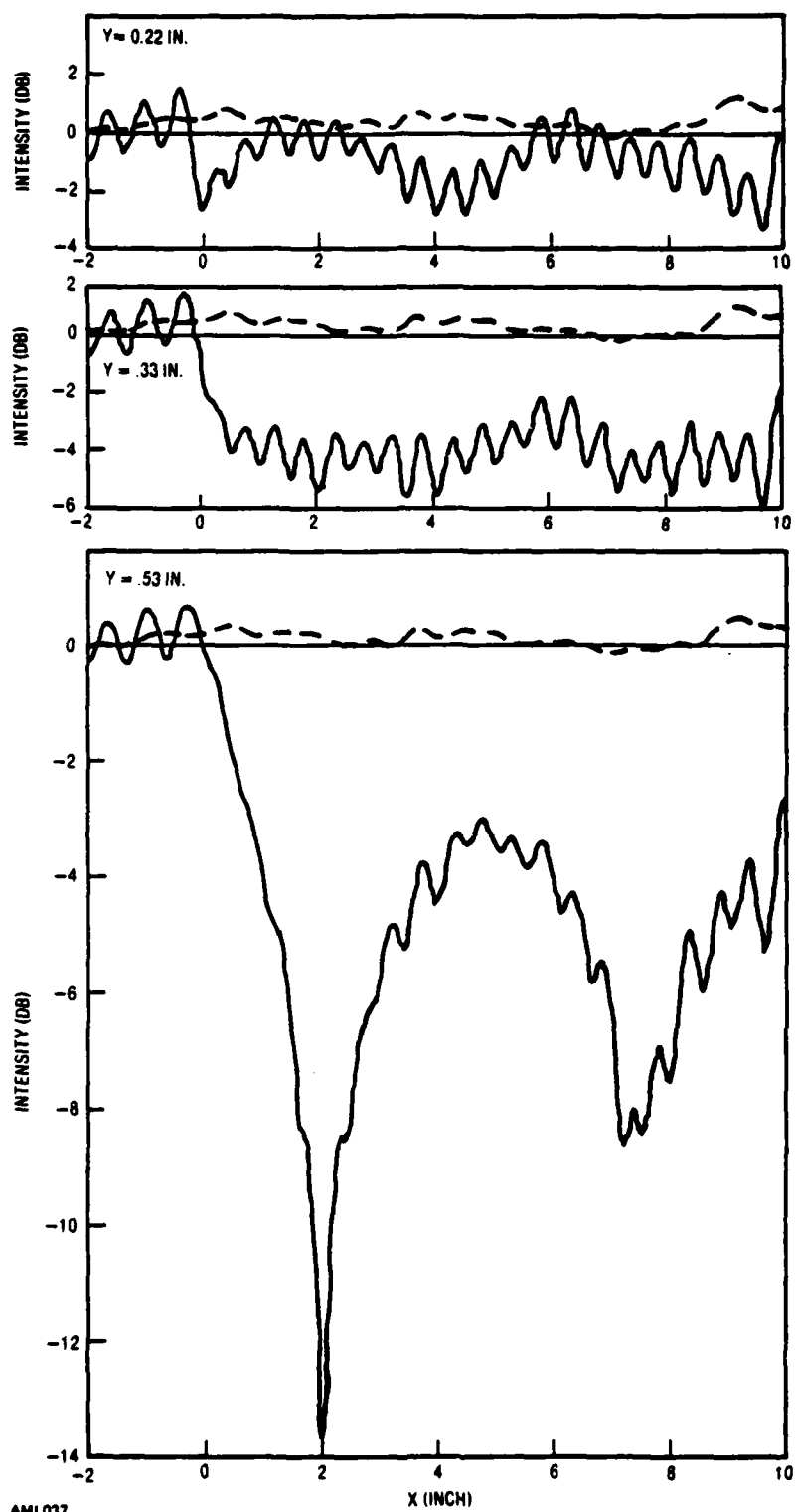


Figure 1-19. Measured Intensity Near Slab (Length 10 in.; Thickness 0.25 in.; Wavelength 1.26 in.; Dielectric Constant 2.6).

The scattered field magnitude (the total field minus the incident) is shown in Figure 1-20. The field is not uniform, indicating that the scattered field in the slab contains more constituents than just a guided wave. Since the spacing of peaks in Figure 1-20 is Δs to a good approximation, the field in the slab apparently consists mainly of a guided wave and a plane wave with free space propagation constant. In addition, a small amplitude reflected guided wave is also present. The free space propagation constant k_0 rather than nk_0 , when n is the index of refraction, is remarkable. Apparently k_0 occurs because the slab is thin, not a volume in which n modifies the wavelength.

To test the guided wave hypothesis and to estimate its excitation, we examine the curve for $Y = 0$ in Figure 1-20. Consider the oscillation of $|E^s|$. The value varies from 2.7 to approximately 0.1, where $|E^i|$ has unit value. Now smooth the variation with period 0.5 in.; $|E^s|$ varies from 2.3 to 0.1, or 1.2 ± 1.1 . We assume the amplitude 1.2 represents that of a guided wave propagating in the positive X direction. Now consider the variation of a slab-guided wave with Y . In the slab, the field has the form

$$E_{Gi} = 1.2 \cos u y; \quad (1-2)$$

outside for $Y > 0$ the field has the form

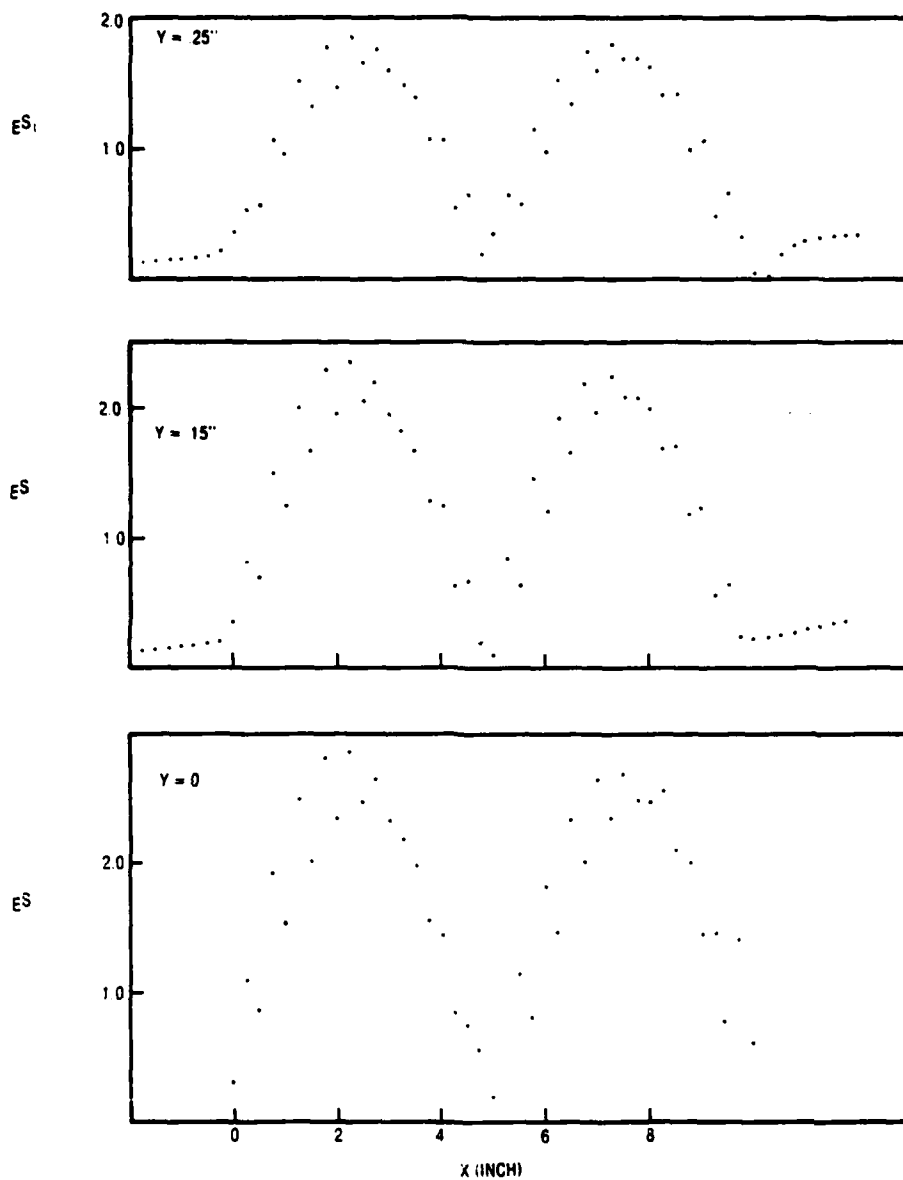
$$E_{Go} = 0.96 e^{-v(y-b)} \quad (1-3)$$

where v is computed from boundary conditions as 1.12 inches and b is half the slab thickness. The scalar amplitude 0.96 was computed from Equation 1-2, with $u = 1.65$ inches. The values computed from Equations 1-2 and 1-3 are shown in Figure 1-21. For comparison, estimates of guided wave amplitude derived from Figure 1-20 and additional calculations by the moment method are shown in Figure 1-21. The agreement in Figure 1-21 is additional evidence for a slab guided wave and verifies the estimate of excitation magnitude.

The apparent value of k_0 rather than nk_0 discourages a simple ray picture that assumes nk_0 for an internal ray; however, outside the slab a free-space plane wave (plus an evanescent guided wave) seem reasonable.

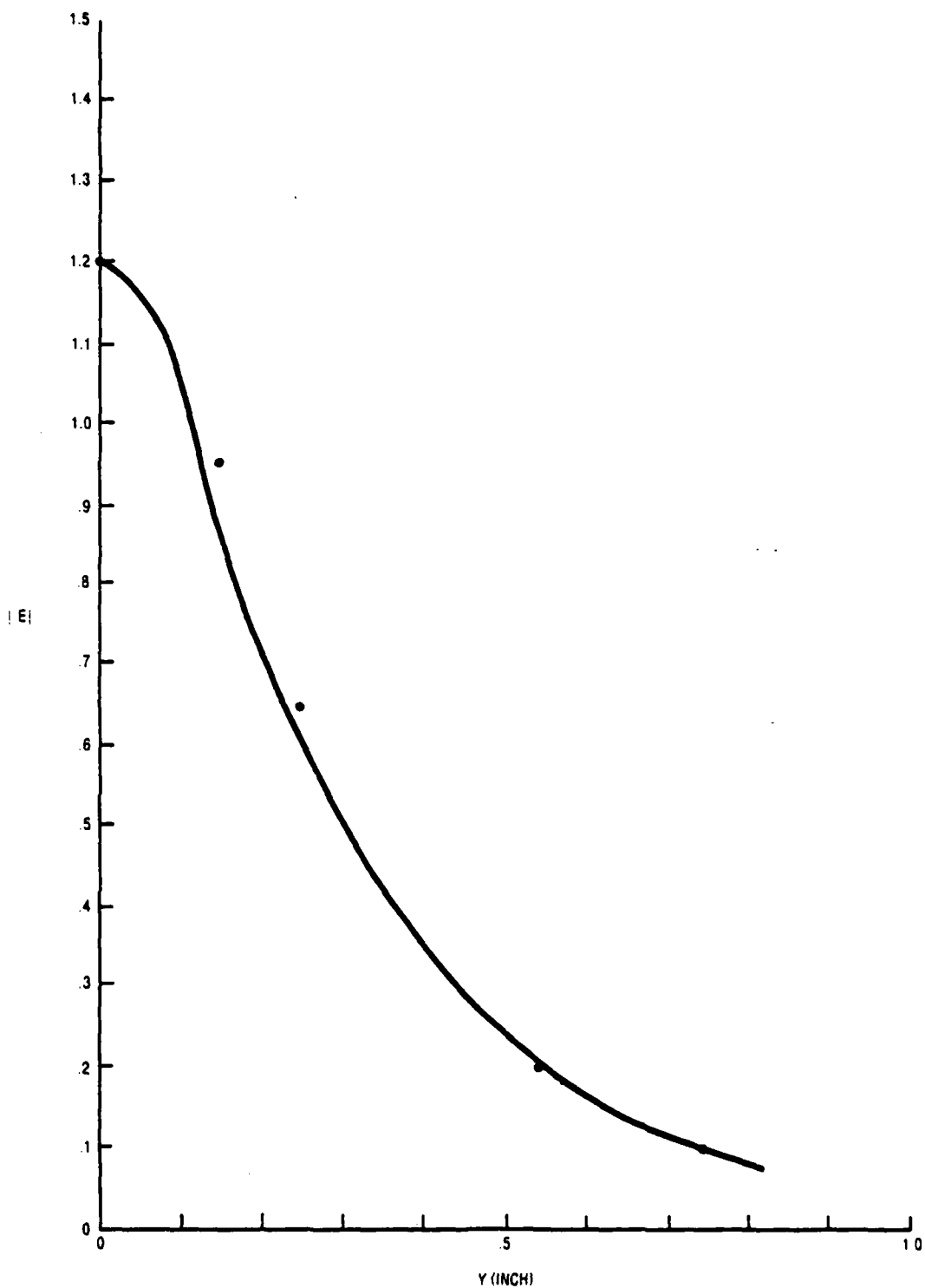
To determine the form of the wave that combines with the guided wave, we graph the phase increment of the scattered field between adjacent points on the X -axis. Inside the slab at $Y = 0$, Figure 1-22 shows wide variations. Outside, the free phase increment is reached approximately for $Y = 0.94$ in. The phase increment $k_0 \Delta x$ is 71.5° for $\Delta X = 0.25$ in. At even larger distances (6 in.) the amplitude of the scattered field is below 0.1.

To obtain a comprehensive view of the fields near the slab we plotted the contours of computed phase and intensity of the scattered field for grazing incidence. See Figures 1-23 and 1-24. The total field phase and intensity contours are plotted in Figures 1-25 and 1-26.



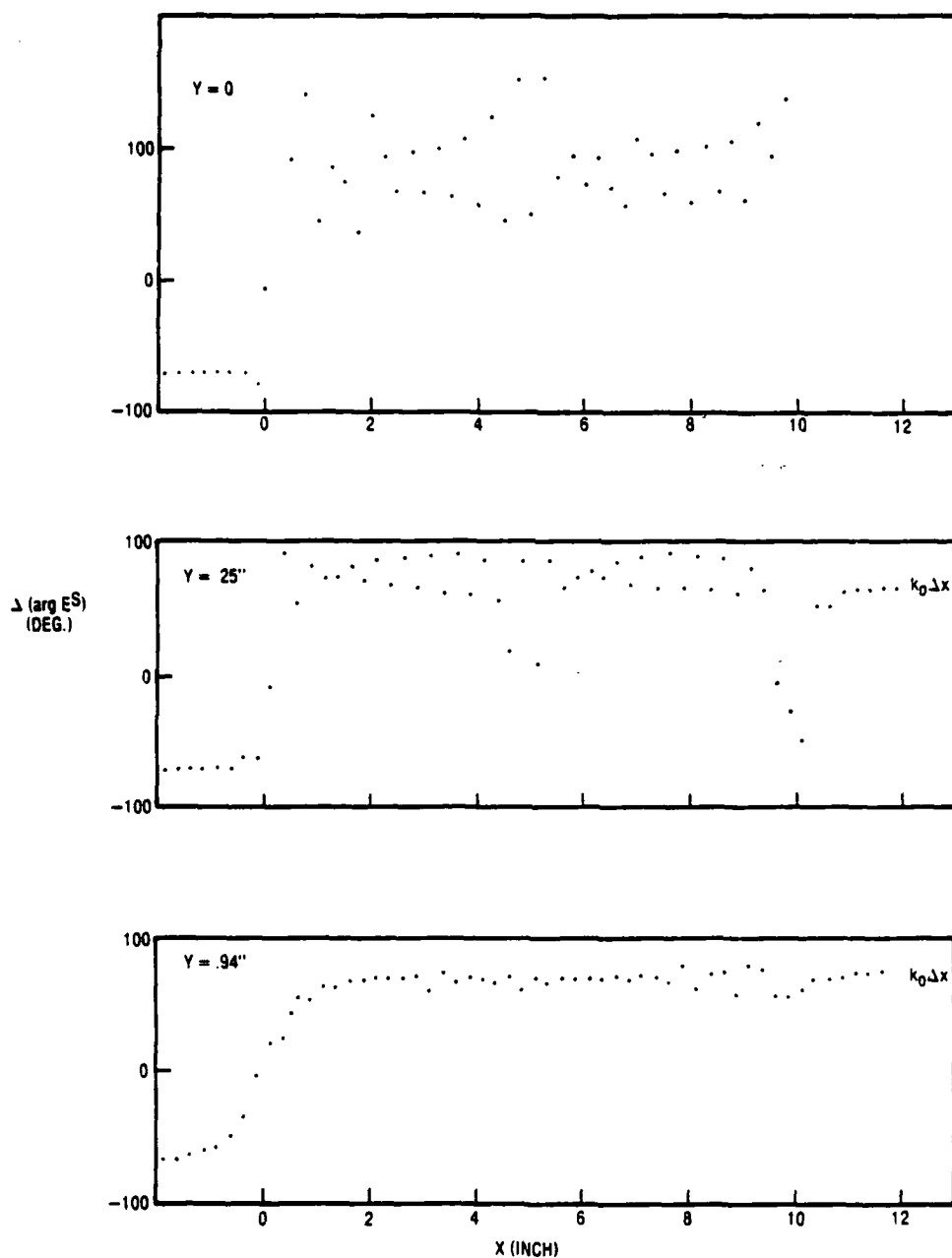
AML038

Figure 1-20. Scattered Field Magnitude Near Slab Computed by Moment Method



AML039

Figure 1-21. Computed Decay of Guided Wave Amplitude for Slab. The Curve is from Equations 1-2 and 1-3. The Points are Moment Method Calculations.



AML040

Figure 1-22. Phase Increment for Grazing Incidence on Dielectric Slab
Computed with Moment Method. Slab: 10" Long, 1/4" Thick,
 $\kappa = 2.6$. Wavelength: 1.259".

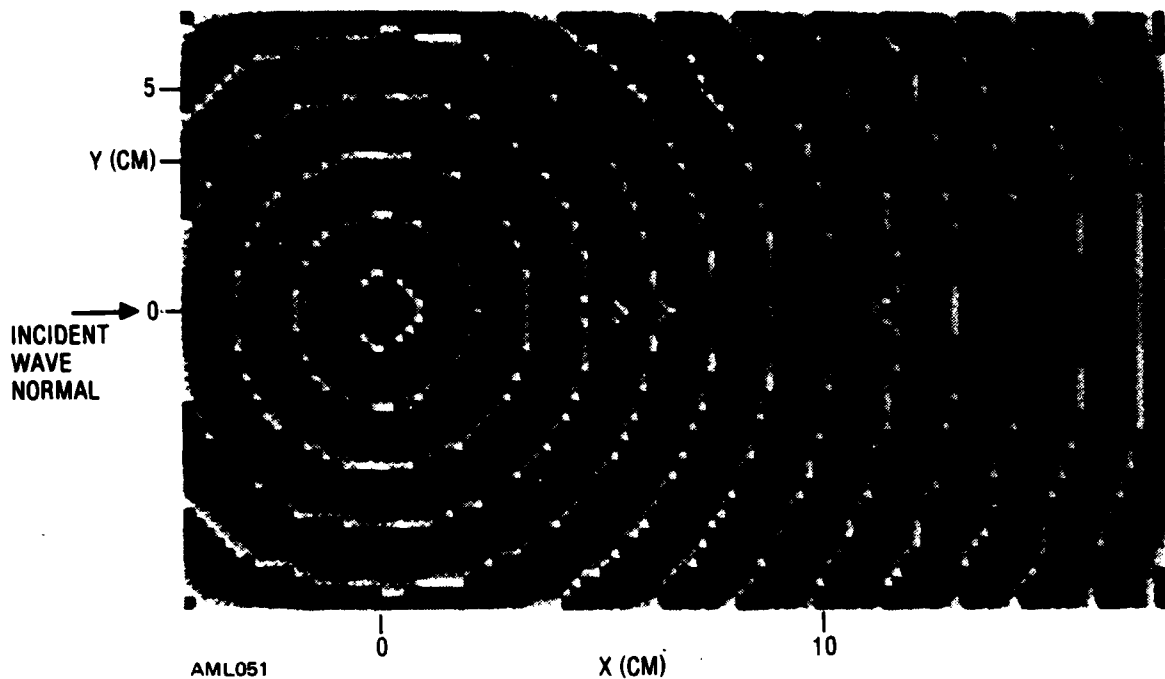


Figure 1-23. Computed Scattered Field Phase Contours Near 1/4 in. Thick, 10 in. Wide Slab with $\kappa = 2.6$; Wavelength: 1.26". Incidence: Grazing. The Contours are Spaced by 360° .

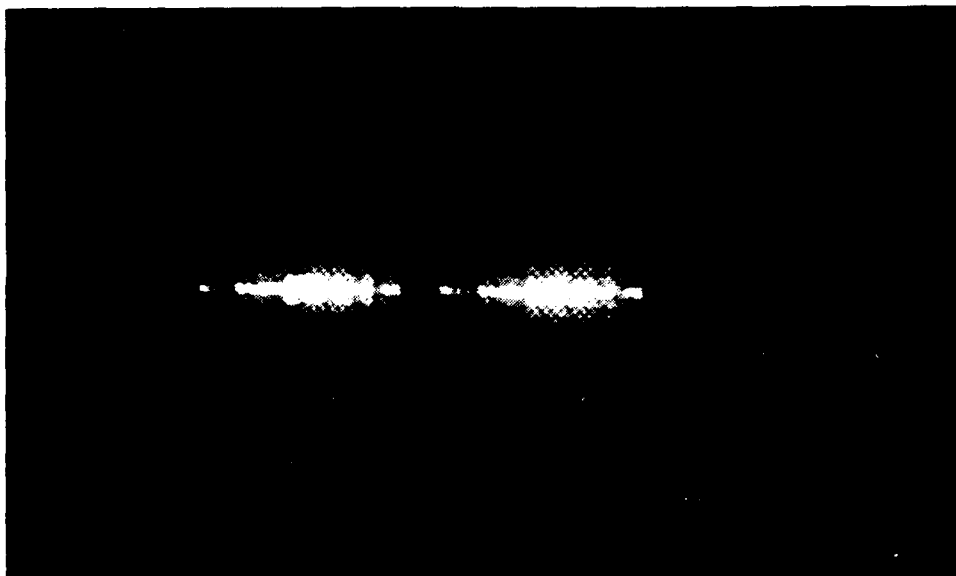
The phase of the scattered field shown in Figure 1-23 suggests a cylindrical wave from the edge nearest the source. Within the slab, the phase changes rapidly near X equal 5 in. This behavior was shown graphically in Figure 1-22; see the graph for $Y = 0$ near $X = 5$ in.

We conclude that the scattered field consists of guided waves, a cylindrical wave from an edge, and an approximately plane wave at larger distances from the slab. However the analysis does not explain why the second constituent of E^S should travel as $\kappa_0 x$ in the slab.

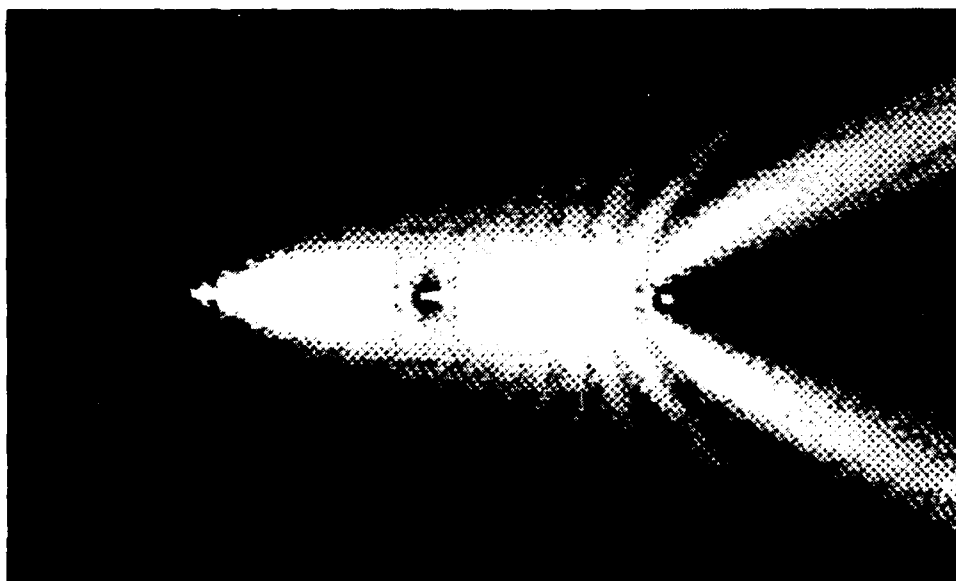
Consider the total field in Figure 1-26. For the region outside the slab, we assume the total field consists of the incident field and a cylindrical wave centered at the origin, which is at $X = 0$, $Y = 0$. The field is thus

$$E = e^{ik_0 x} + C e^{ik_0 r} \quad (1-4)$$

where r was approximated by $x + (y^2/2x)$, and C is as yet an undetermined constant. To test Equation 1-4 we computed loci such that the two terms are in phase. Figure 1-27 shows two such loci superimposed on moment method calculations. To obtain this agreement we choose C to be -1. That is, the cylindrical wave suffers a phase reversal on its excitation. Since amplitudes were not computed, the magnitude of C was not determined by using Equation 1-4.



10 IN SLAB SCAT FLD 0DEG
 .0191 2.2000 .0191 2.2000



10 IN SLAB SCAT FLD 0DEG 9.7GHZ
 .0191 2.2000 .0191 .9500

AML042

Figure 1-24. Computed Intensity in Field Scattered by Slab. The Intensity Levels are Compressed in the Lower Picture.

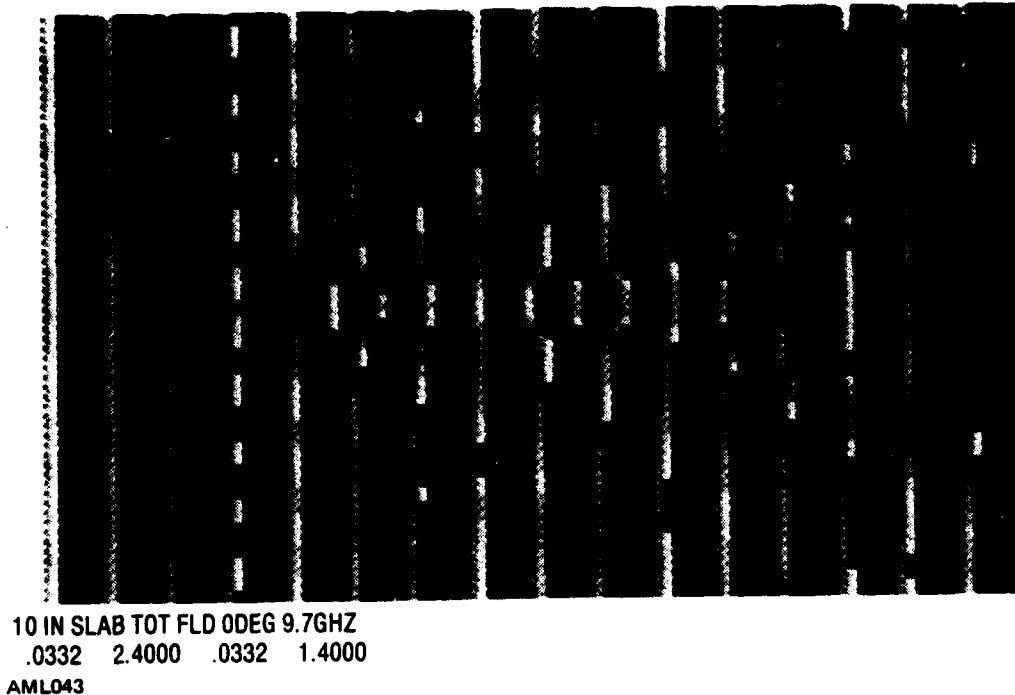


Figure 1-25. Phase of Total Field for Slab

In Figure 1-26, the maxima and the minimum near the slab resemble the variations in Figure 1-12. Therefore the analysis of the slab seems relevant to analysis of radomes so that some additional analysis on estimating amplitudes near the slab seems warranted.

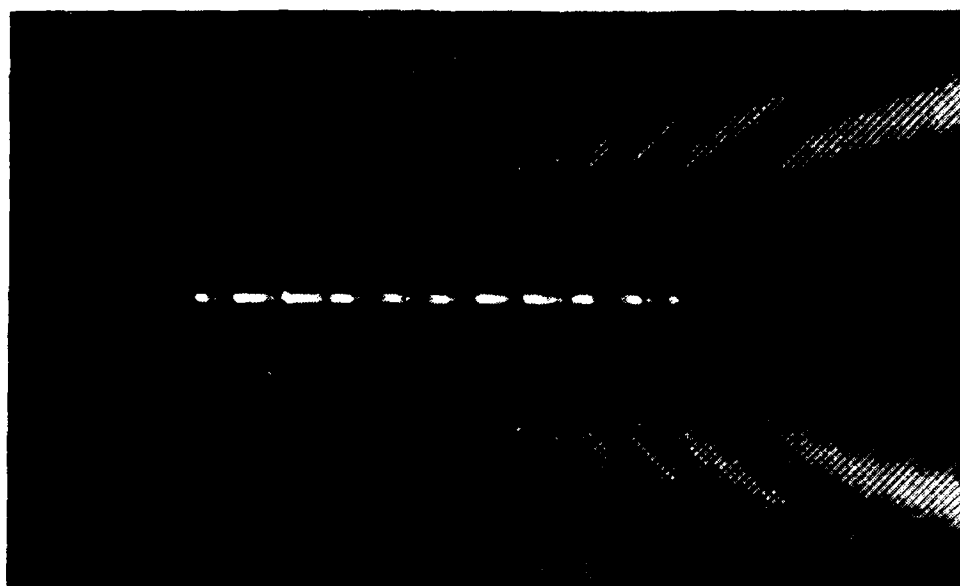
Now consider Figure 1-28. It shows the variation of the fields with Y the transverse coordinate for X fixed at 5 in. For the total field E computed by the moment method, maxima occur at Y equal 2.4 in. and 4.8 in., and a minimum is Y equal 0.6 in. The two maxima in $|E|$ coincide with bright regions in Figure 1-26, and the arrows indicate maxima positions determined by assuming a cylindrical wave, see Equation 1-4.

For the scattered field, $|E^S|$ computed by the moment method is also shown in Figure 1-28. We see a minimum for Y equal 0, despite the maximum of $|E|$ of a guided wave and a wave with propagation constant κ_0 .

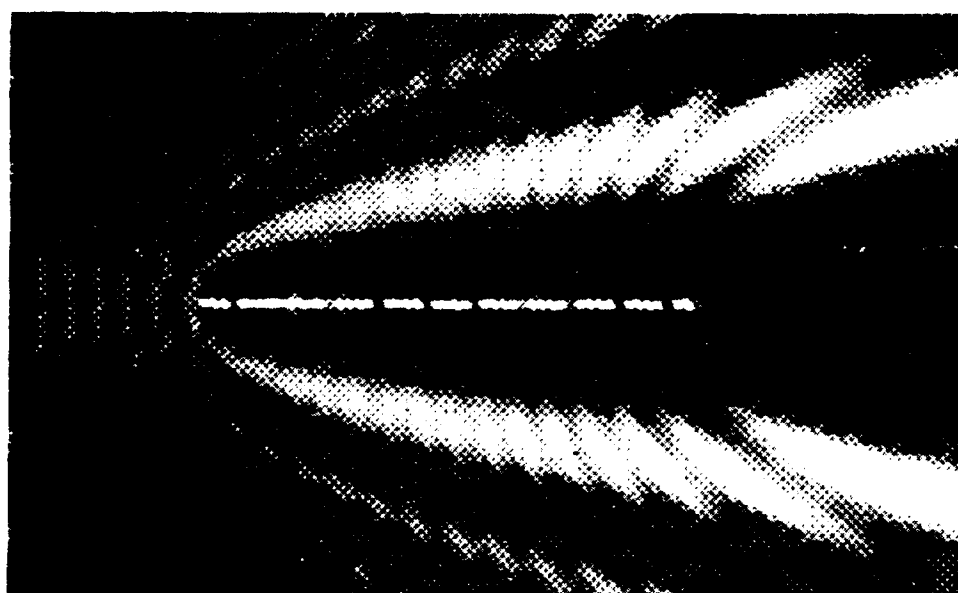
The magnitude of the scattered field's guided wave constituent $|E_G|$ was graphed in Figure 1-21. It is shown in Figure 1-28 on another scale.

The magnitude of the cylindrical wave constituent $|E_C|$ is shown also in Figure 1-28. The value 1.1 for Y equal 0 was estimated from the interference behavior of the scattered field; Figure 1-20. For values of Y greater than 0.6, $|E_C|$ was taken as $|E^S|$ because E_G has decayed to negligible values. For Y equal 0.6 we assumed $|E_C| = |E^S| - |E_G|$ because the value of $|E^S|$ was nearly zero.

The phase variation at Y equal 5 in. is shown in Figure 1-29. The moment method value of $\arg E^S$ is well matched by the assumed cylindrical wave phase except at $Y = 0$, where



10 IN SLAB TOT FLD 0DEG
 .0332 2.4000 .0332 2.4000



10 IN SLAB TOT FLD 0DEG 9.7GHZ
 .0332 2.4000 .0332 1.4000

AML044

Figure 1-26. Intensity of Total Field for Slab. The Intensity Levels are Compressed in the Lower Picture.

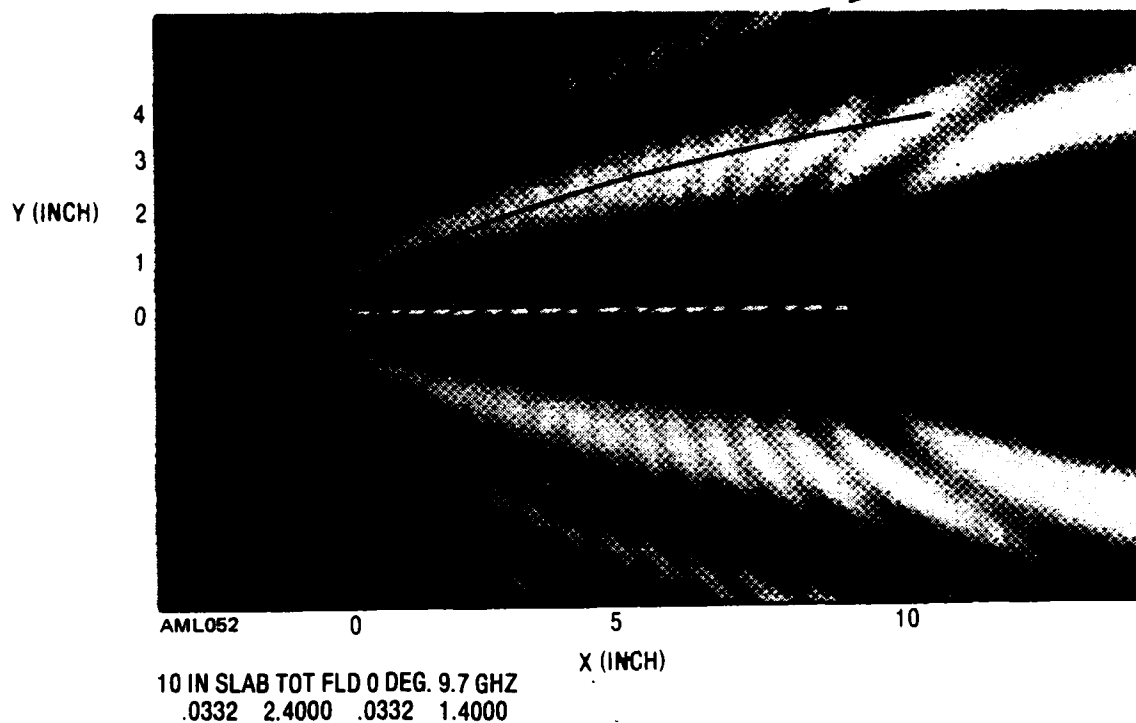


Figure 1-27. Computed Loci of Constructive Interference

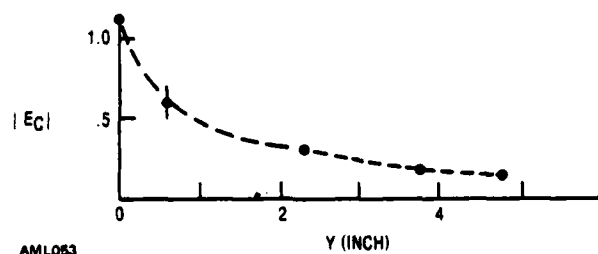
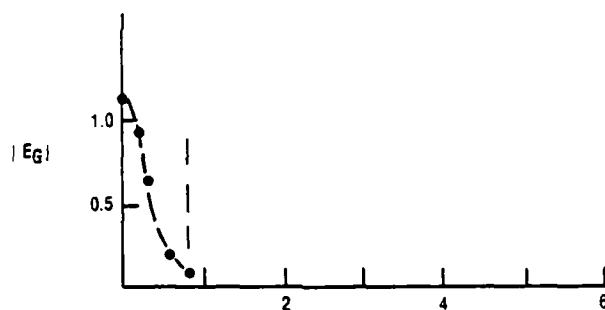
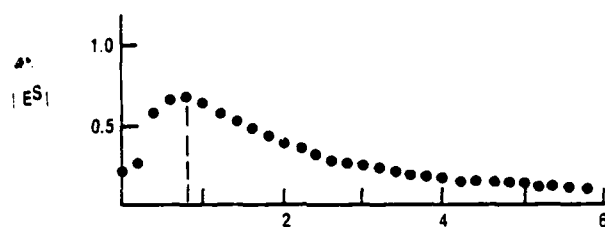
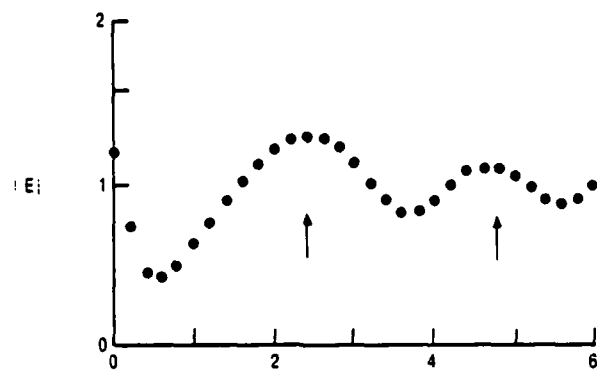
the guided wave amplitude is high. This guided wave component is apparently present in the moment method results, but it is of course absent from the cylindrical wave constituent of the scattered field.

The preceding analysis leads to a geometric diffraction theory description of scattered fields near a finite width slab for grazing incidence. This description is summarized in Figure 1-30. The field consists of the waves in Table 1-1.

Table 1-1. Constituent Waves

WAVE TYPE	VARIATION	MAGNITUDE AT X EQUAL 5 IN.
Incident	$\exp(i\kappa_0 x)$	1
Guided wave (forward)	$\exp(i\kappa_g x)$	1.2
Guided wave (reflected)	$\exp(-i\kappa_g x)$	0.2
Cylindrical wave	$\exp(\kappa_0 r + \pi)$	1.1 for $Y = 0$ 0.37 for $Y = 2$ in.

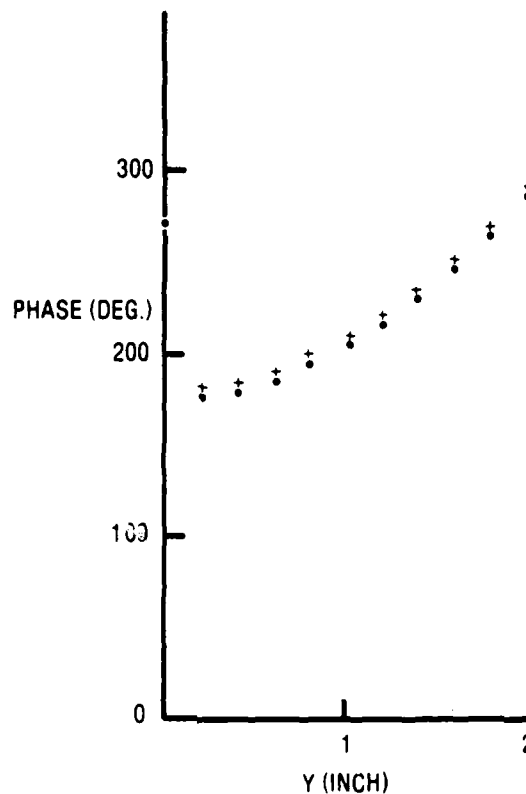
We thus have solved a canonical problem.



AML053

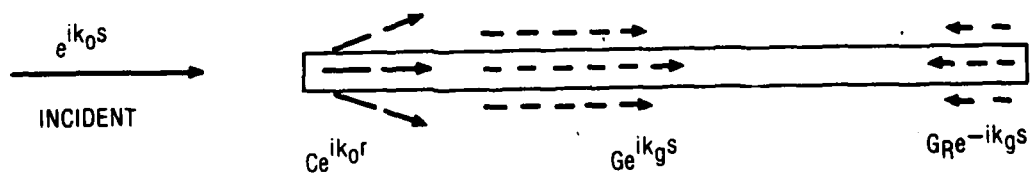
Y (INCH)

Figure 1-28. Fields Near a Slab for Y Equal 5 in. E is the Total Field, and E^S is the Scattered Field, Both Computed by the Moment Method. E_G is a Guided Wave Constituent of the Scattered Field and E_C is the Cylindrical Wave Constituent. Frequency 9.4 GHz.



AML054 B

Figure 1-29. Computed Phases of Scattered Fields. Moment Method (·);
for Cylindrical Wave with π Added (+)



AML055 A

Figure 1-30. Constituent Fields Near a Slab for Grazing Incidence.
The Guided Waves have Propagation Constant k_g . The Cylindrical
Wave Has Propagation Constant of Free Space k_0 .
These Waves are Geometric Diffraction
Corrections to Direct Waves.

2. SCALAR GREEN'S FUNCTION FORMULATION

2.1 INTEGRATION OF MAXWELL'S EQUATIONS

The starting point is Maxwell's equations.⁸ The symbols have their usual meanings, and the time variation has the form $\exp(-i\omega t)$; thus,

$$\nabla \times \underline{E} = i\omega\mu_0 \underline{H} \quad (2-1)$$

$$\nabla \times \underline{H} = -i\omega\epsilon \underline{E} \quad (2-2)$$

A scattering object is represented by considering the permeability ϵ to be a function of position. To solve Eqs. 2-1 and 2-2, let the total fields \underline{E} and \underline{H} be decomposed into incident fields, without the scatterer, and the scattered fields; thus,

$$\underline{E} = \underline{E}^I + \underline{E}^S \quad (2-3)$$

$$\underline{H} = \underline{H}^I + \underline{H}^S \quad (2-4)$$

where the I superscript denotes incident, and the s denotes scattered.

Note that

$$\nabla \times \underline{E}^I = i\omega\mu_0 \underline{H}^I \quad (2-5)$$

$$\nabla \times \underline{H}^I = -i\omega\epsilon_0 \underline{E}^I \quad (2-6)$$

Now rewrite Equation 2-2, with $\epsilon = \epsilon + \epsilon_0 - \epsilon_0$, subtract Equation 2-5 from Eq. 2-1 and Eq. 2-6 from Eq. 2-2, and obtain

$$\nabla \times \underline{E}^S = i\omega\mu_0 \underline{H}^S \quad (2-7)$$

$$\nabla \times \underline{H}^S = -i\omega\mu_0 \underline{E}^S - i\omega(\epsilon - \epsilon_0)\underline{E} \quad (2-8)$$

Eqs. 2-7 and 2-8 show that \underline{E}^S and \underline{H}^S satisfy the free space form of Maxwell's equations, except for the term $-i\omega(\epsilon - \epsilon_0)\underline{E}$, which is a polarization current

$$\underline{J} = -i\omega\epsilon_0 (\kappa - 1)\underline{E} \quad (2-9)$$

where κ is the dielectric constant. If we apply the equation of continuity, the polarization charge is

$$\rho = -\epsilon_0 \nabla \cdot (\kappa - 1) \underline{E} \quad (2-10)$$

A wave equation for \underline{E}^S results by applying the curl operation to Equation 2-7 and eliminating \underline{H}^S with Equation 2-8. Thus

$$\nabla \times \nabla \times \underline{E}^S - k_0^2 \underline{E}^S = k_0^2 (\kappa - 1) \underline{E} = i\omega \mu \underline{J} \quad (2-11)$$

Notice that the left side contains \underline{E}^S but the right side has \underline{E} . Since Eq. 2-11 can be expressed with \underline{J} on the right side to replace \underline{E} , we expect to derive \underline{E}^S from potentials as

$$\underline{E}^S = -\nabla \Phi + i\omega \underline{A}, \quad (2-12)$$

where the potentials are

$$\Phi = (4\pi\epsilon_0)^{-1} \int \rho g \, dv \quad (2-13)$$

$$\underline{A} = (\mu_0/4\pi) \int \underline{J} g \, dv \quad (2-14)$$

and g is the free space, scalar Green's function $r^{-1} \exp ikr$, with r the distance between integration and observation points.

Although the field in Eq. 2-12 seems intuitive with the currents in Eqs. 2-13 and 2-14, the classical deviations⁹ start with wave equations (like Equation 2-11) that contain a single field quantity such as \underline{E}^S , not \underline{E}^S and \underline{E}^I . The use of \underline{J} suppresses this distinction, which may be questionable when differential operators are used to derive Equations 2-13 and 2-14 from Equation 2-11. Therefore we give a direct integration of Equation 2-11. The procedure follows that of Stratton and Chu¹⁰.

In Eq. 2-11 let \underline{P} represent \underline{E}^S , $\underline{Q} = \psi \underline{a}$ where ψ is g or $r^{-1} \exp ikr$, and \underline{a} is an arbitrary constant vector. Apply Green's identity.

$$\int_V (\underline{Q} \cdot \nabla \times \nabla \times \underline{P} - \underline{P} \cdot \nabla \times \nabla \times \underline{Q}) \, dV = \int_S (\underline{P} \times \nabla \times \underline{Q} - \underline{Q} \times \nabla \times \underline{P}) \cdot \underline{n} \, dA \quad (2-15)$$

The left side can be written as

$$\underline{a} \cdot \left[k_0^2 \int_V (\kappa - 1) \underline{E} \, dV - \nabla \cdot \int_V \nabla \cdot (\kappa - 1) \underline{E} \, dV \right] - \int_S (\underline{n} \cdot \underline{E}^S) (\underline{a} \cdot \nabla \psi) \, dA = \text{L.S.} \quad (2-16)$$

where the integration is bounded by a large sphere and by a small sphere about the observation point. The derivation used the facts that $\nabla \cdot \underline{E}^S$ is $\nabla \cdot (\kappa-1)\underline{E}$ and the identity

$$\underline{E}_s \cdot \nabla (\underline{a} \cdot \nabla \varphi) = \nabla \cdot [(\underline{a} \cdot \nabla \varphi) \underline{E}^S] - (\underline{a} \cdot \nabla \varphi) \nabla \cdot \underline{E}^S$$

For the right side we obtain

$$\text{R.S.} = \underline{a} \cdot \int_S \left[\nabla \varphi \times (\underline{E}^S \times \underline{n}) + i\omega\mu_0 (\underline{n} \times \underline{H}^S) \right] dA \quad (2-17)$$

From Equations 2-15, 2-16 and 2-17, we obtain

$$k_0^2 \int_V (\kappa-1) \varphi dV - \nabla' \int_V \varphi \nabla \cdot (\kappa-1) \underline{E} dV = \int_S \left[(\underline{n} \cdot \underline{E}^S) \nabla \varphi + \nabla \varphi \times (\underline{E}^S \times \underline{n}) + i\omega\mu_0 \varphi (\underline{n} \times \underline{H}^S) \right] dA \quad (2-18)$$

The right side of Eq. 2-18 tends to $4\pi \underline{E}^S$ when integrations are done over a large sphere and over a small sphere about the observation point. The integral over the large sphere tends to zero because of the properties of g and the fields, and the integration over the small sphere gives $4\pi \underline{E}^S$. We obtain

$$4\pi \underline{E}^S = k_0^2 \int (\kappa-1) g \underline{E} dV - \nabla' \int g \nabla \cdot [(\kappa-1) \underline{E}] dV \quad (2-19)$$

which is the result obtained by assuming Equations 2-9, and 2-12 through 2-14 as a starting point.

The integral equation for the electric field is obtained from the definition of the scattered field in Equation 2-3.

The integral equation is

$$\underline{E} - \underline{E}^S = \underline{E}^I$$

where \underline{E}^S is given by Equation 2-19.

2.2 SIMULTANEOUS ALGEBRAIC EQUATIONS

The integral equation is solved for the interior of the dielectric object by changing it to a set of simultaneous algebraic equations. A hollow cylinder is divided into rings and subdivided into cells as in Figures 2-1, 2-2 and 2-3. A hollow cone is subdivided into rings as in Figures 2-4 and 2-5, and the rings are divided as in Figure 2-3. The integral equation is evaluated at the center of each cell to generate as many equations as there are cells. At the center of a particular cell, labelled with index m , the integral equation for each rectangular component is

$$E_m - E_m^s = E_m^I \quad (2-20)$$

for $1 \leq m \leq N$, where N is the number of cells. E_m^s is a sum of contributions from all cells, so

$$E_m - \sum E_{mn}^s = E_m^I \quad (2-21)$$

This equation is put into matrix form by writing

$$E_m - \sum \left(E_{mn}^s / E_n \right) E_n = E_m^I \quad (2-22)$$

or

$$\sum C_{mn} E_n = E_m^I \quad (2-23)$$

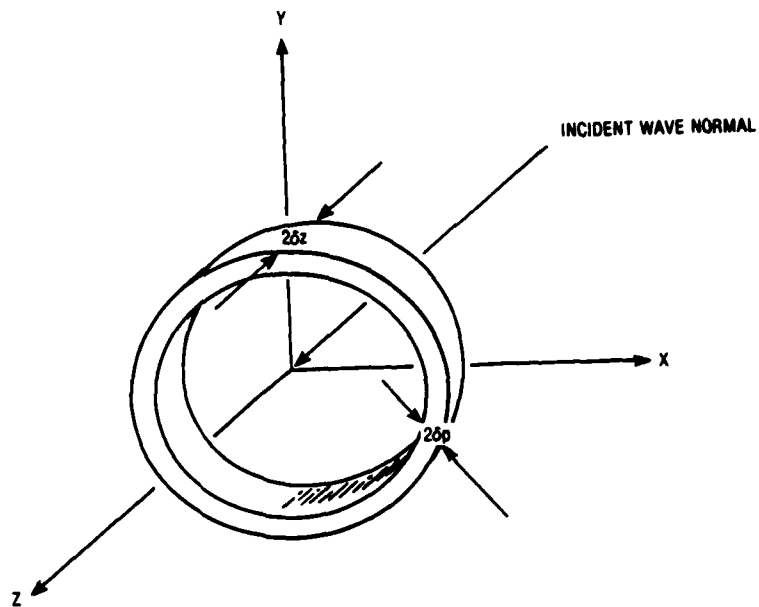
where

$$C_{mm} = 1 - \left(E_{mm}^s / E_m \right), \quad (2-24)$$

and

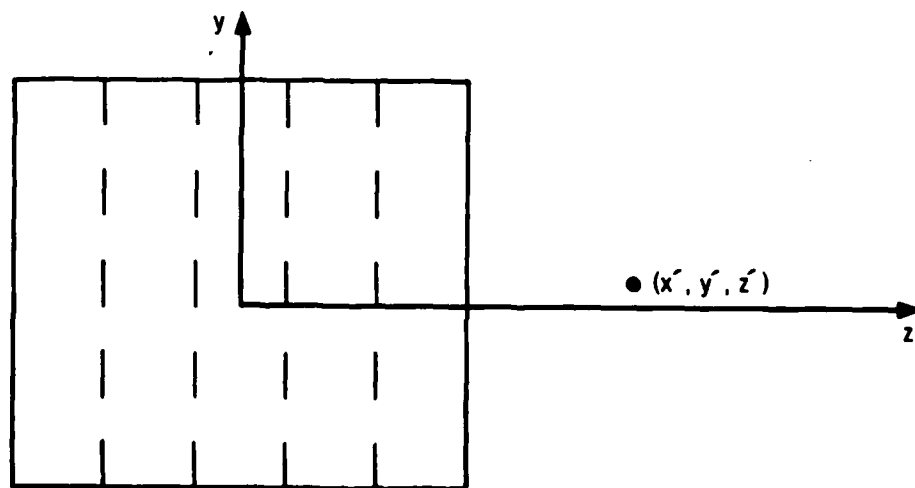
$$C_{mn} = - E_{mn}^s / E_n \quad (2-25)$$

The next step is to evaluate the scattered fields E_{mn}^s . Formulas are derived in the following sections. Diagonal and off-diagonal matrix elements are separately given, and the vector and scalar potentials are separately evaluated.



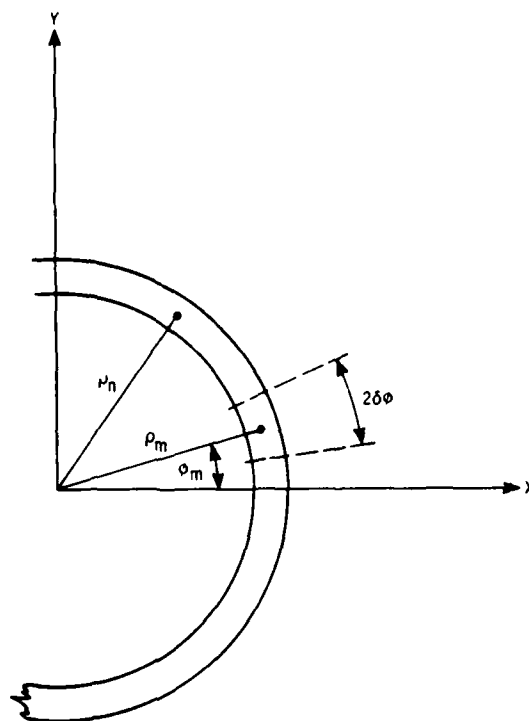
ADR002

Figure 2-1. Dielectric Ring and Coordinate System



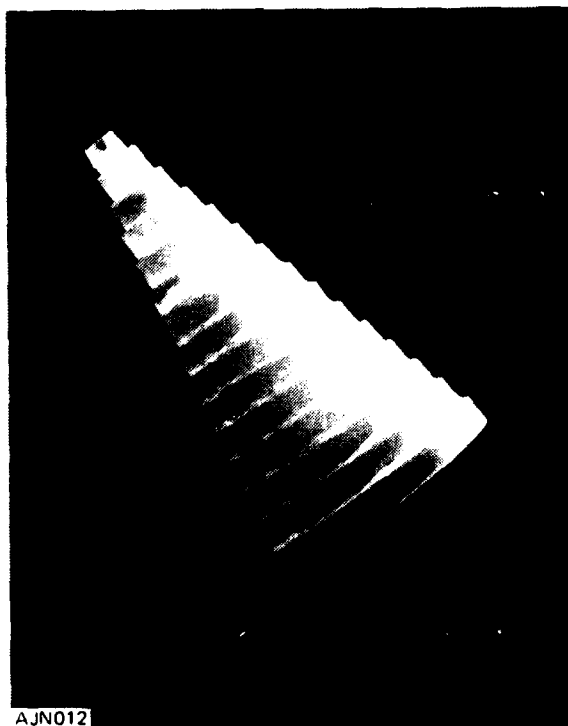
ADR004

Figure 2-2. Subdivision of Hollow Cylinder Into Rings. An observation point has coordinates (x', y', z') ; it may be inside or outside the cylinder.



ADR003A

Figure 2-3. Coordinates for a Cell. A typical cell has dimensions as follows: radial $2\delta\rho$, circumferential $2\delta\phi$ and longitudinal $2\delta z$



AJN012

Figure 2-4. Hollow Cone Composed of Rings. Half angle is 14° . Dielectric Constant was 2.6.

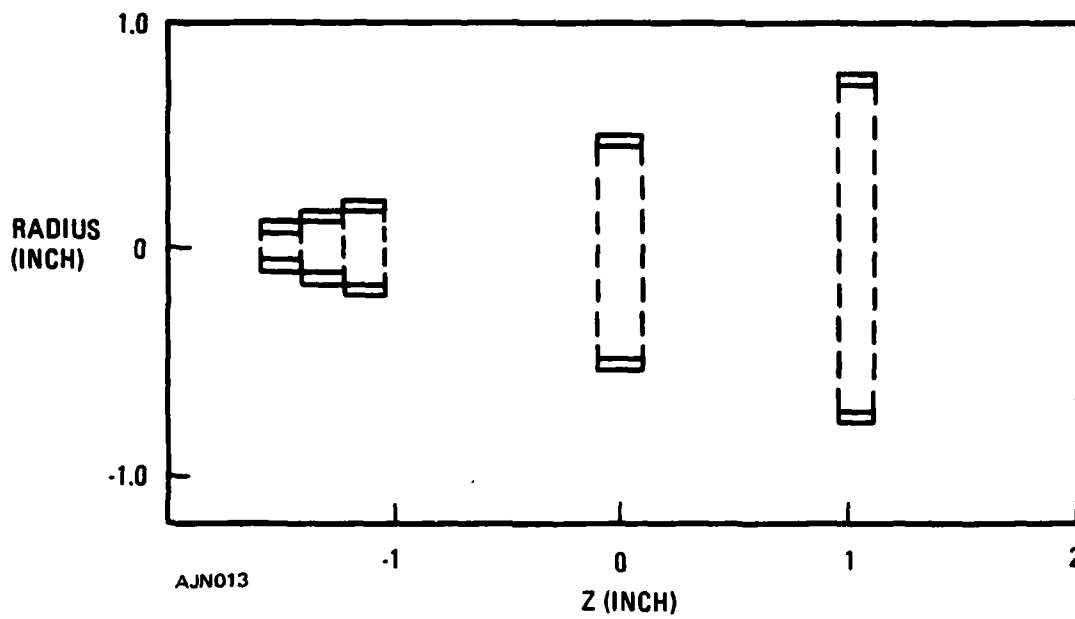


Figure 2-5. Dimensions of Rings. Cell lengths $2\delta z$ were 0.215".
Thickness $2\delta p$ were 0.065".

2.3 SCATTERED FIELD FOR DIAGONAL ELEMENTS

2.3.1 VECTOR POTENTIAL

The scattered field from the vector potential is

$$\underline{E}^s = k^2 (\kappa - 1) (4\pi)^{-1} \int g \underline{E} dV. \quad (2-26)$$

Let us assume horizontal polarization both incident and within the ring. This assumption is reasonable for thin rings and axial incidence. For the cell labelled m we have

$$E_{xm}^s = k^2 (\kappa - 1) (4\pi)^{-1} \int g E_x dV_m \quad (2-27)$$

To simplify notation let

$$I_{Am} = \int g E_x dV_m \quad (2-28)$$

Since the integration extends only over the cell labelled m,

$$r = \left[\rho^2 + \rho_m^2 - 2\rho\rho_m \cos(\phi - \phi_m) + (z - z_m)^2 \right]^{1/2} \quad (2-29)$$

with integration limits $\rho_m - \delta\rho \leq \rho \leq \rho_m + \delta\rho$, $z_m - \delta z \leq z \leq z_m + \delta z$, $\phi_m - \delta\phi \leq \phi \leq \phi_m + \delta\phi$. Introduce abbreviations $\theta = \phi - \phi_m$, $\zeta = z - z_m$, and $\sigma = \rho - \rho_m$. Then on assuming $\phi - \phi_m$ is small, we have

$$r \approx r_m = \left(\sigma^2 + \rho_m^2 \theta^2 + \zeta^2 \right)^{1/2}, \quad (2-30)$$

so that

$$I_{Am} = \int_{-\delta z}^{\delta z} \int_{-\delta\phi}^{\delta\phi} \int_{-\delta\rho}^{\delta\rho} E_x r_m^{-1} e^{ikr_m} (\rho_m + \sigma) \cos \theta d\sigma d\theta d\zeta. \quad (2-31)$$

The factor $\cos \theta$ in the integrand arises from first expressing the x-component of field in polar coordinates, expanding $\cos(\theta + \phi_m)$ and $\sin(\theta + \phi_m)$, and then using small angle approximations for $\sin \theta$ and $\cos \theta$. Now assume r_m is small; that is, σ and ζ are small. Moreover, assume E_x is constant E_m in the cell. Thus we can expand the exponential, to obtain

$$I_{Am} = I_{Am}^{(1)} + I_{Am}^{(2)} ; \quad (2-32)$$

where

$$I_{Am}^{(2)} = ik E_m \int_{-\delta z}^{\delta z} \int_{-\delta \phi}^{\delta \phi} \int_{-\delta \rho}^{\delta \rho} (\rho_m + \sigma) \cos \theta d\sigma d\theta d\zeta \quad (2-33)$$

This integral is, if we omit σ in $\rho_m + \sigma$,

$$I_{Am}^{(2)} = ik (8 \delta z \delta \rho \rho_m \delta \phi) E_m \quad (2-34)$$

The factor in parentheses is the volume of the cell.

The term $I_{Am}^{(1)}$ is more complicated. We omit limits, which equal those in Equation 2-31

$$I_{Am}^{(1)} = \iiint [(\rho_m + \sigma) \rho_m \theta^2 + \sigma^2 + \zeta^2]^{-1/2} (\rho_m + \sigma) \cos \theta d\sigma d\theta d\zeta E_m \quad (2-35)$$

The integral over ζ leads to a logarithmic function so

$$I_{Am}^{(1)} = \iint (\rho_m + \sigma) \cos \theta \log [(R-1)/(R-1)] d\sigma d\theta E_m \quad (2-36)$$

where R is $\left[1 + \left(s_+^2/\delta z^2\right)\right]^{1/2}$, and

where s_+ is $\left[\sigma^2 + (\rho_m + \sigma) \rho_m \theta^2\right]^{1/2}$. Assuming $s_+^2 \ll \delta z^2$, to expand the square root, we obtain

$$\begin{aligned} I_{Am}^{(1)} &= \iint (\rho_m + \sigma) \cos \theta \log \left\{ 4\delta z^2 s_+^{-2} \left[1 + (s_+/2\delta z)^2\right] \right\} d\sigma d\theta E_m \quad (2-37) \\ &= \iint (\rho_m + \sigma) \cos \theta \log (2\delta/s_+)^2 d\sigma d\theta E_m \\ &\quad + \iint (s_+/2\delta z)^2 (\rho_m + \sigma) \cos \theta d\sigma d\theta E_m \end{aligned}$$

We assume that $\cos \theta \approx 1$ and $\sigma \ll \rho_m$ to carry out the integrals. We finally have that the x component of the scattered field is

$$I_{Am}^{(1)} = \pi s_+^2 [1 - \log (s/2\delta z)^2] + \rho_m \frac{\delta \rho \delta \phi}{3\delta z} s_+^2, \quad (2-38)$$

where

$$s_2^2 = \delta \rho^2 + \rho_m^2 \delta \phi^2$$

Equations (2-27), (2-32), (2-34) and (2-38) give the scattered field in the cell labelled m

$$E_{Am}^s = k^2 (\kappa-1) \left\{ i \frac{2}{\pi} k \delta z \delta \rho \rho_m \delta \phi + \frac{\rho_m}{12\pi \delta z^2} \delta \rho \delta \phi s_2^2 - \frac{s_2^2}{4} \left[1 - \log (s_2/2\delta z)^2 \right] \right\} E_m \quad (2-39)$$

For brevity we omit the details of the integrations over σ and θ . The integral was done by integrating over local polar coordinates. In effect then our cells are small right circular cylinders not the truncated wedges defined by $\rho_m d\theta d\sigma$. This approximation procedure is described near the end of Paragraph 2.3.

2.3.2 SCALAR POTENTIAL

The scattered field from the scalar potential is

$$\tilde{E}_s^s = \frac{1}{4\pi} \nabla' I_2 \quad (2-40)$$

where

$$I_2 = \int g \nabla \cdot (\kappa-1) \tilde{E} dV \quad (2-41)$$

To represent the dielectric constant we use the unit step functions as functions of ρ only. That is, we shall understand,

$$(\kappa-1) = (\kappa-1) [H(\rho_m - \delta\rho) - H(\rho_m + \delta\rho)] \quad (2-42)$$

where on the right side $(\kappa-1)$ is a constant, but on the left κ is a function of ρ . Because we have assumed $E_z = 0$, it is unnecessary to specify the z dependence. Finally, κ is assumed independent of ϕ . Therefore

$$I_2 = \int \frac{e^{ikr}}{r} \nabla \cdot (\kappa-1) [H(\rho_m - \delta\rho) - H(\rho_m + \delta\rho)] \tilde{E} \left(\frac{1}{r} \cos \phi - \frac{1}{\phi} \sin \phi \right) dV \quad (2-43)$$

where $\frac{1}{r}$ and $\frac{1}{\phi}$ are unit vectors in the r and ϕ directions respectively.

We assume $\text{div } E = 0$, in the cell so

$$I_2 = (\kappa-1) E_m \left(I_2^{(1)} - I_2^{(2)} - I_2^{(3)} \right), \quad (2-44)$$

where

$$I_2^{(1)} = \int g \delta (\rho_m - \delta \rho) \cos \phi \, dV_m, \quad (2-45)$$

$$I_2^{(2)} = \int g \delta (\rho_m - \delta \rho) \cos \phi \, dV_m, \quad (2-46)$$

$$I_2^{(3)} = \int g \cos \phi \, d\rho \, d\phi \, dz. \quad (2-47)$$

The first two integrals, $I_2^{(1)}$ and $I_2^{(2)}$, approximately cancel. To see this consider $I_2^{(1)}$. Assume kr is small and expand $\exp ikr$. Thus

$$I_2^{(1)} = \int (r^{-1} + ik) \delta (\rho_m - \delta \rho) \cos \phi \, dV_m$$

The second term of the integrand, with factor ik , gives $-4ik (\rho_m - \delta \rho) \delta z \delta \phi \cos \phi_m$. This term is omitted because it approximately cancels the term $-4ik (\rho_m + \delta \rho) \delta z \delta \phi$ that arises from $I_2^{(2)}$. The first term with factor r^{-1} , gives

$$I_2^{(1)} = \left(1 - \frac{\delta \rho}{\rho_m}\right) \cos \phi_m \int \left[\left(\zeta/\rho_m\right)^2 + (\delta \rho/\rho_m)^2 + \left(1 - \frac{\delta \rho}{\rho_m}\right) \theta^2 \right]^{-1/2} \cos \theta \, d\theta \, d\zeta; \quad (2-48)$$

recall θ and ζ were defined earlier. Following integration on ζ we have

$$I_2^{(1)} = \left(1 - \frac{\delta \rho}{\rho_m}\right) \cos \phi_m \int (\ln P_+ - \ln P_-) \cos \theta \, d\theta \, d\zeta \quad (2-49)$$

where

$$P_{\pm} = \frac{q \pm \delta z}{\rho_m} + \frac{(\rho_m - \delta \rho) \theta^2}{2q} \quad (2-50)$$

and

$$q = \sqrt{\delta z^2 + \delta \rho^2} \quad (2-51)$$

The evaluation of $I_2^{(2)}$ proceeds in the same way. The result is that

$$I_2^{(2)} = \left(1 + \frac{\delta \rho}{\rho_m}\right) \cos \phi_m \int (\ln Q_+ - \ln Q_-) \cos \theta \, d\theta \, d\zeta \quad (2-52)$$

where

$$Q_{\pm} = \frac{(q \pm \delta z)}{\rho_m} + \frac{(\rho_m + \delta \rho) \theta^2}{2q} \quad (2-53)$$

Now consider

$$I_2^{(1)} - I_2^{(2)} = \left(1 - \frac{\delta \rho}{\rho_m}\right) \int \ln(L_+/L_-) d\theta \quad (2-54)$$

where

$$L_{\pm} = \frac{s^2 - \delta z^2}{\rho_m^2} + \theta^2 + \frac{\rho_m^2 - \delta \rho^2}{4s^2} \theta^4 \pm \frac{\delta z}{s} \frac{\delta \rho}{\rho_m} \theta^2. \quad (2-55)$$

Inspection of L_+/L_- shows that it tends to unit value for small θ . For example, at $\theta = 0$ the value is 1; for $\theta = 0.2$, the value is 1.046. Therefore the logarithm is small so the contributions of $I_2^{(1)}$ and $I_2^{(2)}$ from E_{Am}^s are omitted.

To evaluate $I_2^{(3)}$, expand the exponential, $\exp ikr$, in the integrand as $1 + ikr$. The first term is omitted because it is independent of the observation point coordinates so the ∇ operator yields zero. From the second term we obtain

$$I_2^{(3)} = \int r^{-1} \cos \phi \, d\rho \, d\phi \, dz \quad (2-56)$$

Again we use substitution $z - z_m = \zeta$, $\rho - \rho_m = \sigma$, $\phi - \phi_m = \theta$ to obtain

$$I_2^{(3)} = \cos \phi_m \iiint \left[\sigma^2 + (\rho_m + \sigma) \rho_m \theta^2 + \zeta^2 \right]^{-1/2} \cos \theta \, d\rho \, d\theta \, d\zeta. \quad (2-57)$$

We assume θ is small so $\cos \theta \approx 1$. Integration on ζ gives

$$I_2^{(3)} = \cos \phi_m \iint \log \left\{ \left[1 + \frac{(\rho_m + \theta) \rho_m \theta^2 + \sigma^2}{4\delta z^2} \right] \frac{4\delta z^2}{[(\rho_m + \theta) \rho_m \theta^2 + \sigma^2]} \right\} d\sigma \, d\theta \quad (2-58)$$

Because wall thickness is much smaller than radius, we omit the term

$$\sigma \rho_m \theta^2 / 4\delta z$$

in the integrands. The integrations on σ and θ give

$$I_2^{(3)} = \pi \rho_m^{-1} \cos \phi_m \left[1 - \log(s_m / 2\delta z)^2 \right] s_m^2 + \frac{\delta \rho \delta \phi (\delta z)^{-2}}{3} s_m^2 \cos \phi_m \quad (2-59)$$

where

$$s_m^2 = \left(\delta \rho^2 + \rho_m^2 \delta \phi^2 \right).$$

To obtain the field apply the ∇' operator to $I_2^{(3)}$. The ρ and ϕ components are as follows:

$$\begin{aligned} \left(E_{\phi m}^S \right)_\rho = & - (\kappa-1) \left\{ \frac{\delta \phi^2}{2} \left[1 + \left(1 - \log \left(\frac{s}{2} \right)^2 \delta z^{-2} \right) \left(1 - \frac{s^2}{2} \rho_m^{-2} \delta \phi^{-2} \right) \right. \right. \\ & \left. \left. + \frac{\delta \rho \rho_m \delta \phi}{3\pi \delta z^2} \right] \cos \phi_m \right\} E_{xm} \end{aligned} \quad (2-60)$$

$$\left(E_{\phi m}^S \right)_\phi = - (\kappa-1) \left(\frac{s}{2\rho_m} \right)^2 \left\{ \left[1 - \log \frac{s}{2\delta z} \right] + \frac{\rho_m \delta \rho \delta \phi}{3\pi \delta z^2} \right\} \sin \phi_m E_{xm} \quad (2-61)$$

From Equations 2-60 and 2-61, the contribution of the scalar potential to the x component of the scattered field is

$$\begin{aligned} E_{xm}^S(\Phi) = & - (\kappa-1) \left\{ \frac{\delta \phi^2}{2} \left[1 + d \left(1 - \frac{s^2}{2\rho_m^2 \delta \phi^2} \right) + f \right] \cos^2 \phi_m \right. \\ & \left. + \left(\frac{s}{2\rho_m} \right)^2 (d + f) \sin^2 \phi_m \right\} E_{xm} \end{aligned} \quad (2-62)$$

where

$$d = 1 - \log \left(\frac{s}{2} \right)^2 \quad (2-63)$$

and

$$f = \rho_m \delta \rho \delta \phi / (3\pi \delta z)^2 \quad (2-64)$$

2.4 SCATTERED FIELD FOR OFF DIAGONAL ELEMENTS

2.4.1 VECTOR POTENTIAL

The scattered field is

$$\underline{E}^s = k^2 (\kappa - 1) (4\pi)^{-1} \int g \underline{E} dV \quad (2-65)$$

where the integral extends over the shell, and g is $r^{-1} \exp ikr$, where r is the distance between integration and observation points. The shell is subdivided into cells, as shown in Figures 2-1 and 2-3; the subdivision is into rings, defined by increments along the z -axis of symmetry, and further division of each ring into angular sectors. The center of a cell has coordinates (ρ_m, ϕ_m, z_m) for an internal observation point; integration cells have coordinates (ρ_n, ϕ_n, z_n) . In these coordinates

$$r^2 = \rho^2 + \rho_m^2 - 2\rho\rho_m \cos(\phi - \phi_m) + (z - z_m)^2. \quad (2-66)$$

We let $\rho = \rho_n + \sigma$, $z = z_n + \zeta$, and $\phi = \phi_n + \theta$, and utilize a binomial expansion so that

$$r = B + \sigma [] B^{-1} + \zeta(z_n - z_m) B^{-1}, \quad (2-67)$$

where $B^2 = \rho_n^2 + \rho_m^2 - 2\rho_n \rho_m \cos(\phi_n - \phi_m) + (z_n - z_m)^2$.

and $[] = \rho_n - \rho_m \cos(\phi_n - \phi_m)$.

For horizontal polarization and axial incidence the volume integral

$$I = \int g E_x dV \quad (2-68)$$

becomes

$$I = \sum_n e^{ikB} B^{-1} \rho_n E_n \int e^{ik\sigma [] / B} e^{ik\zeta(z_n - z_m) / B} d\sigma d\zeta (2\delta\phi) \quad (2-69)$$

where the integral over ϕ yielded $2\delta\phi$. We also approximated the factor $\rho_n + \sigma$ which multiplies the exponentials by ρ_n . This approximation means that radome thickness is smaller than radius. We obtain

$$E_x^s = k^2 (\kappa - 1) (2/\pi) \delta\rho\delta\phi\delta z \sum E_n \rho_n e^{ikB} B^{-1} \text{sinc} \left\{ k [] \delta\rho B^{-1} \right\} \text{sinc} \left\{ k z_{nm} \delta z B^{-1} \right\} \quad (2-70)$$

where z_{nm} is $z_n - z_m$, and $\text{sinc} z$ is $z^{-1} \sin z$.

2.4.2 SCALAR POTENTIAL

The scalar potential generates a scattered field

$$E_s^s = (4\pi)^{-1} \nabla' I_2 \quad (2-71)$$

where

$$I_2 = \int g \nabla \cdot (\kappa - 1) \underline{E} dV, \quad (2-72)$$

and ∇' is taken at the observation point. The integral extends over the cells described in the preceding section, so

$$I_2 = \sum_n \int g \nabla \cdot (\kappa - 1) \underline{E}_n dV. \quad (2-73)$$

The function $(\kappa - 1)$ is constant within the dielectric and thus in every cell; it depends only on radius, which changes from one cell to another. We describe the inner and outer radii by step functions so that

$$(\kappa - 1) = |\kappa - 1| \left[H(\rho_n - \delta\rho) - H(\rho_n + \delta\rho) \right], \quad (2-74)$$

where $H(x)$ is zero for x negative and unity for x positive, and ρ_n is the radius of the cell with index n . For horizontal polarization we obtain

$$I_2 = \int g \nabla \cdot \left\{ |\kappa - 1| \left[H(\rho_n - \delta\rho) - H(\rho_n + \delta\rho) \right] E_{on} (c \phi \underline{1}_\rho - s \phi \underline{1}_\phi) \right\} dV, \quad (2-75)$$

where $\underline{1}_\phi$, and $\underline{1}_\rho$ are unit vectors. The symbols $|\kappa - 1|$ denote the magnitude of the dielectric constant within the dielectric.

Within the dielectric cells we assume $\nabla \cdot \underline{E}$ is zero because the field is assumed constant. The derivative on ρ of the divergence operator leads to Dirac δ functions, but the derivative on ϕ operates only on $\sin \phi$,

because $\kappa - 1$ is independent of ϕ . We obtain

$$I_2 = |\kappa - 1| \sum E_n I_{2n}, \quad (2-76)$$

where the integral over any cell is

$$I_{2n} = |\kappa - 1| \left[I_{2n}^{(1)} - I_{2n}^{(2)} - I_{2n}^{(3)} \right] \quad (2-77)$$

where

$$I_{2n}^{(1)} = \int g \delta(\rho_n - \delta\rho) \cos \phi \rho d \rho d \phi dz; \quad (2-78)$$

$$I_{2n}^{(2)} = \int g \delta(\rho_n + \delta\rho) \cos \phi \rho d \rho d \phi dz; \quad (2-79)$$

$$I_{2n}^{(3)} = \int g \cos \phi d \rho d \phi dz. \quad (2-80)$$

As before

$$r = [\rho^2 + \rho_m^2 - 2\rho\rho_m \cos(\phi - \phi_m) + (z - z_m)^2]^{1/2}; \quad (2-81)$$

with $z - z_n = \zeta$, and $\rho - \rho_n = \sigma$; a binomial expansion gives

$$r = s + bs^{-1}\sigma + z_{nm}s^{-1}\zeta$$

where b is $\rho_n - \rho_m \cos(\phi_n - \phi_m)$, and z_{nm} is $z_n - z_m$.

To evaluate $I_{2n}^{(3)}$ let ϕ be $\phi_n + \theta$, where θ is small in each cell, so $\cos(\phi_n + \theta)$ is approximately $\cos\phi_n$. The integrals over θ and ϕ are well known, so we have

$$I_{2n}^{(3)} = 8\delta\rho \delta\phi\delta z e^{iks_s^{-1}\cos\phi_n} \text{sinc}(kb\delta\rho s^{-1}) \text{sinc}(kz_{nm}\delta z s^{-1}), \quad (2-82)$$

or approximately

$$I_{2n}^{(3)} = 8\delta\rho\delta\phi\delta z e^{iks_s^{-1}\cos\phi_n} \quad (2-83)$$

For $I_{2n}^{(1)}$, we have

$$\begin{aligned} I_{2n}^{(1)} &= e^{iks_s^{-1}} \int e^{ikb(\sigma/s)} e^{ikz_{nm}(\zeta/s)} \delta(\sigma + \delta\rho) \cos(\phi_n + \theta) d\theta d\zeta \\ &= 4\delta z \delta\phi (\rho_n - \delta\rho) \cos\phi_n e^{iks_s^{-1}} e^{-ikb\delta\rho/s}, \end{aligned} \quad (2-84)$$

where $\text{sinc}(kz_{nm}\delta z/s)$ has been approximated by unit value.

In addition,

$$I_{2n}^{(2)} = 4\delta z \delta\phi (\rho_n + \delta\rho) \cos\phi_n e^{iks_s^{-1}} e^{ikb\delta\rho/s}. \quad (2-85)$$

Therefore

$$I_{2n}^{(1)} - I_{2n}^{(2)} = -8\delta z \delta\phi \cos\phi_n e^{iks_s^{-1}} [\delta\rho \cos(kb\delta\rho/s) + i\rho_n \sin(kb\delta\rho/s)]; \quad (2-86)$$

with small argument approximations, we obtain

$$I_{2n}^{(1)} - I_{2n}^{(2)} = -8\delta z \delta\phi \delta\rho \cos\phi_n e^{iks_s^{-1}} (1 + ik\rho_n bs^{-1}) \quad (2-87)$$

The electric field from $I_{2n}^{(3)}$, Equation 2-83, is given by the gradient in Equation 2-12,

$$E_s^s(I_{2n}^{(3)}) = -(\kappa-1)(4\pi)^{-1} \nabla' I_{2n}^{(3)}. \quad (2-88)$$

The partial derivative on ρ_m gives a radial component,

$$E_{s\rho}^s(I_{2n}^{(3)}) = -(2/\pi)(\kappa-1)\delta\rho\delta\phi\delta z\cos\phi_n e^{iks} s^{-2}(ik-s^{-1})b, \quad (2-89)$$

and differentiation on ϕ_m gives

$$E_{s\phi}^s(I_{2n}^{(3)}) = (2/\pi)(\kappa-1)\delta\rho\delta\phi\delta z\cos\phi_n e^{iks} s^{-2}(ik-s^{-1})\rho_n \sin(\phi_n - \phi_m). \quad (2-90)$$

The x component is

$$E_{sx}^s(I_{2n}^{(3)}) = E_{s\rho}^s(I_{2n}^{(3)})\cos\phi_n - E_{s\phi}^s(I_{2n}^{(3)})\sin\phi_n \quad (2-91)$$

The electric field from $I_{2n}^{(1)} - I_{2n}^{(2)}$ is given by applying the gradient operator to the expression in Equation 2-87. The first term, that is the factor multiplying 1, is identical to $E_{sx}^s(I_{2n}^{(3)})$ in Equation 2-91. The second term gives a radial component

$$E_{s\rho}^s(I_1 - I_2)' = -F e^{iks} s^{-3} b [2bs^{-1} + C_{nm} + ikb] \quad (2-92)$$

when C_{nm} is $\cos(\phi_n - \phi_m)$, and F is $-2(i/\pi)(\kappa-1)k\rho_n\delta z\delta\phi\delta\rho\cos\phi_n$. The prime denotes that the contribution of the first term is absent. The second term gives a ϕ component

$$E_{s\phi}^s(I_1 - I_2)' = -F e^{iks} s^{-2} \sin(\phi_n - \phi_m) [1 + bs^{-1}\rho_n(ik-s^{-1})-b\rho_n s^{-2}] \quad (2-93)$$

If we combine the results we obtain for the x-component:

$$\begin{aligned} E_s^s &= \nabla' \cdot I_{2n}^{(1)} - I_{2n}^{(2)} - I_{2n}^{(3)} \\ &= [-2 s^{-1}(ik-2^{-1})b\cos\phi_m - 2 s^{-1}(ik-s^{-1})\rho_n \sin(\phi_n - \phi_m) \sin\phi_m \\ &\quad + i s^{-2} k \rho_n b [2bs^{-1} + \cos(\phi_n - \phi_m) - ikb] \cos\phi_m \\ &\quad + 1 s^{-1} k \rho_n \sin(\phi_n - \phi_m) [2b \rho_n s^{-2-1} - ibks^{-1} \rho_n] \sin\phi_m] G, \end{aligned} \quad (2-94)$$

where G is $[(2/\pi)|\kappa-1|\delta\rho\delta\phi\delta z\cos\phi_n e^{iks} s^{-1}]$

Equation 2-94 reduces to the formula developed for the hollow cylinder; where all the ρ_n have equal magnitude.

2.5 EXTERNAL FIELDS

The field outside the dielectric region is found by evaluating Equations 2-26 and 2-40. The integration extends over the dielectric region. It can be done after the total field inside the dielectric is determined by solving the integral equation.

The field near a cylinder is evaluated to test the approximations in the derivations. The near field also is useful in understanding the effects of a dielectric cylinder or a radome on an antenna.

The field from the vector potential is

$$E^S(A) = i \omega A.$$

A measurement requires a probe. We consider a half-wave dipole and weight the contribution of each cell by the far-field pattern. To simplify the expressions, consider the field on the z-axis. The vector potential gives for the x component (from one ring)

$$E^S(A_1) = (\kappa-1) k^2 (4\pi)^{-1} \int g E_x \cos\left(\frac{\pi}{2} \cos \theta\right) (\sin \theta)^{-1} \rho d\rho d\phi dz \quad (2-95)$$

where the factor $\cos(\pi/2 \cos \theta)/\sin \theta$ is the far-field pattern of the probe. Consider the distance large enough so that

$$r = R + (a\sigma - a\rho \cos \phi - zz') R^{-1} \quad (2-96)$$

where a is the mean radius of the cylinder and R is $(a^2 + z'^2)^{1/2}$. Furthermore approximate $\sin \theta$;

$$\sin \theta = 1 - (a/R)^2 \cos^2 \phi \quad (2-97)$$

2.5.1 FROM AVERAGE INTERNAL FIELD

To develop a simple formula we omit the dependence of E on ϕ and use an average value E_0 . The integrations are elementary, so that

$$E^S(A_1) = 2 (\kappa-1) k^2 a \delta \rho \delta z E_0 e^{ikR} R^{-1} \text{sinc}(ka \delta \rho/R) \text{sinc}(kz' \delta z/R) P$$

$$P = \left[1 - (a/2R)^2 \left(\frac{\pi^2}{4} - 1 \right) \right]. \quad (2-98)$$

P is the probe correction.

The field from the scalar potential is

$$E_x^S(\Phi) = (4\pi)^{-1} \nabla' \cdot \int g \nabla \cdot (\kappa-1) E_x dV. \quad (2-99)$$

The procedures are like those in Paragraphs 2.3.2 and 2.4.2. So

$$E_{\mathbf{x}}^S(\Phi) = -i(\kappa-1) \frac{a^2}{2\lambda} \frac{e^{ikR}}{R^2} E_0 \int e^{ik(\dots)} [\dots] \cos^2 \phi \, d\sigma \, d\phi \, dz, \quad (2-100)$$

where

$$(\dots) = (a\sigma - a\rho' \cos \phi - zz') R^{-1} \quad (2-101)$$

and

$$[\dots] = [\delta(\sigma + \delta\rho) - \delta(a - \delta\rho) - a^{-1}] . \quad (2-102)$$

After doing the integrals, we have

$$E_{\mathbf{x}}^S(\Phi_1) = i\pi(\kappa-1) a^2 \delta z \delta\rho e^{ikR} (R^2 \lambda)^{-1} \left(\frac{2}{a} + \frac{ika}{R} \right) J_0 \left(\frac{ka\rho'}{R} \right) \text{sinc} \left(\frac{kz' \delta z}{R} \right) P' E_0 \quad (2-103)$$

Note the probe correction P' is $[1 - 3/8 (\pi^2/4 - 1) a^2/R^2]$; it differs from that in Equation 2-98.

The total field is

$$E_{\mathbf{x}}^T = E^I + E_{\mathbf{x}}^S(A) + E_{\mathbf{x}}^S(\Phi) \quad (2-104)$$

The observable quantities are intensity $|E_{\mathbf{x}}^T|^2$ and phase, the argument of $E_{\mathbf{x}}^T$.

This theory does not include the effects of fields reflected from the probe to the scatterer and scattered back to the probe.

The formulas generalize readily to several rings forming a cylinder. For example for two rings

$$E_{\mathbf{x}}^S(A_2) = E^S(A_1) \left(E_{01} e^{ikz' \delta z/R} + E_{02} e^{ikz' \delta z/R} \right) \quad (2-105)$$

where E_{01} and E_{02} are the fields in each of the rings and $E^S(A_1)$ is from Equation 2-98. The scalar potential gives

$$E_{\mathbf{x}}^S(\Phi_2) = E^S(\Phi_2) \left(E_{01} e^{ikz' \delta z/R} + E_{02} e^{ikz' \delta z/R} \right) \quad (2-106)$$

where $E^S(\Phi_2)$ is from Equation 2-102.

2.5.2 FROM CIRCUMFERENTIALLY VARYING INTERNAL FIELD

The external scattered field is computed from a general formula, which gives

$$E^S = A \sum \cos \phi_n (P_n \partial g_n / \partial x_n + g_n \partial P_n / \partial x_n), \quad (2-107)$$

where A is $-4 (\kappa - 1) \delta z \delta \phi \delta \rho / \pi$, the probe correction factor is

$$P = \left[1 - (x_n - x^I)^2 r_n^{-2} \right]^{-1/2} \cos \left[\pi (x_n - x^I) / 2r_n \right],$$

and g_n is g with r_n equal to $[(x_n - x^I)^2 + (y_n - y^I)^2 + (z_n - z^I)^2]^{1/2}$.

3. RESULTS FROM SCALAR GREEN'S FUNCTION METHOD

3.1 CYLINDERS

3.1.1 INTERNAL FIELDS

The first example is a single ring, diameter $2a$ equal λ , length $2\delta z = 0.16\lambda$, dielectric constant 2.6. Because incidence was axial, necessary conditions on the computed results were that the field at $\phi = 0$ equal that at $\phi = \pi$ and that the field at $\phi = \pi/2$ equal that at $\phi = 3\pi/2$. This condition was well satisfied.

Figure 3-1 shows computed internal values of E^T for several values of N ; the graph suggests subdivision into 24 cells is adequate for stable values.

Figure 3-2 shows computed internal values of E^T for a cylinder, also of diameter λ , but with length 0.32λ . Two rings were utilized.

3.1.2 EXTERNAL FIELD FROM CIRCUMFERENTIALLY UNIFORM INTERNAL FIELDS

The approximation of Section 2.5 was utilized to compute external fields. Figure 3-3 shows computed values of E^T outside the ring, on the z -axis, with and without probe

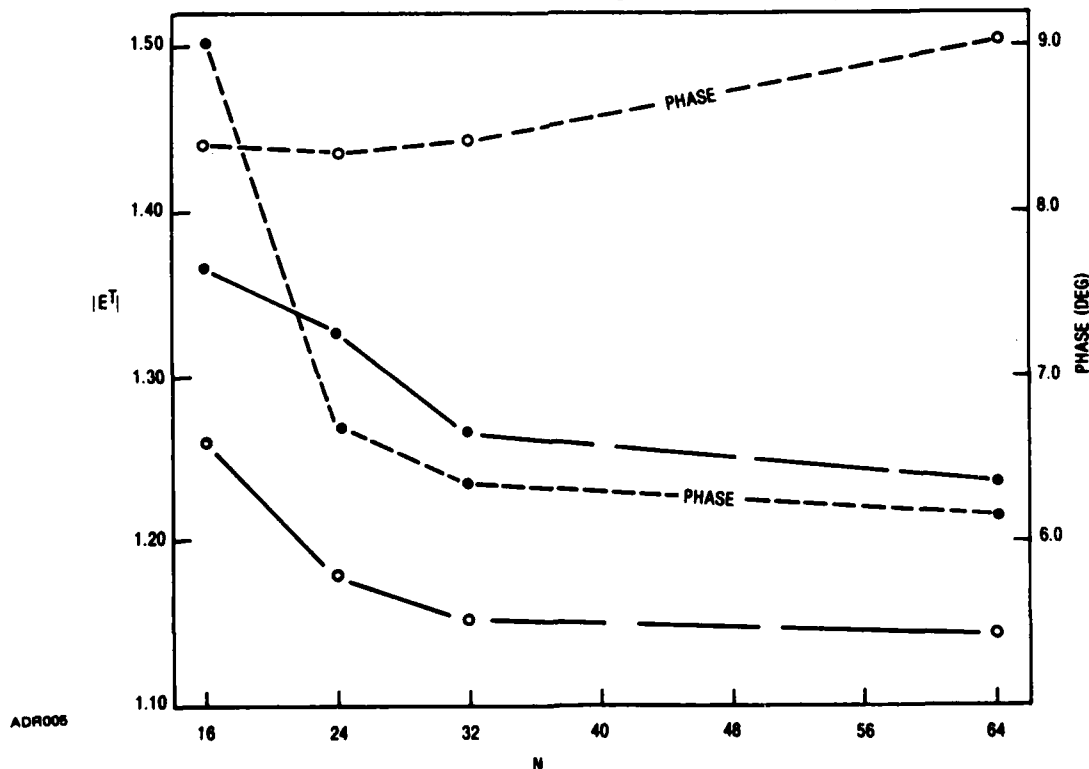


Figure 3-1. Phase and Amplitude of E^T for Single Ring: $\delta z = 0.100$ in., $\delta \rho = 0.030$ in., $x = 2.6$, frequency = 9.375 GHz. For $\phi = 0^\circ$ (o), $\phi = 90^\circ$ (•)

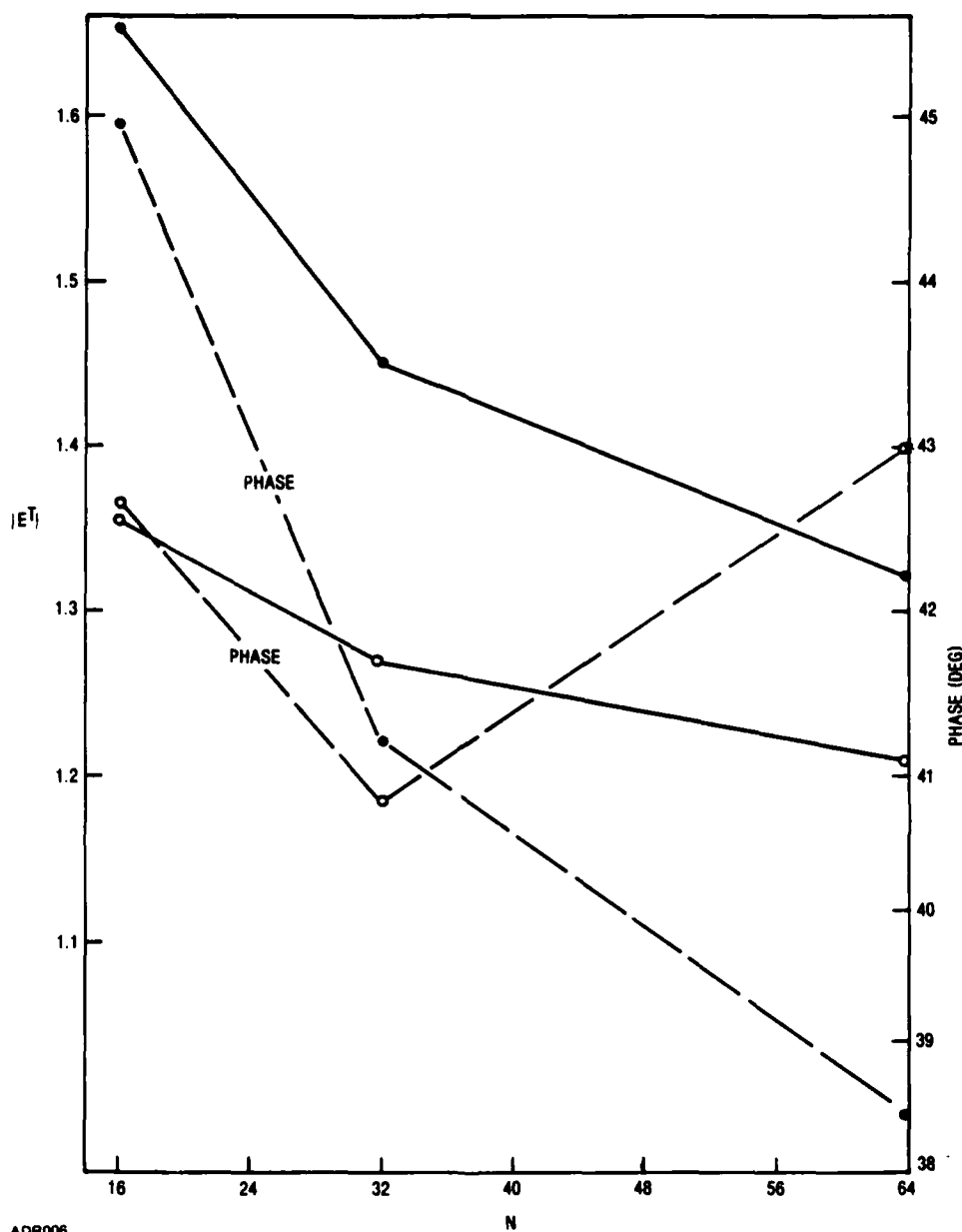
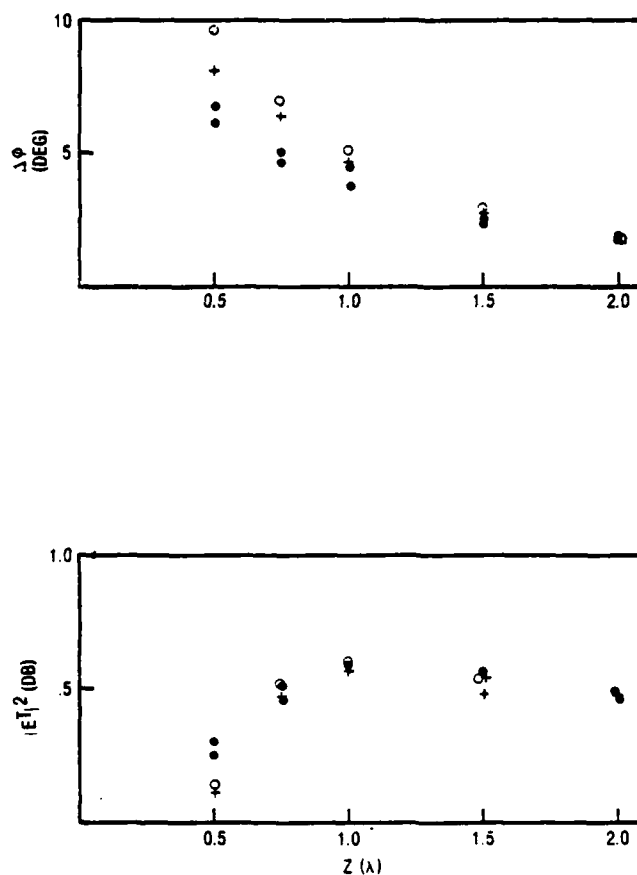


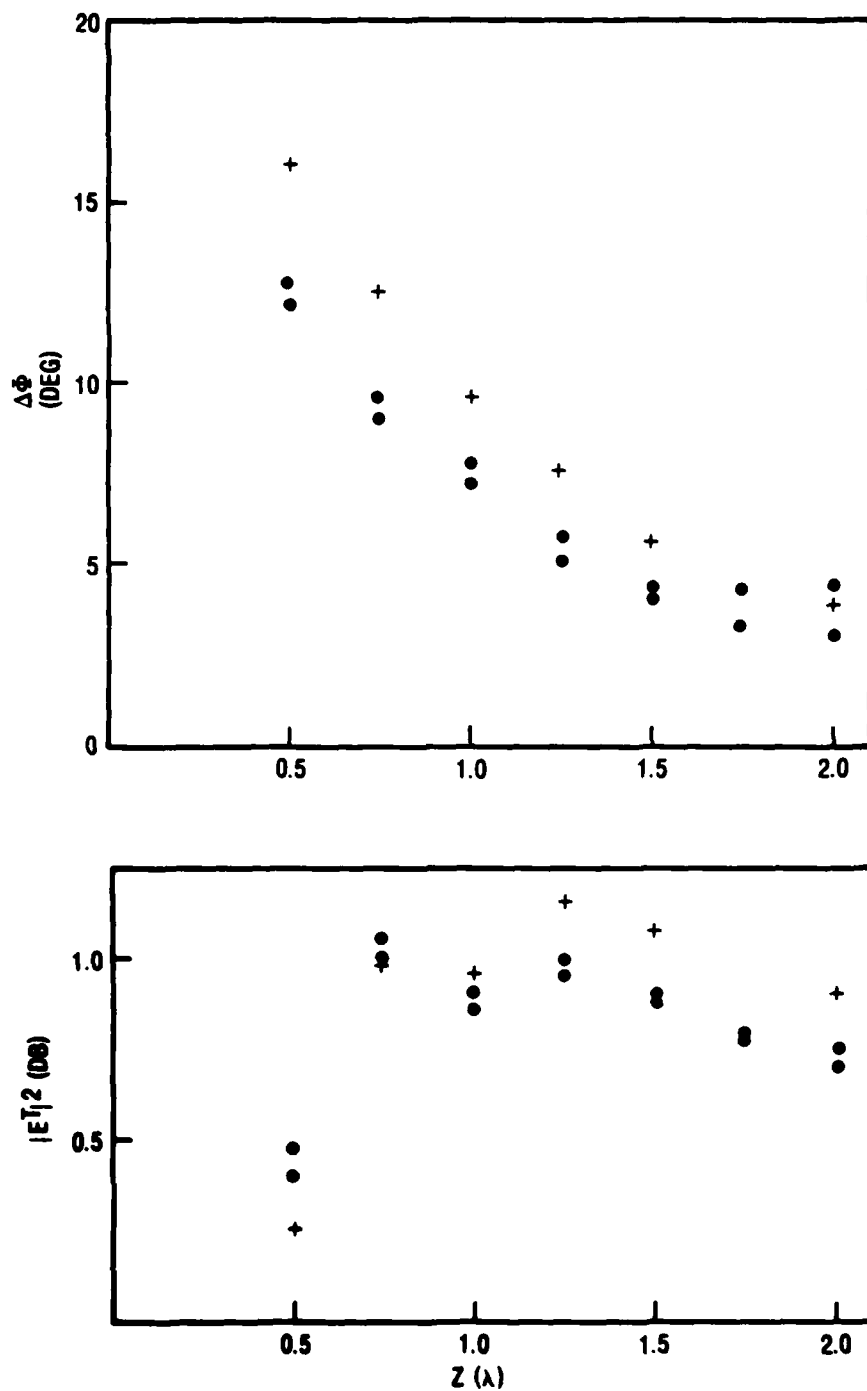
Figure 3-2. Phase and Amplitude of E^T for Two Rings. $\delta z = 0.1045$ in.;
 $\delta \rho = 0.0313$ in. at center of second cell. Symbols as in Figure 3-2.

corrections. Figure 3-4 shows computed value of E^T outside the cylinder. Figure 3-5 shows computed values for the cylinder, but the area of the cylinder cross section was reduced by 80% in evaluating the external field integrals, Equations 2-105 and 2-106. The area reduction makes the volume of the cylinder equal to that of the elementary integration cells.



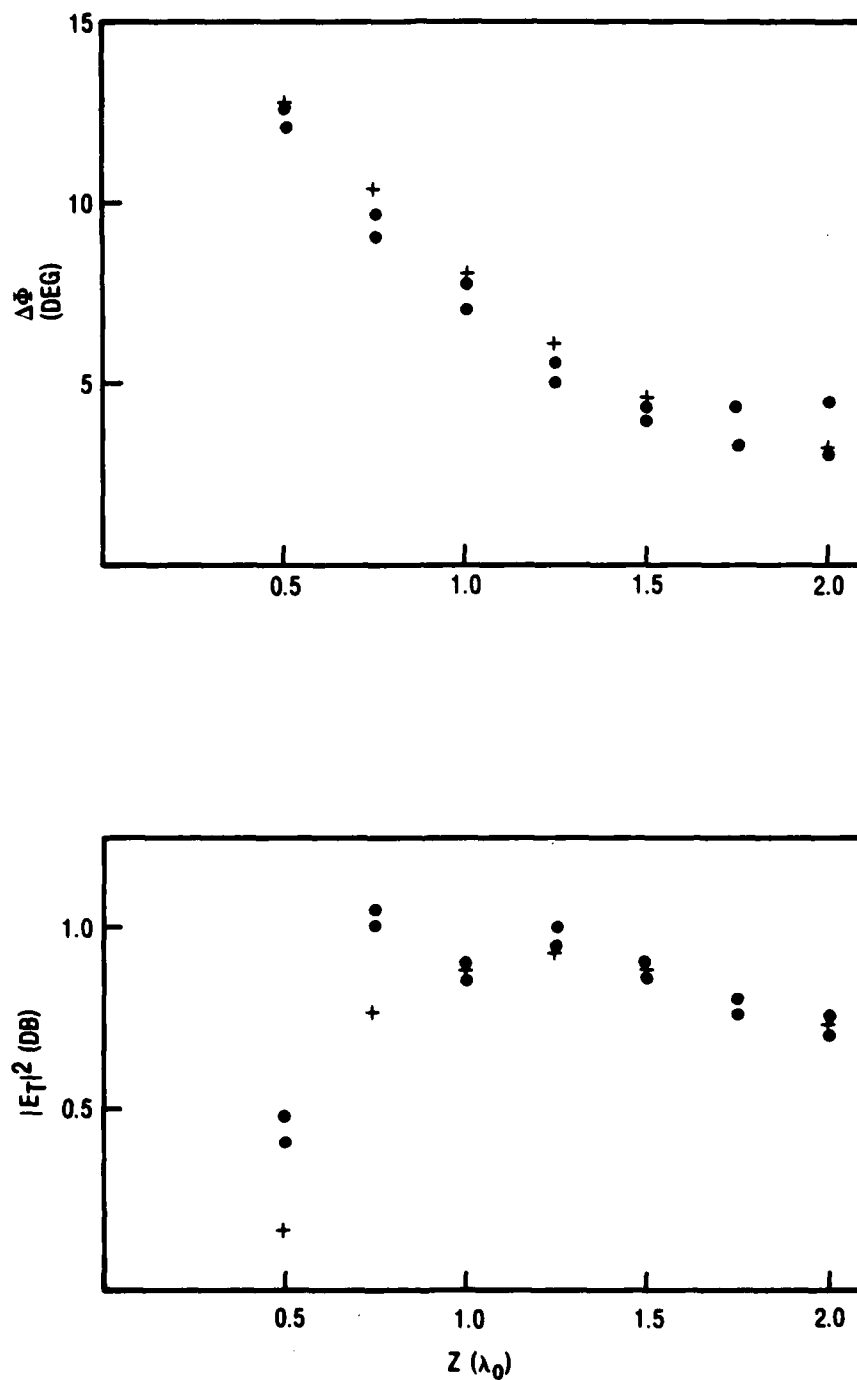
ADR007A

Figure 3-3. Total Field Behind Dielectric Ring. Length: 0.2 in.; thickness $2\delta p$: 0.06 in.; mean diameter $2a$: 1.25 in.; dielectric constant 2.6. Measured with dipole probe: (·); computed without probe corrections (o); computed with probe correction (+). Internal field: $1.19 \exp i 7.8^\circ$ for $N = 64$



AD8008

Figure 3-4. Total Field Outside Dielectric Ring. Length is 0.42 in. with other parameters equaling those in Figure 4-6. Measured (\cdot), calculated with probe correction (+)



ADR009

Figure 3-5. As in Figure 3-4 but with $\delta\rho$ Reduced by 20 Percent

3.1.3 EXTERNAL FIELDS FROM CIRCUMFERENTIALLY VARYING INTERNAL FIELDS

This section gives external field values computed from Equation 2-107, which includes the circumferential variation of the internal field. Figures 3-6 through 3-15 show the intensity $|E^T|^2$ and phase $\Delta\phi$ of the total field on transverse paths at distances 0.5, 0.75, and 1.0 wavelengths from the center of a ring of length $2\delta z = 0.21"$. Incidence was axial.

Figure 3-16 shows axial dependence.

3.1.4 POLARIZATION DEPENDENCE OF INTERNAL FIELDS

Figure 3-17 shows computed values of $|E^T|^2$ inside one or two rings. The graph shows data for a cell in the E-plane and for a cell in the H-plane. The E-plane cells are at the sides of the cylinder, and the H-plane cells are at the top and bottom; recall the field was horizontally polarized. Clearly a polarization dependence exists.

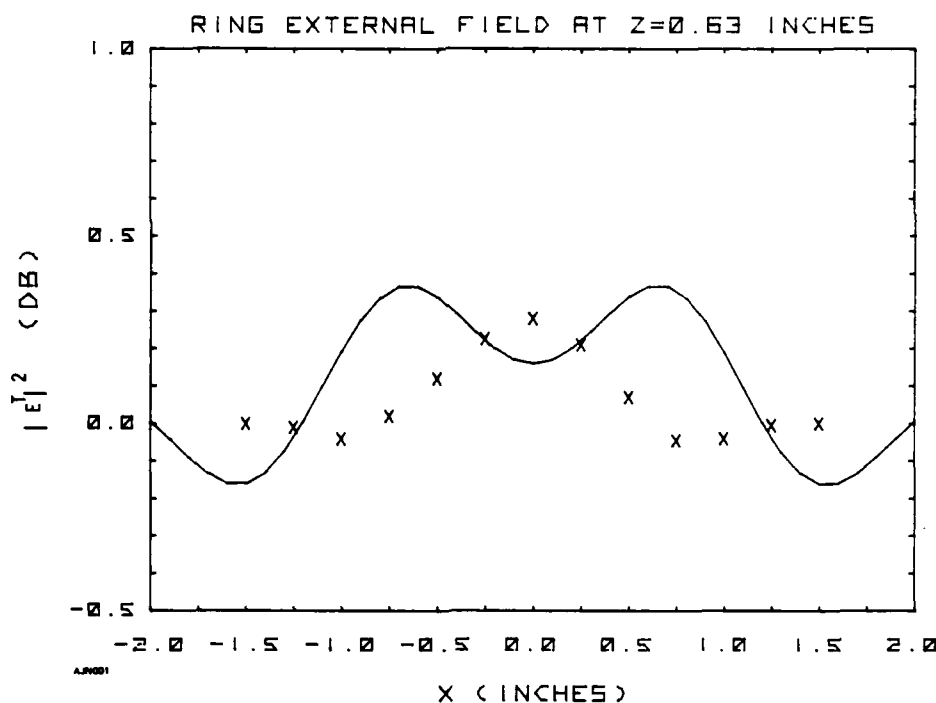


Figure 3-6. Total Field Intensity for a Ring; $z = 0.5\lambda$; $2\delta\rho = 0.625"$, $2\delta z = 0.21"$, $\rho = 0.594"$; $\kappa = 2.6$. (-): Computed; (X): Measured

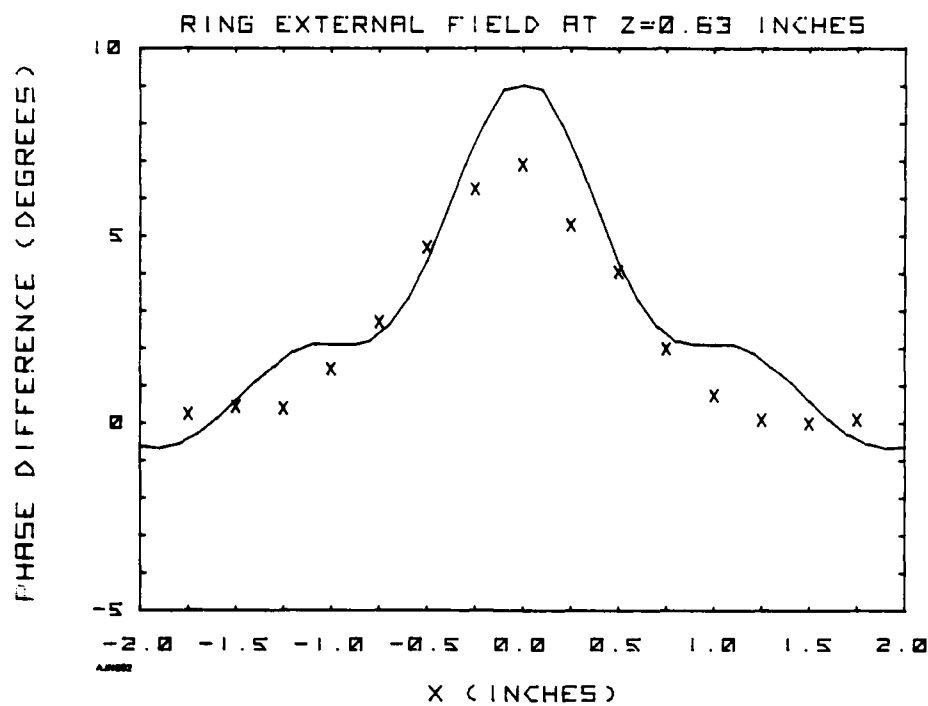


Figure 3-7. Total Field Phase for a Ring like that in Figure 3-6.

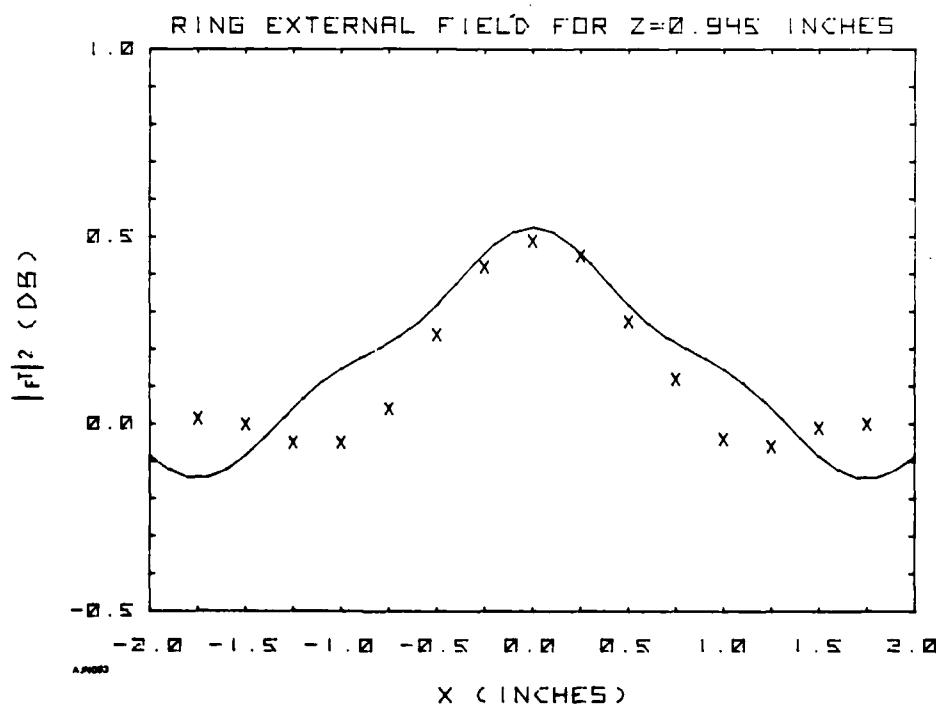


Figure 3-8. As in Figure 3-6 but $z = 0.75\lambda$

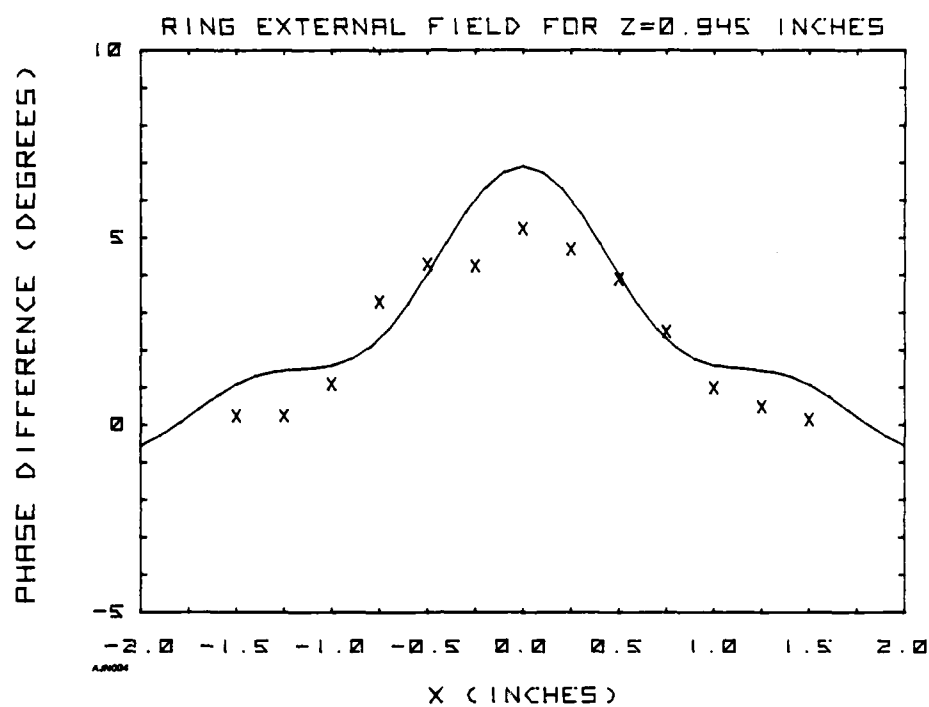


Figure 3-9. As in Figure 3-7 but $z = 0.75\lambda$

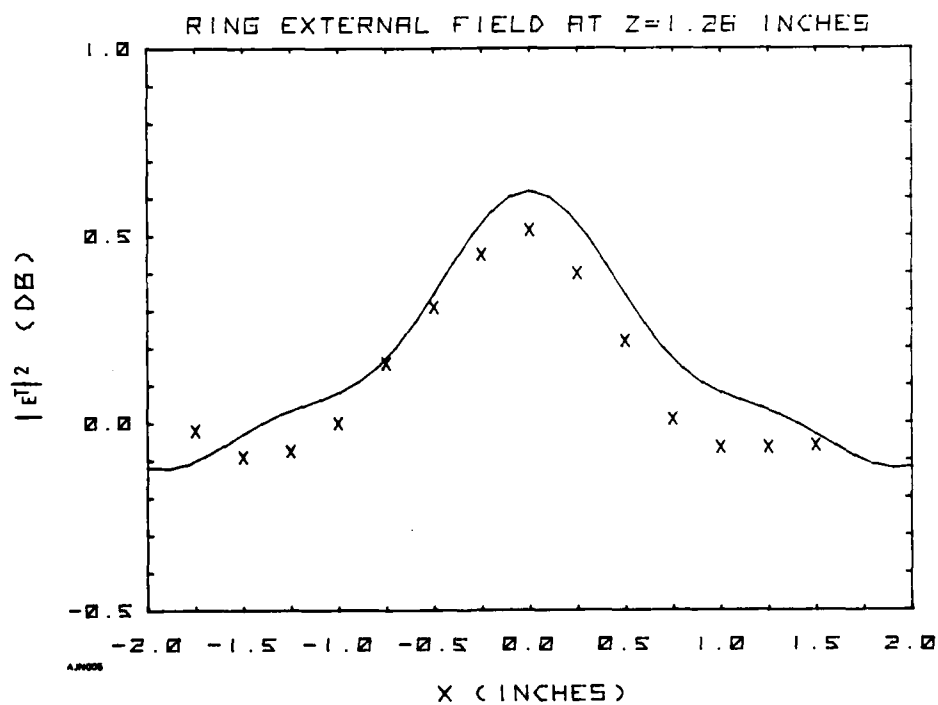


Figure 3-10. As in Figure 3-6, but $z = \lambda$

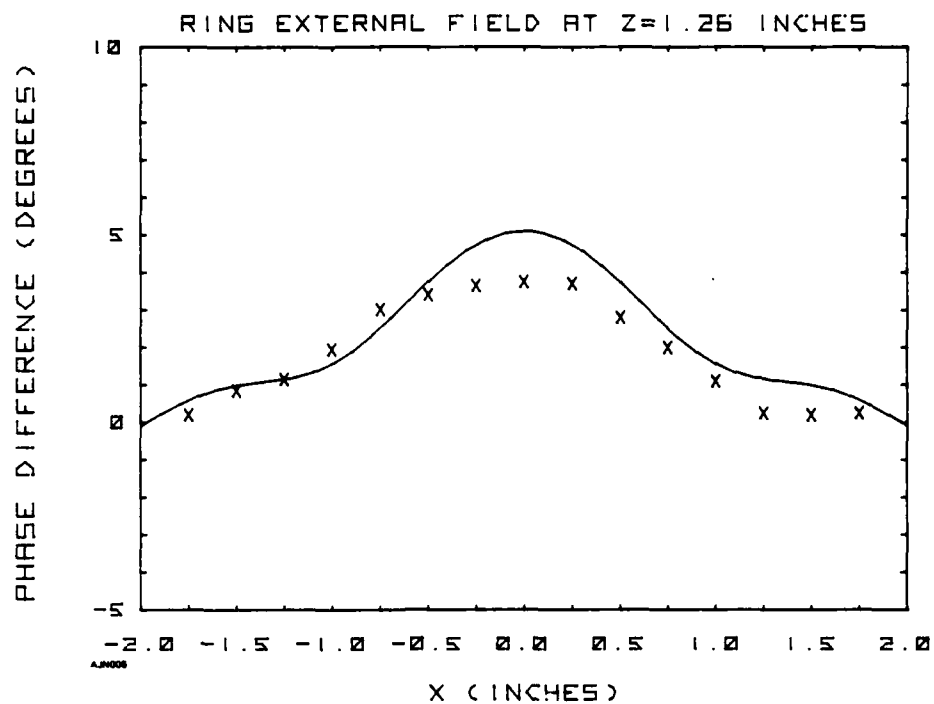


Figure 3-11. As in Figure 3-7 but $z = \lambda$.

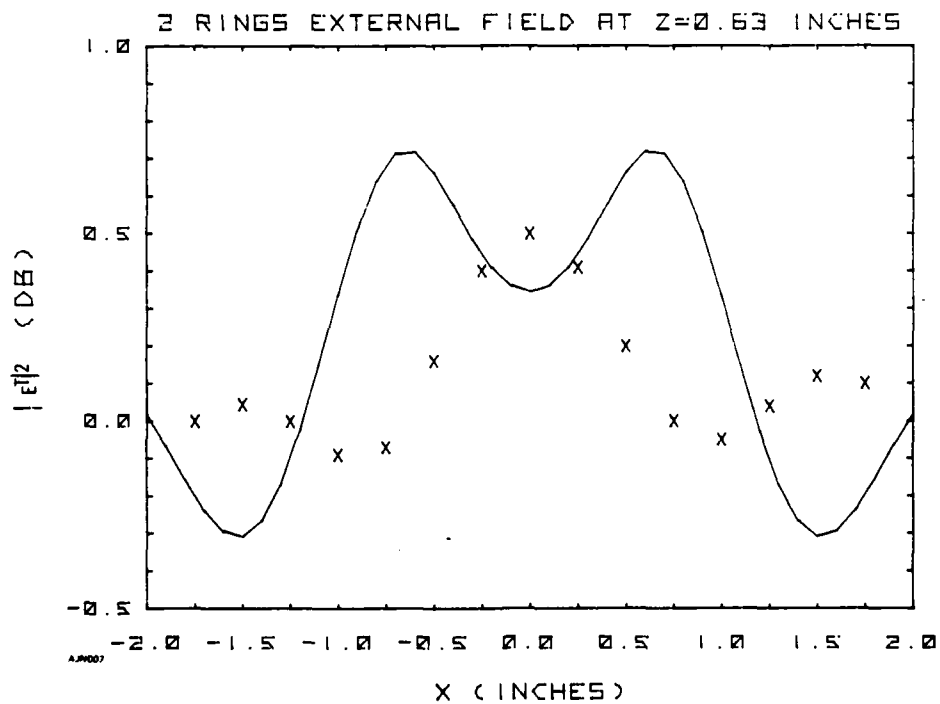


Figure 3-12. Total Field Phase for a Cylinder Composed of Two Rings; Length 0.42". (-): Computed; (X): Measured.

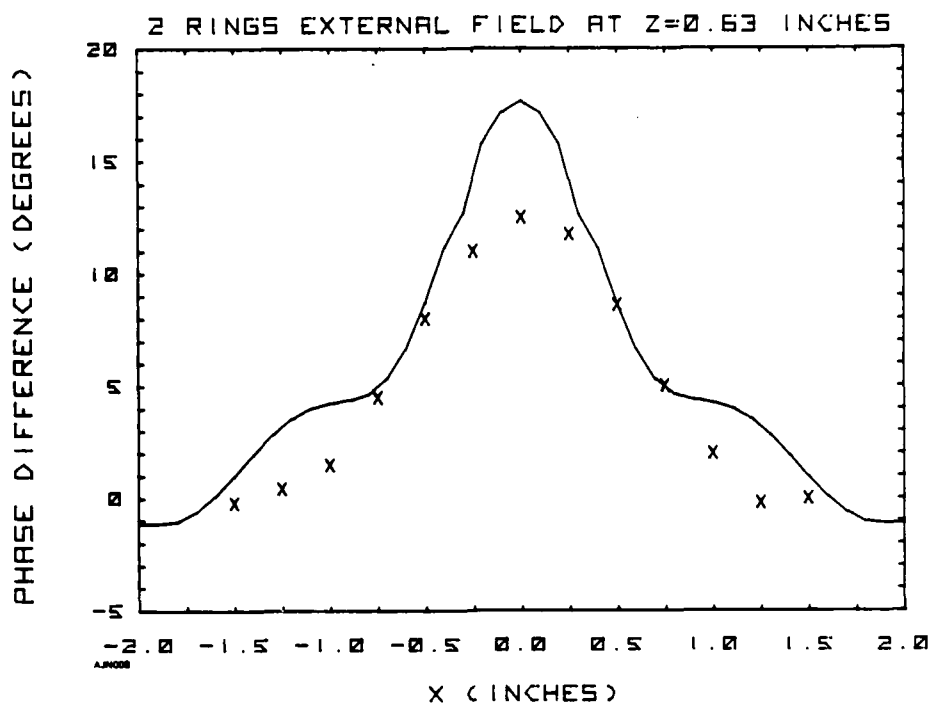


Figure 3-13. Total Field Intensity for a Cylinder Composed of Two Rings;
 $2\delta z = 0.21''$; $2\delta\rho = 0.0625$; $P = 0.594''$; $\kappa = 2.6$. (-): Computed; (X): Measured.

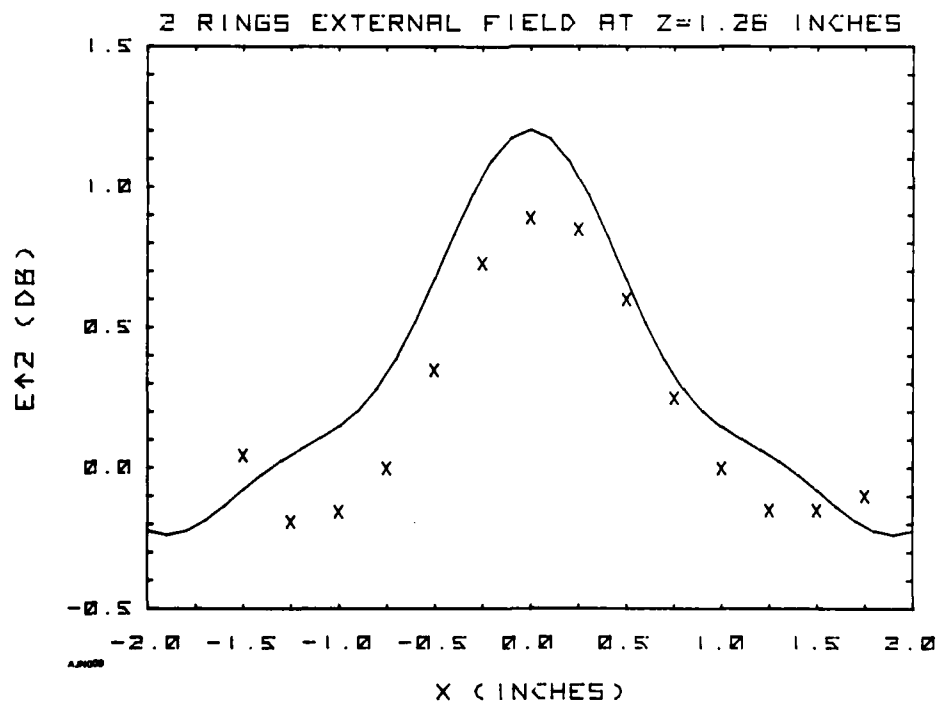


Figure 3-14. As in 3-12, but $z = \lambda$.

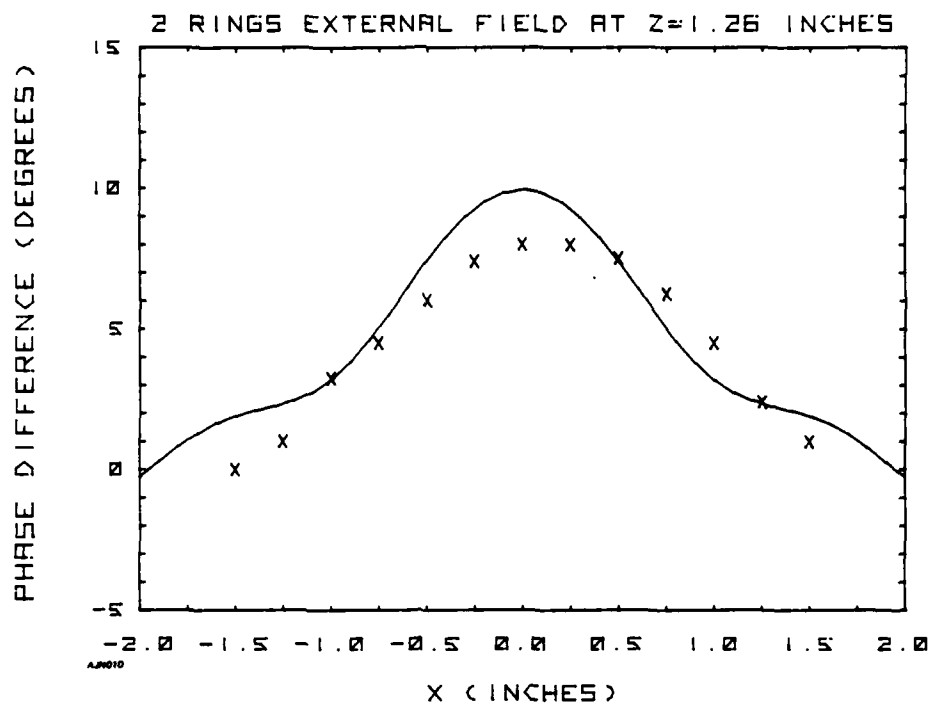


Figure 3-15. As in Figure 3-13, but $z = \lambda$.

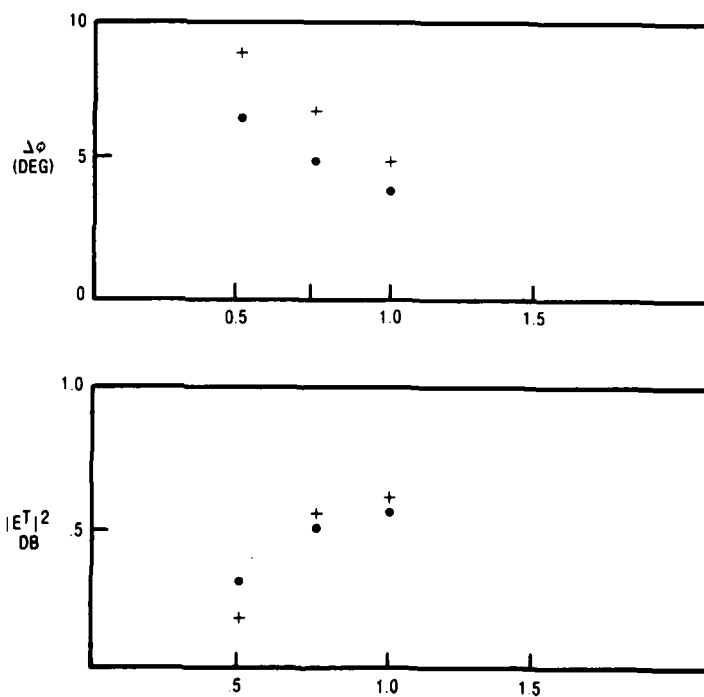


Figure 3-16. Total Field Behind Dielectric Ring with Dimensions Given in Figure 3-6. Measured (•); Computed with Equation 2-107(+).

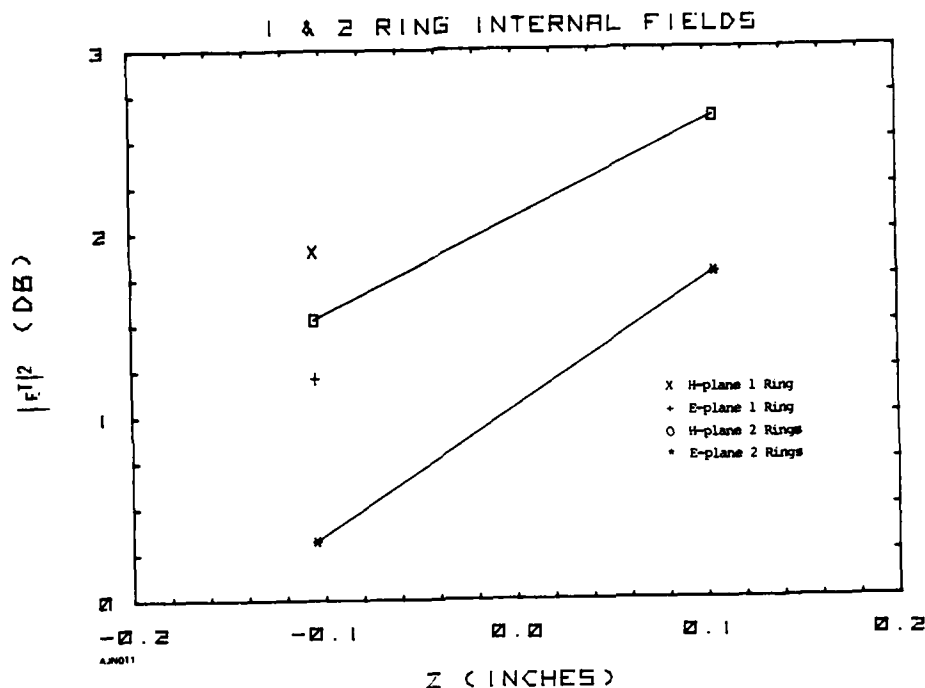


Figure 3-17. Computed Internal Values of $|E^T|^2$ for 1 and 2 Rings. $2\delta\rho = 0.0625''$, $2\delta z = 0.21''$, $\rho = 0.594''$; $N = 64$ Per Ring.

3.2 CONE

Calculations were done for the cone in Figure 2-4; dimensions are given in Figure 2-5. Incidence was axial; frequency was 9.400 GHz; polarization was horizontal (parallel to the x-axis of Figure 2-3, with the cone axis parallel to the z-axis. The cone had 13 rings although the cone in Figure 2-4 has 15.

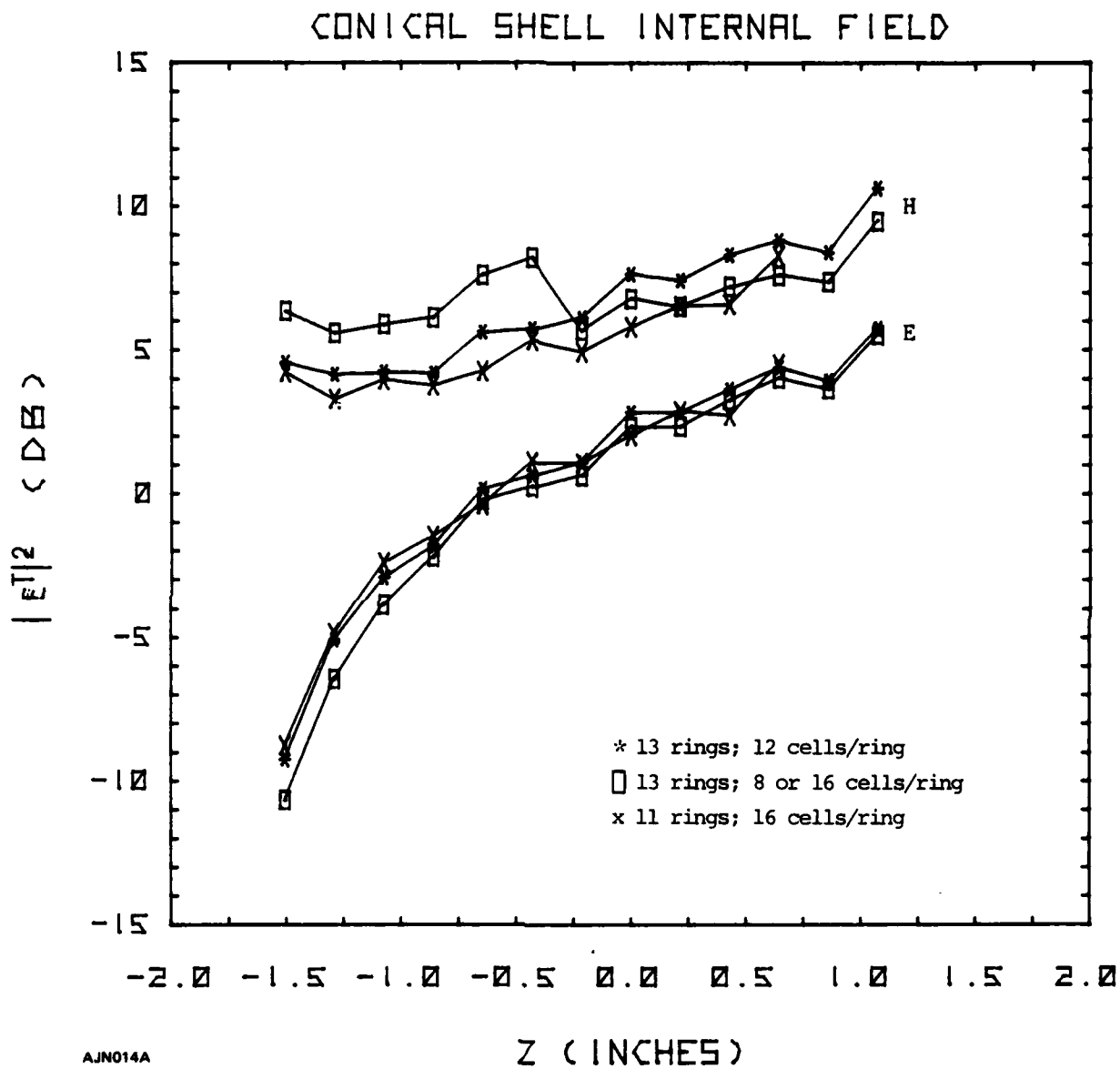
Calculations were first done for 11 rings as well as 13, with the subdivision given in Table 3-1, and for thickness of all rings $2\delta\rho = 0.63''$.

Computed values of total field intensity within the cone are shown in Figure 3-18.

The computed data in Figure 3-18 are for two generators. One is the E-plane; the other the H-plane. The polarization dependence is large, especially near the tip. The nature

Table 3-1. Computational Parameters

NUMBER OF RINGS	CELLS PER RING
13	12
13	8 in smaller 6 rings, 16 in larger 7 rings
11	16



AJN014A

Figure 3-18. Computed $|E^T|^2$ inside conical shell. The inset shows the loci of points. E refers to points in the x - z plane, the E-plane; H refers to y - z plane, the H-plane.

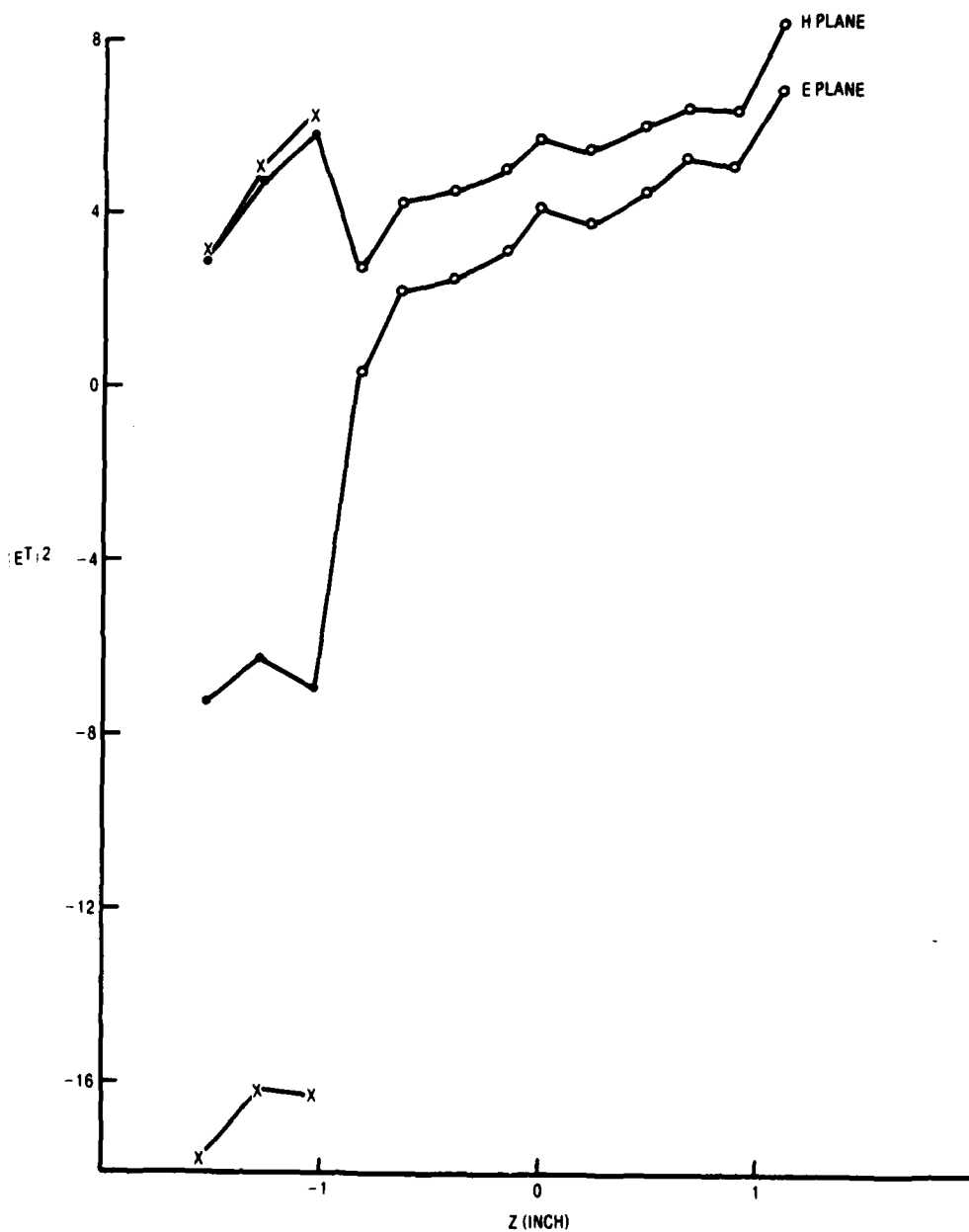
of the dependence resembles that in Figure 3-17 for two rings of equal radii. The curves in Figure 3-18 show that the numerical representation influences $|E^T|^2$. However, these differences are smaller than those between the curves for the E and H planes. Near the tip, in the region $z < -1$, the intensity is -10 dB below the incident intensity, but the H-plane intensity is 4 dB to 5 dB above the incident. Near the base the intensity exceeds the incident for both planes.

The H-plane curve for 8 cells in the smaller rings differs from the curves for the larger number of cells per ring.

The fact that $|E^T|^2$ is greater in the H-plane than the E-plane is reasonable because the electric field is approximately parallel to a cell in the H-plane but approximately orthogonal to a cell in the E-plane. However the large dependence on polarization is smaller for a single ring.

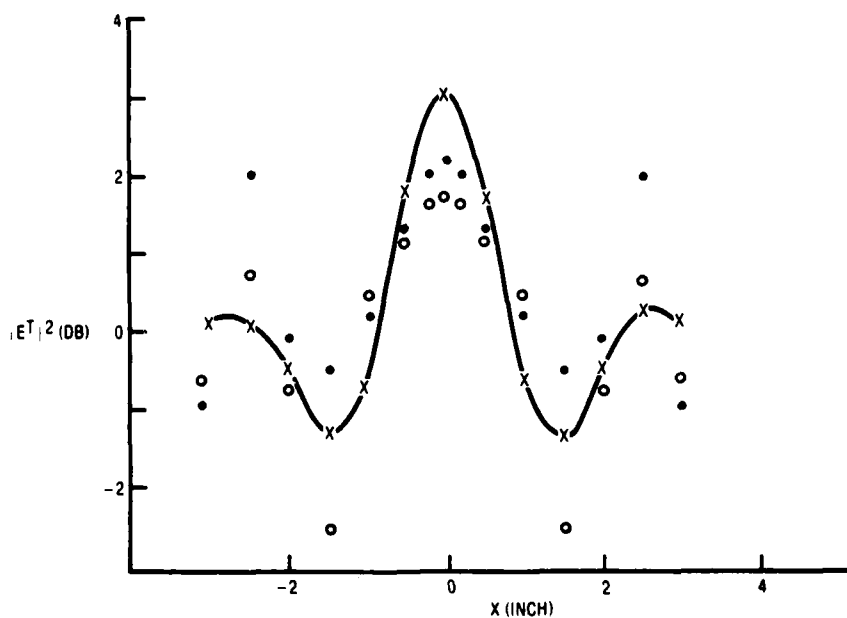
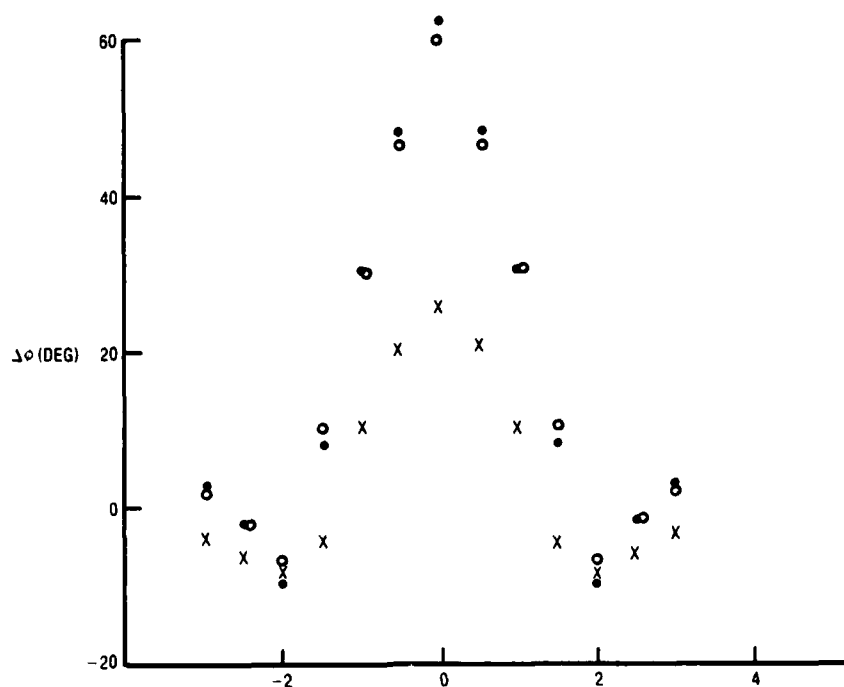
The smallest rings have thickness approximately that of the radii, violating an assumption. Therefore calculations were made by representing each of the three smallest rings by a pair of concentric rings. Figure 3-19 shows the computed internal field intensity $|E^T|^2$. The values for the E-plane depend on radial position, but those for H-plane depend negligibly on radial position. The results in Figure 3-19 also differ from those in Figure 3-18 near the base.

The external field was computed for a transverse path at $z = 1.812''$, which is a half wavelength behind the base of the cone. Figure 3-20 shows the results. The subdivision of the three rings nearest the tip influences the field.



AJN034

Figure 3-19. Computed Internal Field Intensity for Another Subdivision of Three Smallest Rings



AJN035

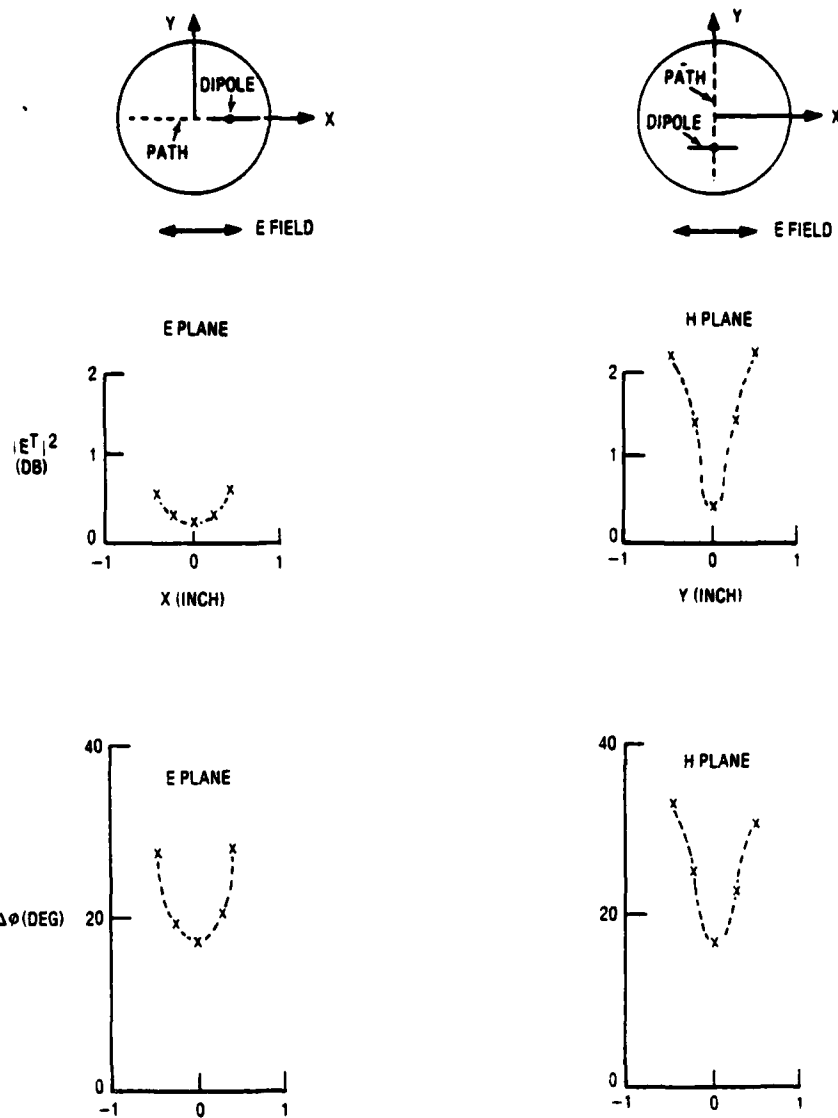
Figure 3-20. $|E^T|^2$ at Z One-Half Wavelength Behind Largest Ring ($z = 1.812''$). Measured (X); Computed (•) for 13 Rings, 12 Cells/Ring $\delta\rho = .065''$; Computed with 16 Rings, Smallest Rings Have $\delta\rho = .033''$ (•).

4. MEASUREMENT

Intensity and phase near the cylinders and cone were measured with a setup that included a half-wave dipole and a network analyzer. Measurements were made for horizontal polarization in the system of Figure 2-1. The probe was scanned in the x direction or y direction for fixed values of z.

For the cylinders Figures 3-3 through 3-6 show two observed values on the z axis; one value comes from each scan. Figures 3-6 through 3-15 show the data on transverse scans.

For the cone, Figure 3-20 shows measured values of phase and intensity for $z = 1.816''$ as a function of x. This scan is half a wavelength behind that base of the cone. Figure 4-1 shows intensity on two orthogonal scans at the center of the second largest ring.



AJN032A

Figure 4-1. Phase and Intensity Measured in Plane of 12th Ring, $z = 0.86''$ for 13-ring cone. The electric field was orthogonal to the y-z plane of Figure 1. The H plane is the y-z plane ($x = 0$) and the E plane is orthogonal to the H plane (that is, $y = 0$). The probe was a half-wave dipole.

5. DISCUSSION

5.1 CYLINDERS

Figure 3-1 suggests that convergence is obtained for a single ring divided into twenty-four cells, but Figure 3-2 suggests that two contiguous rings may require a somewhat larger number of cells per ring. The phase in the H-plane generator is the most sensitive quantity.

The axial dependence in Figure 3-3 shows the phase of the external field is somewhat overestimated. Discrepancies are 28 percent at the closest spacing of probe and ring but are a few percent at wavelength spacing. Probe correction, in the theory, reduces discrepancies. Figure 3-5 shows that a reduction of $\delta\rho$ by 20 percent reduced discrepancies to small values, comparable to the measurement precision. The reduction of $\delta\rho$ is possibly related to the approximation made in evaluating the integral in Paragraph 2.3.1, specifically to the integral over θ .

The axial dependence in Figure 3-16 is comparable to that in Figure 3-3 despite the approximation of using circumferentially independent fields for the results shown in Figure 3-3.

The transverse dependence in Figure 3-6 shows discrepancies of five percent in $|E^T|$ at off-axis positions of approximately one inch. In general, phase discrepancies are approximately 20 percent for small probe-ring separation. The shape of the measured and computed curves agree well.

5.2 CONE

Figure 3-18 shows a polarization dependence of the internal field $|E^T|$. The approximation that required ring radius to be much larger than thickness was tested. Figures 3-18 and 3-19 show that this approximation produces significant internal field changes.

The measured data in Figure 4-1 show a polarization dependence. The H-plane intensity exceeds the E-plane intensity by approximately 1-1/2 dB. This difference is approximately that for the internal fields of the larger rings; see Figure 3-19. Figure 3-20 shows that discrepancies are reduced by performing calculations with smaller ring thicknesses, for the rings near the tip of the cone. The differences between measured and computed phase are large for the probe on the axis, but fall to smaller values at the first minimum. The shape of the measured and computed curves agree, especially for the graph computed with small values of $\delta\rho$ near the tip. It is unclear whether the discrepancies are caused by numerical or theoretical approximations.

6. TENSOR GREEN'S FUNCTION FORMULATION

6.1 INTEGRAL EQUATION

Maxwell's equations for time harmonic electric and magnetic fields of angular frequency ω in the presence of a nonmagnetic scatterer of dielectric function $\kappa(\mathbf{r})$ can be combined to yield a wave equation for the electric field $\underline{\underline{E}}(\mathbf{r})$:

$$\nabla \times \nabla \times \underline{\underline{E}} - k^2 \underline{\underline{E}} = k^2 (\kappa - 1) \underline{\underline{E}} \quad (6-1)$$

Here $k = 2\pi/\lambda_0 = \omega/c$ is the free space wavenumber, λ_0 the free space wavelength, and c the speed of light in vacuum. The tensor (or dyadic) Green's function¹¹ $\underline{\underline{\Gamma}}$:

$$\underline{\underline{\Gamma}}(\mathbf{k}, \mathbf{r}', \mathbf{r}) = (\underline{\underline{1}} + k^{-2} \nabla' \nabla') (\exp(i\mathbf{k} \cdot (\mathbf{r}' - \mathbf{r})) (4\pi |\mathbf{r}' - \mathbf{r}|)^{-1}) \quad (6-2)$$

satisfying

$$\begin{aligned} \nabla \times \nabla \times \underline{\underline{\Gamma}} - k^2 \underline{\underline{\Gamma}} &= \underline{\underline{1}} \delta^3(\mathbf{r} - \mathbf{r}') \\ \nabla \cdot \underline{\underline{\Gamma}} &= 0 \quad (\mathbf{r} \neq \mathbf{r}') \end{aligned}$$

(where $\delta^3(\mathbf{r} - \mathbf{r}')$ is the three-dimensional Dirac delta function) can be used to immediately rewrite (6-1) as an integral equation:

$$\underline{\underline{E}}(\mathbf{k}, \mathbf{r}') - \underline{\underline{E}}^I(\mathbf{k}, \mathbf{r}') + k^2 \int_{V_s} dV \underline{\underline{\Gamma}}(\mathbf{k}, \mathbf{r}', \mathbf{r}) \underline{\underline{E}}(\mathbf{k}, \mathbf{r}) [\kappa(\mathbf{r}) - 1] \quad (6-3)$$

Here $\underline{\underline{E}}^I$ is the incident electric field satisfying the homogeneous free space equation

$$\nabla \times \nabla \times \underline{\underline{E}}^I - k^2 \underline{\underline{E}}^I = 0$$

and the integration extends over the volume V_s of the scatterer (everywhere $\kappa(\mathbf{r}) \neq 1$).

To begin the transition to the moment method approximation of (6-3), we partition V_s into η subvolumes ("cells") each of volume V_n ; moreover, we assume $\kappa(\mathbf{r}) = \kappa = \text{constant}$ inside the scatterer. Then (6-3) becomes:

$$\begin{aligned} \underline{\underline{E}}(\mathbf{k}, \mathbf{r}) &= \underline{\underline{E}}^I(\mathbf{k}, \mathbf{r}') + k^2 (\kappa - 1) \sum_{n \neq n_{r'}} \int_{V_n} dV \underline{\underline{\Gamma}}(\mathbf{k}, \mathbf{r}', \mathbf{r}) \cdot \underline{\underline{E}}(\mathbf{k}, \mathbf{r}) \\ &\quad + k^2 (\kappa - 1) \int_{V_{n_{r'}}} dV \underline{\underline{\Gamma}}(\mathbf{k}, \mathbf{r}', \mathbf{r}) \underline{\underline{E}}(\mathbf{k}, \mathbf{r}) \end{aligned} \quad (6-4)$$

where $V_{n,r'}$ is the volume of the cell containing the observation point r' . If r' is outside the scatterer, the last integral in (6-4) is absent.

Now we introduce the essential assumption underlying the moment method: the n th cell is assumed to be small enough that the electric field $E(r)$ may be approximated as a constant E_n throughout the cell. As a consequence $E(r)$ may be removed from the integral in (6-4):

$$E(k, r') \approx E^I(k, r') + k^2 (\kappa - 1) \sum_{n \neq n_{r'}} E_n \cdot \int_{V_n} dV \underline{\underline{I}}(k, r', r) \\ + k^2 (\kappa - 1) E_n \cdot \int_{V_{n_{r'}}} dV (k, r', r) \quad (6-5)$$

The major remaining task is the evaluation of the two integrals appearing in (6-5):

$$\underline{\underline{I}}(k, r', r) \equiv \int_{V_n} dV \underline{\underline{I}}(k, r', r) \quad (6-6)$$

Substituting (6-2) for $\underline{\underline{I}}$ into (6-6):

$$\underline{\underline{I}}(k, r', r) = (4\pi)^{-1} \int_{V_n} dV (1 + k^{-2} \nabla' \nabla') g(k, r', r) \quad (6-7)$$

where $g(k, r', r) = (|r' - r|)^{-1} \exp(ik|r' - r|)$ is the scalar Green's function. To actually perform the integration (6-7) we approximate the n th cell as a sphere of radius a centered at r_n . If we temporarily exclude the case $n = n_{r'}$, so that the observation point r' is not within the cell, we may remove the gradient operators from the integral:

$$\underline{\underline{I}}(k, r', n) = (4\pi)^{-1} (1 + k^{-2} \nabla' \nabla') \int_{V_n} dV g(k, r', r)$$

The integration over the spherical volume is conveniently carried out by Fourier decomposing g ; the result is

$$\underline{\underline{I}}(k, r', r) = k^{-3} (\sin ka - k \cos ka) (1 + k^{-2} \nabla' \nabla') g(k, r', r_n) (|r' - r_n| \geq a) \quad (6-8)$$

When $n = n_{r'}$, the source point r and observation point r' coincide in the integration volume $V_{n_{r'}}$ and the integrand in (6-7) is formally divergent. However, a principal value prescription¹² may be applied to give (6-7) a unique value in this case:

$$\underline{\underline{I}}(k, r', n_{r'}) = -k^{-2} \left[\frac{2}{3} (ika - 1) \exp(ika) + 1 \right] \underline{\underline{1}} \quad (6-9)$$

In view of (6-6), (6-8), and (6-9), equation (6-5) becomes:

$$\begin{aligned} \underline{\underline{E}}(k, r') &\approx \underline{\underline{E}}^I(k, r) + (\kappa - 1) k^{-1} (\sin ka - \kappa \cos ka) \\ &\times \sum_{n \neq n_{r'}} \underline{\underline{E}}_n \cdot \left(\underline{\underline{1}} + k^{-2} \nabla' \nabla' \right) g(k, r', r_n) \\ &+ (1 - \kappa) \left[\frac{2}{3} (ika - 1) \exp(ika) + 1 \right] \underline{\underline{E}}_n \end{aligned} \quad (6-10)$$

The last term is absent if r' is outside the scatterer. Rearrangement of (6-10) yields

$$\begin{aligned} \underline{\underline{E}}(k, r') &\approx \left[\frac{2}{3} (\kappa - 1) (ika - 1) \exp(ika) + \kappa \right]^{-1} \underline{\underline{E}}^I(k, r') \\ &+ (\kappa - 1) k^{-1} (\sin ka - \kappa \cos ka) \left[\frac{2}{3} (\kappa - 1) (ika - 1) \exp(ika) + \kappa \right]^{-1} \\ &\times \sum_{n \neq n_r} \underline{\underline{E}}_n \cdot \left(\underline{\underline{1}} + k^{-2} \nabla' \nabla' \right) g(k, r', r_n) \end{aligned} \quad (6-11)$$

(valid for r' within the scatterer)

$$\begin{aligned} \underline{\underline{E}}(k, r') &\approx \underline{\underline{E}}^I(k, r') + (\kappa - 1) k^{-1} (\sin ka - \kappa \cos ka) \\ &\times \sum_n \underline{\underline{E}}_n \cdot \left(\underline{\underline{1}} + k^{-2} \nabla' \nabla' \right) g(k, r', r_n) \end{aligned} \quad (6-12)$$

(valid for r' external to the scatterer)

From (6-11) we obtain for the field in the mth cell in the scatter:

$$\underline{E}_m \approx \left[\frac{2}{3} (\kappa-1) (ika - 1) \exp(ika) + \kappa \right]^{-1} \left\{ \underline{E}_m^I + (\kappa-1) k^{-1} (\sin ka - k a \cos ka) \right. \\ \left. \left[\frac{2}{3} (\kappa-1) (ika - 1) \exp(ika) + \kappa \right]^{-1} \times \sum_{n \neq m} \underline{E}_n \cdot (1 + k^{-2} \nabla_m \nabla_m) g(k, R_{mn}) \right\} \quad (6-13)$$

where

$$g(k, R_{mn}) \equiv R_{mn}^{-1} \exp(ik R_{mn})$$

and

$$R_{mn} \equiv |\underline{R}_{mn}| \equiv |\underline{r}_m - \underline{r}_n|$$

Since

$$k^{-2} \nabla_m \nabla_m g(k, R_{mn}) = g(k, R_{mn}) \left\{ k^{-2} R_{mn}^{-4} \left[3(1 - ikR_{mn}) - k^2 R_{mn}^2 \right] R_{mn} R_{mn} \right. \\ \left. + (kR_{mn})^{-2} (ikR_{mn} - 1) \underline{1} \right\} (R_{mn} \neq 0)$$

Equation (6-13) becomes

$$\underline{E}_m \approx \left[\frac{2}{3} (\kappa-1) (ika - 1) \exp(ika) + \kappa \right]^{-1} \underline{E}_m^I \\ + (\kappa-1) k^{-3} (\sin ka - k a \cos ka) \left[\frac{2}{3} (\kappa-1) (ika - 1) \exp(ika) + \kappa \right]^{-1} \\ \times \sum_{n \neq m} g(k, R_{mn}) \left\{ R_{mn}^{-2} \left[k^2 R_{mn}^2 + ikR_{mn} - 1 \right] \underline{E}_n \right. \\ \left. + R_{mn}^{-4} \left[3(1 - ikR_{mn}) - k^2 R_{mn}^2 \right] (\underline{R}_{mn} \cdot \underline{E}_n) \underline{R}_{mn} \right\} \quad (6-14)$$

Equation (6-14) is our main result. Note that for $ka \ll 1$:

$$\frac{2}{3} (\kappa-1) (ika - 1) \exp(ika) + \kappa \approx (\kappa+2)/3$$

$$k^{-3} (\sin ka - ka \cos ka) \approx a^3/3$$

so that in this limit (6-14) is:

$$\begin{aligned} \underline{E}_m &\approx 3 (\kappa+2)^{-1} \underline{E}_m^I + (\kappa+2)^{-1} (\kappa-1) a^3 \\ &\times \sum_{n \neq m} g(k, R_{mn}) \left\{ R_{mn}^{-2} \left[k^2 R_{mn}^2 + ik R_{mn}^{-1} \right] \underline{E}_n \right. \\ &\left. + R_{mn}^{-4} \left[3 (1 - ik R_{mn}) - k^2 R_{mn}^2 \right] (\underline{R}_{mn} \cdot \underline{E}_n) \underline{R}_{mn} \right\} (ka \ll 1) \end{aligned} \quad (6-15)$$

Now consider a collection of oscillating electric dipoles. The electric field at \underline{r} due to one such dipole is¹¹:

$$\begin{aligned} \underline{E}^{\text{Dipole}} &= k^2 \left\{ [(\underline{r}/r) \times \underline{P}] \times (\underline{r}/r) \right\} g(k, r) \\ &+ \left\{ 3 (\underline{r}/r) [(\underline{r}/r) \cdot \underline{P}] - \underline{P} \right\} (r^{-2} - ikr^{-1}) g(k, r) \\ &= g(k, r) \left\{ r^{-2} \left[k^2 r^2 + ikr - 1 \right] \underline{P} + r^{-4} \left[3 (1 - ikr) - k^2 r^2 \right] (\underline{r} \cdot \underline{P}) \underline{r} \right\} \end{aligned}$$

where \underline{P} is the dipole moment. If the dipole moment is induced by an electric field $\underline{E}^{\text{internal}}$, we have

$$\underline{P} = \gamma \underline{E}^{\text{internal}}$$

where γ is the "molecular" polarizability (i.e., the polarizability of the dipole when immersed in the collection of all the other dipoles). By the Claussius-Mossotti equation¹⁴:

$$\gamma = (4 \pi N)^{-1} 3 (\kappa-1) (\kappa+2)^{-1}$$

where N is the number of dipoles per unit volume. Assuming each dipole occupies a sphere of radius a ,

$$N = (4 \pi a^3/3)^{-1}$$

implying

$$\gamma = (\kappa-2)^{-1} (\kappa+1) a^3$$

Therefore,

$$\begin{aligned} \underline{E}^{\text{Dipole}} = (\kappa+2)^{-1} (\kappa-1) a^3 g(k, r) \left\{ r^{-2} \left[k^2 r^2 + ikr - 1 \right] \underline{E}^{\text{internal}} \right. \\ \left. + r^{-4} \left[3(1 - ikr) - k^2 r^2 \right] \underline{E}^{\text{internal}} \right\} \end{aligned} \quad (6-16)$$

Further, if \underline{E}^I is the incident field in free space, then the internal field $\underline{E}^{\text{I internal}}$ in any dielectric sphere due to \underline{E}^I is¹⁵:

$$\underline{E}^{\text{I internal}} = 3 (\kappa+2)^{-1} \underline{E}^I \quad (6-17)$$

Comparing (6-16) and (6-17) to (6-15), we observe that for $ka \ll 1$, the moment approximation consists of replacing a dielectric scatterer by a collection of interacting electric dipoles each occupying a spherical volume $4\pi a^3/3$ and whose induced dipole moments obey the Clausius-Mossotti equation. This result is the same as that of Purcell and Pennypacker¹⁶ (with the exception of the incident field term, where they assume $\underline{E}^{\text{I internal}} = \underline{E}^I$), and so constitutes an independent verification of our main result (6-14) in the long wavelength limit.

6.2 COMPUTATIONAL TECHNIQUE

Eq. 6-14 may be written more compactly as

$$\underline{E}_m = \delta^{-1} \underline{E}_m^I + \delta^{-1} \alpha \sum_{n \neq m} \left\{ \beta_{mn} \underline{E}_n + \underline{\gamma}_{mn} \cdot \underline{E}_n \right\} \quad (6-18)$$

where

$$\alpha \equiv (\kappa-1) k^{-3} (\sin ka - ka \cos ka)$$

$$\beta_{mn} \equiv g(k, R_{mn}) R_{mn}^{-2} \left[k^2 R_{mn}^2 + i k R_{mn} - 1 \right]$$

$$\underline{\gamma}_{mn} \equiv g(k, R_{mn}) R_{mn}^{-4} \left[3(1 - i k R_{mn}) - k^2 R_{mn}^2 \right] \underline{R}_{mn} \underline{R}_{mn}$$

$$\delta \equiv \frac{2}{3} (\kappa-1) (ika - 1) \exp(ika) + \kappa$$

Note that β and γ are symmetric η by η matrices.

Introduce i, j for 3-vector indices. In component form (6-18) becomes:

$$E_{mi} = \delta^{-1} E_{mi}^I + \delta^{-1} \alpha \sum_{n \neq m} \sum_j (\beta_{mn} \delta_{ij} + \gamma_{mnij}) E_{nj} \quad (6-19)$$

By defining

$$\hat{\beta}_{mn} = \beta_{mn} (1 - \delta_{mn})$$

$$\hat{\gamma}_{mnij} = \gamma_{mnij} (1 - \delta_{mn})$$

we may formally extend the sum in (6-19) to include $n = m$:

$$E_{mi} = \delta^{-1} E_{mi}^I + \delta^{-1} \alpha \sum_n \sum_j (\hat{\beta}_{mnij} + \hat{\gamma}_{mnij}) E_{nj}$$

or:

$$E_{mi}^I = \sum_{n=1}^{\eta} \sum_{j=1}^3 \left[\delta \delta_{mn} \delta_{ij} - \alpha (\hat{\beta}_{mnij} + \hat{\gamma}_{mnij}) \right] E_{nj} \quad (6-20)$$

If we introduce "composite" indices M, N by the mapping

$$M = 3(m-1) + i \quad (1 \leq M, N \leq 3\eta)$$

$$N = 3(n-1) + j$$

Eq. (6-20) takes the form

$$\epsilon_M^I = \sum_{N=1}^{3\eta} A_{MN} \epsilon_N \quad (6-21)$$

where

$$\epsilon_M^I = \epsilon^I [3(m-1) + i] \equiv E_{mi}^I$$

$$\epsilon_N = \epsilon [3(n-1) + j] \equiv E_{nj}$$

$$A_{MN} = A [3(m-1) + i] [3(n-1) + j] \equiv \delta \delta_{MN} \delta_{ij} - \alpha (\hat{\beta}_{MNij} + \hat{\gamma}_{MNij})$$

A_{MN} is a symmetric 3η by 3η matrix.

According to (6-21), the moment method approximation has reduced the problem of finding the electric field in a dielectric scatterer to the algebraic task of solving 3η simultaneous equations for 3η complex unknowns. A variety of practical computational techniques exist for solving such a system of equations for η as large as $10^3 - 10^4$ cells.

The only remaining latitude in the approximation is the selection of a , the radius of the spherical cells, and η , the total number of such cells. Since we require that \underline{E} be almost constant in any one cell, we make this requirement quantitative by asking that the phase change in \underline{E} across any cell diameter $2a$ be less than .2 radians. Thus:

$$2a/(\lambda_o/\sqrt{\kappa}) \leq .2$$

or

$$a \leq \lambda_o/(10\sqrt{\kappa}) \quad (6-22)$$

If we further assume that the total volume of the η spherical cells equals the volume V_s of the scatterer:

$$\eta = V_s/(\frac{4}{3} \pi a^3) \geq V_s (10\sqrt{\kappa})^3/(\frac{4}{3} \pi \lambda_o^3) \quad (6-23)$$

7. RESULTS FROM THE TENSOR GREEN'S FUNCTION FORMULATION

An earlier report¹⁰ treated scattering from a dielectric rod and dielectric ring utilizing the scalar Green's function technique. In this section, we reexamine those cases using the Green's tensor formulation developed in Section 6 of this report. The measurements shown below are taken from reference 10, where they are discussed in more detail.

7.1 ROD

The first example considered was a dielectric rod ($\kappa = 2.6$) of length 1.9 inches and diameter 0.139 inches aligned lengthwise along the z-axis. Figure 7-1 shows the rod and its approximation as 15 overlapping spheres, each of radius .0765 inch. The incident wavelength was 1.259 inches and both parallel and perpendicular incident polarizations were considered. Figures 7-2 and 7-3 display the computed internal fields for the two polarizations. For comparison, note that the internal field in an infinite rod of the same diameter and dielectric constant is 1.4 dB above the incident field in the case of parallel polarization. Figures 7-4 through 7-11 exhibit the calculated and measured external fields at two different distances from the rod. With the exception of Figure 7-9, the agreement between theory and measurement is good. Since we would expect the measured phase difference to vanish as z becomes large, the discrepancy in Figure 7-9 is evidently a systematic measurement error.



AJN015

Figure 7-1. Dielectric Rod as Approximated by 15 Dielectric Spheres.
Rod Length: 1.9", Rod Diameter: 0.139"; Sphere Radii: 0.0765".

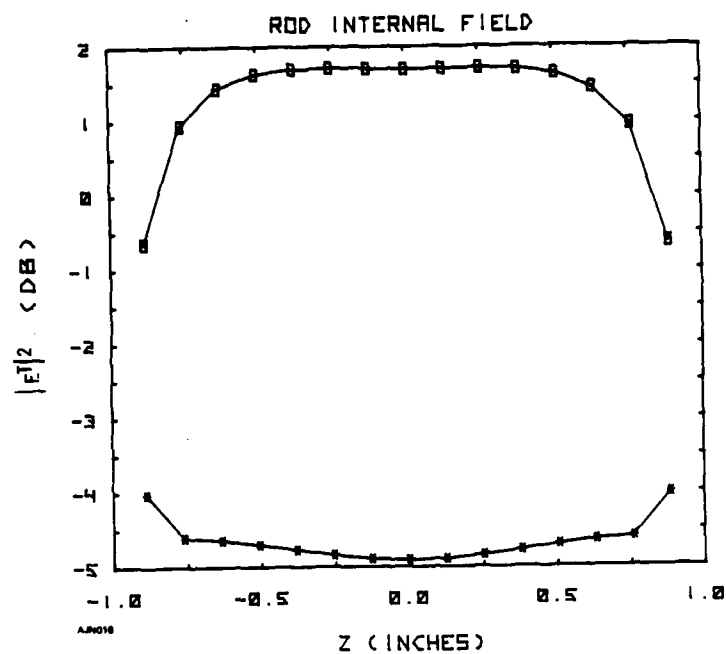


Figure 7-2. Computed Internal Field Intensity for the Dielectric Rod of Figure 7-1.
(O): E^I Parallel to Rod; (*): E^I Perpendicular to Rod.

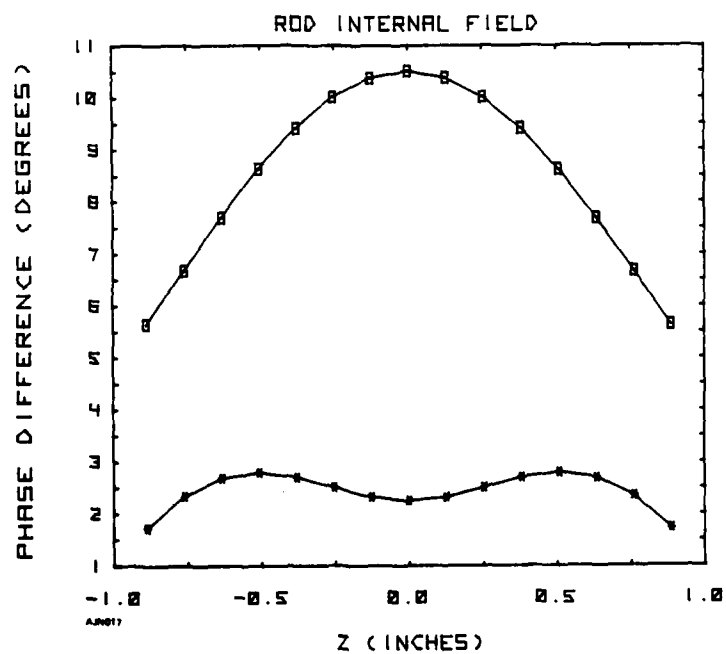


Figure 7-3. Computed Internal Field Phase for the Dielectric Rod of Figure 7-1.
(O): E^I Parallel to Rod; (*) E^I Perpendicular to Rod

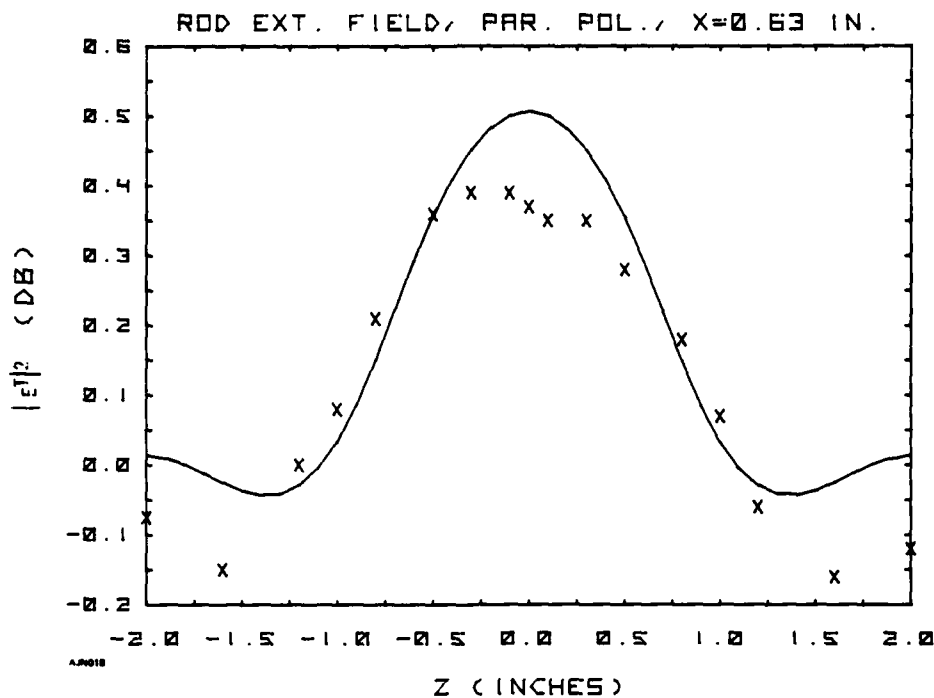


Figure 7-4. Total Field Intensity for the Dielectric Rod of Figure 7-1 for E^I Parallel to Rod and $x = .5\lambda$. (-): Computed; (X): Measured.

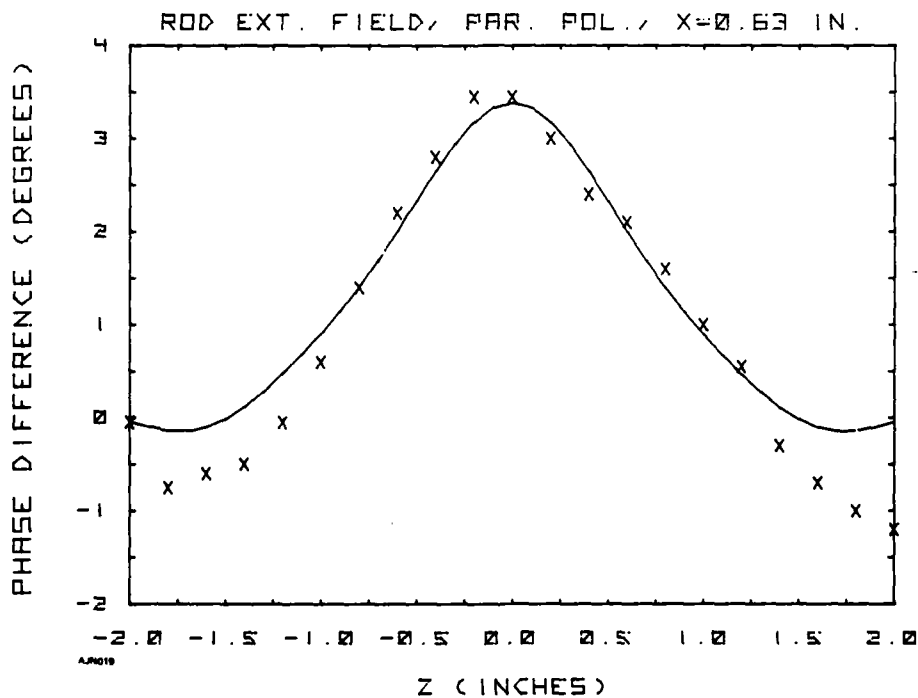


Figure 7-5. Total Field Phase for the Dielectric Rod of Figure 7-1 for E^I Parallel to Rod and $x = .5\lambda$. (-): Computed; (X): Measured.

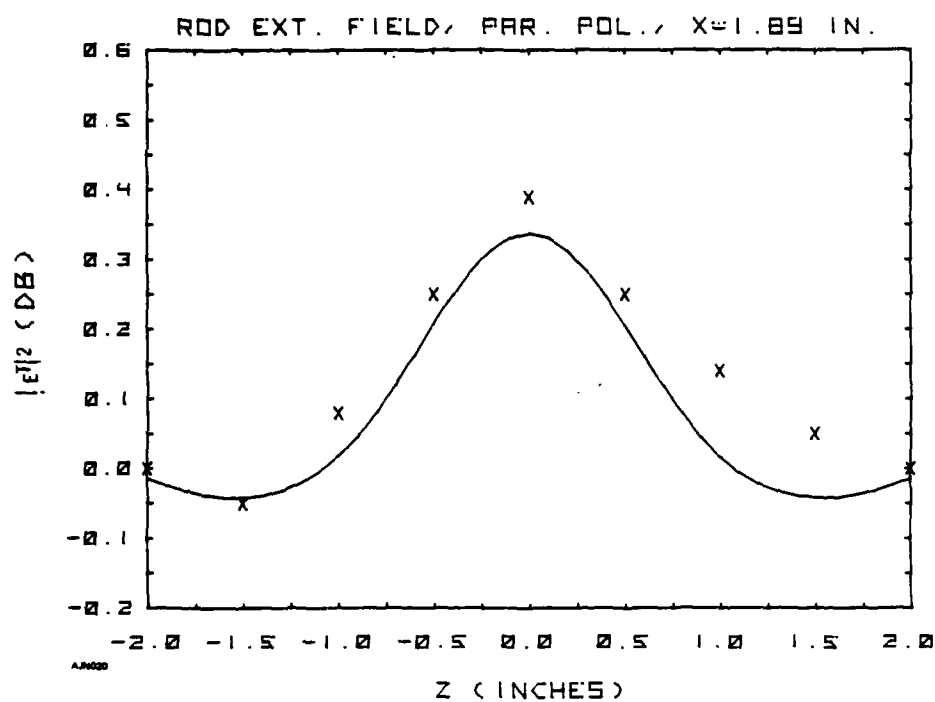


Figure 7-6. As in Figure 7-4, but $x = 1.5\lambda$.

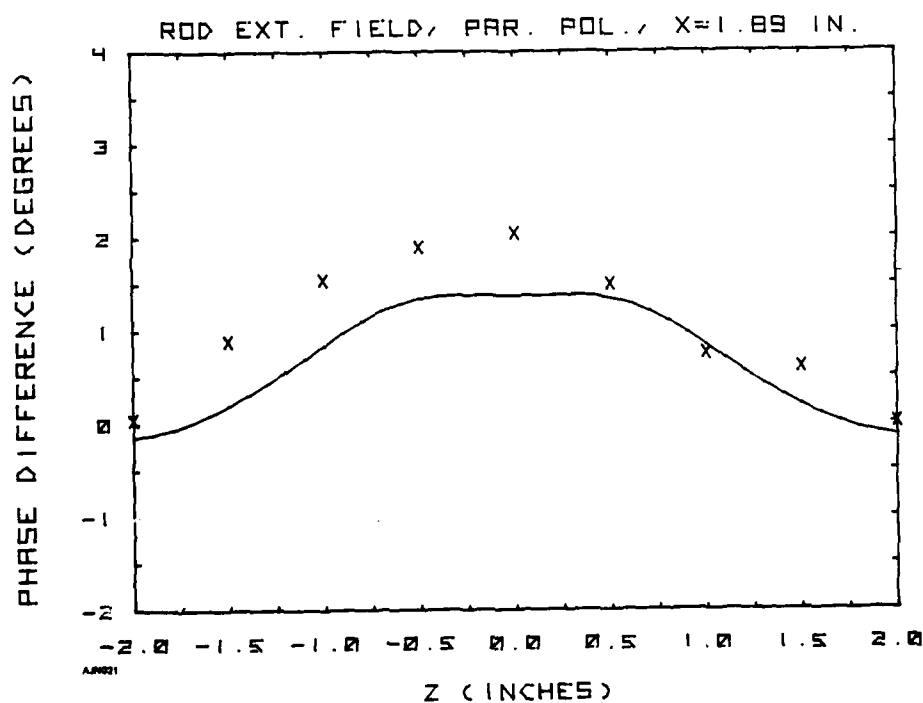


Figure 7-7. As in Figure 7-5, but $x = 1.5\lambda$.

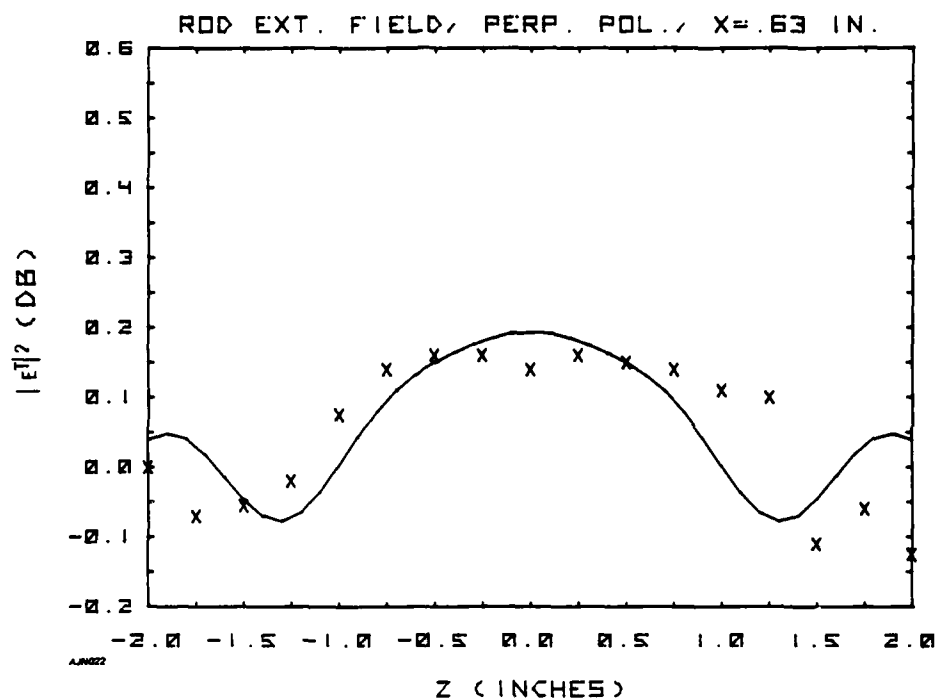


Figure 7-8. As in Figure 7-4, but E^I Perpendicular to Rod.

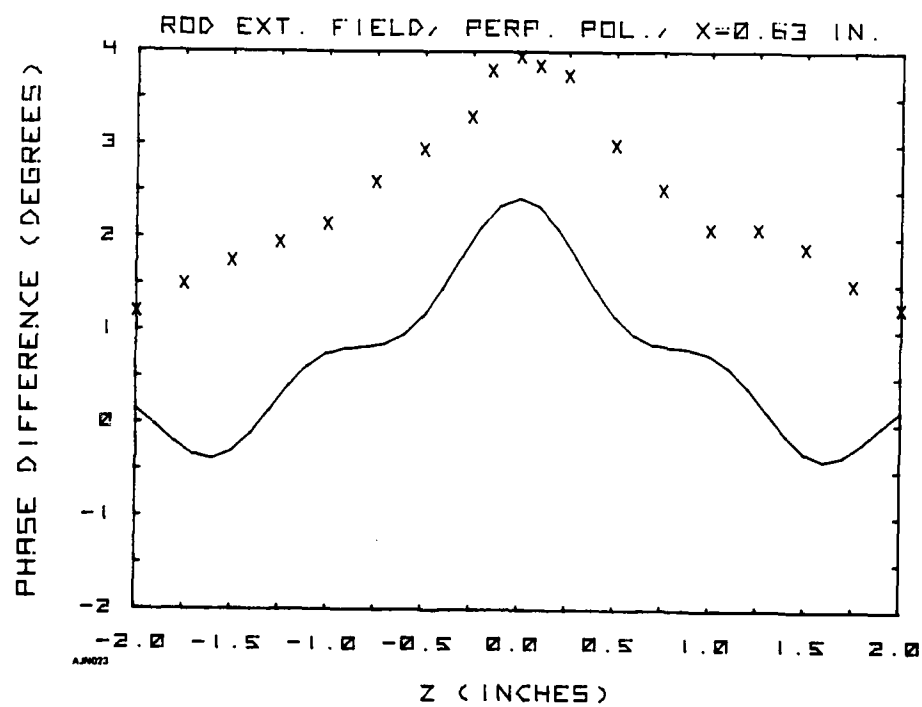


Figure 7-9. As in Figure 7-5, but E^I Perpendicular to Rod.

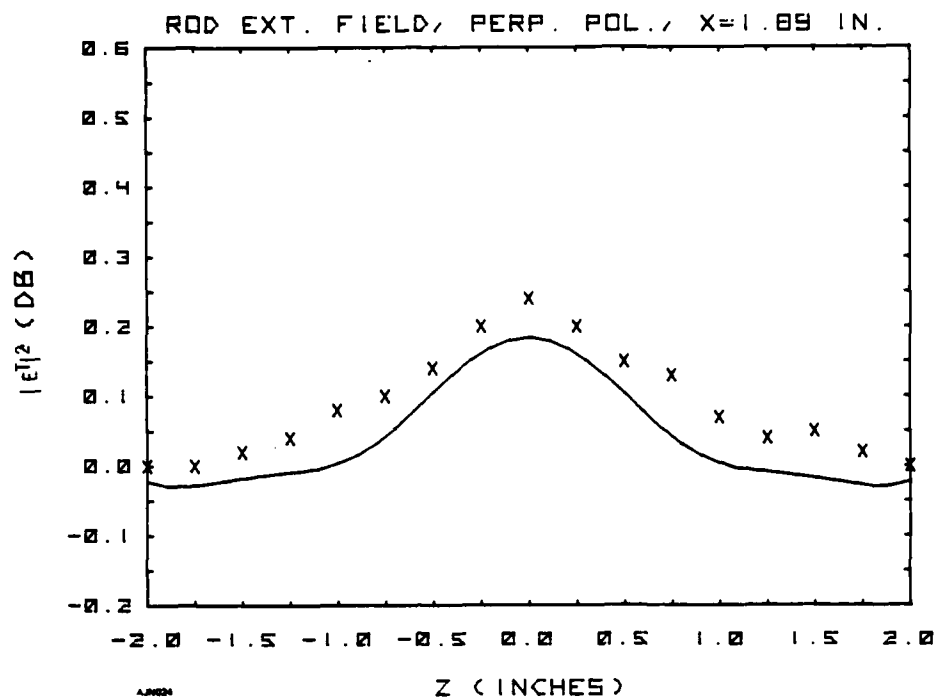


Figure 7-10. As in Figure 7-4, but E^I Perpendicular to Rod and $x = 1.5\lambda$.

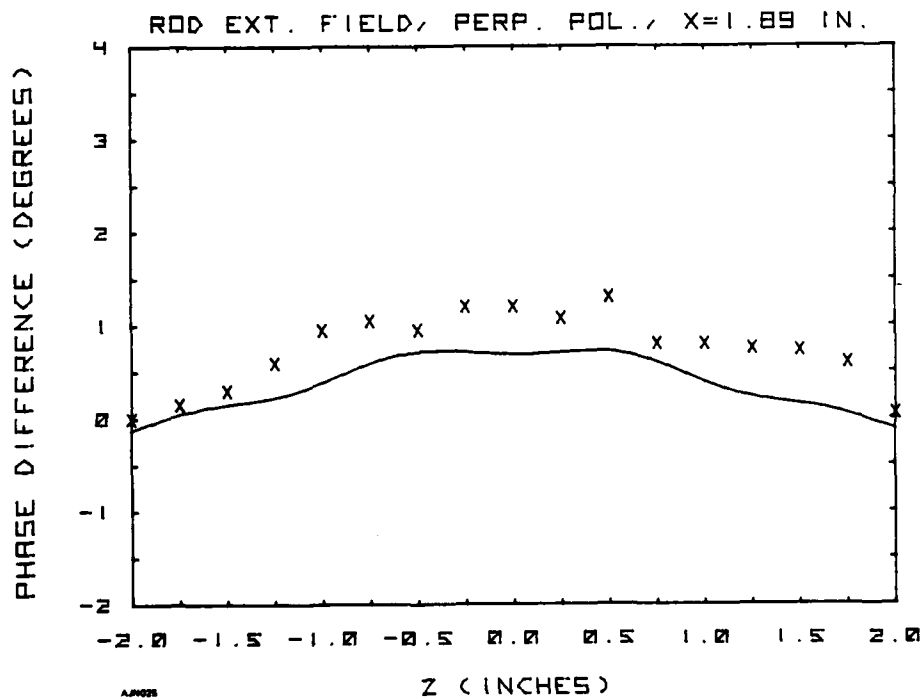
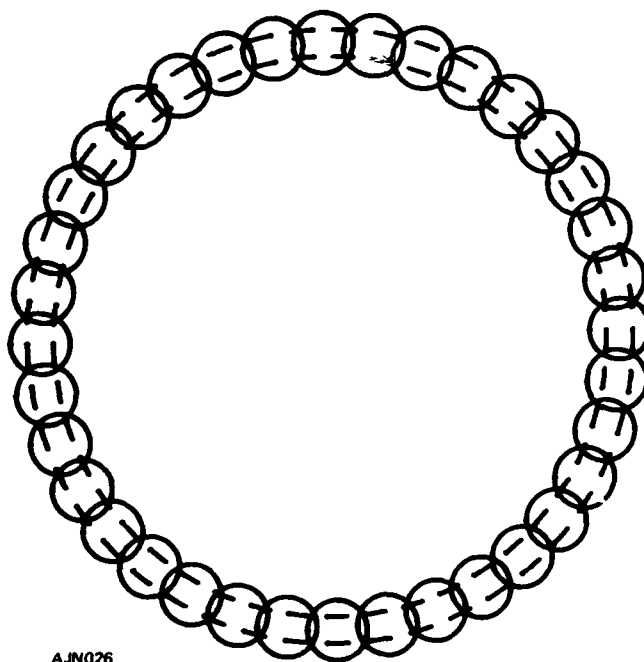


Figure 7-11. As in Figure 7-5, but E^I Perpendicular to Rod and $x = 1.5\lambda$.

7.2 RING

The second example was a dielectric ring ($\kappa = 2.6$) lying in the x-y plane, as shown in Figure 2-1. The incident wavelength was again 1.259". Figure 7-12 shows the ring approximated as 36 overlapping spheres, each having radius 0.0684". Figures 7-13 and 7-14 depict the computed internal fields E_{\parallel} and E_{\perp} as functions of angle around the ring. Figures 7-15 and 7-16 display the computed and measured external field along the ring axis. The agreement is quite good for $z \geq \lambda$, with small discrepancies for $z < \lambda$. However, it should be pointed out that no attempt has been made in the calculations to compensate for the non-isotropic receiving pattern of the field probe. Thus, as the probe moves closer to the scatterer, the solid angle subtended by the scatterer at the probe grows larger, and the effect due to the non-isotropy of the probe becomes more and more pronounced. This non-isotropy in combination with the field disturbances caused by the mere existence of the probe probably suffices to account for the nearfield discrepancies exhibited in Figures 7-15 and 7-16.



AJN026

Figure 7-12. Dielectric Ring (as in Figure 2-1). Approximated by 36 Spheres.
Sphere radii: 0.0684".

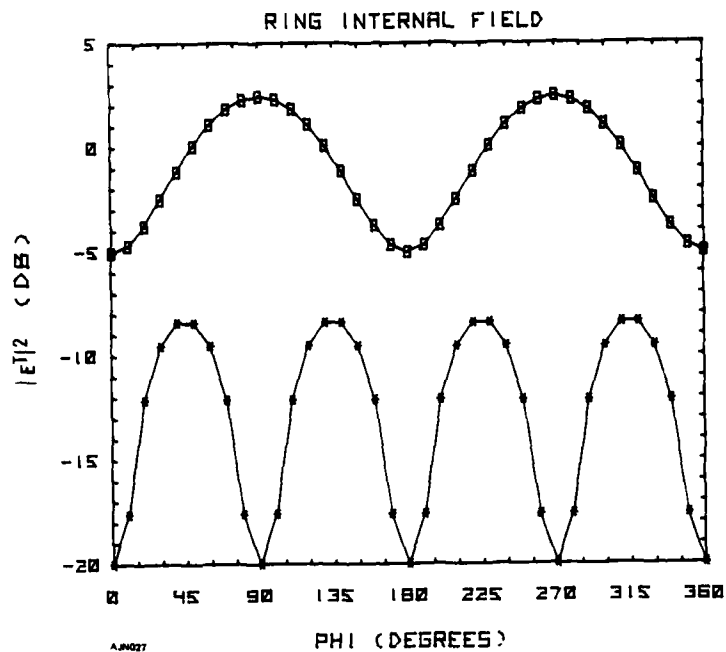


Figure 7-13. Computed Internal Field Intensity as a Function of Azimuth for the Dielectric Ring of Figure 7-12. (O): Component of \underline{E}^T Parallel to \underline{E}^I ; (*): Component of \underline{E}^T Perpendicular to \underline{E}^I .

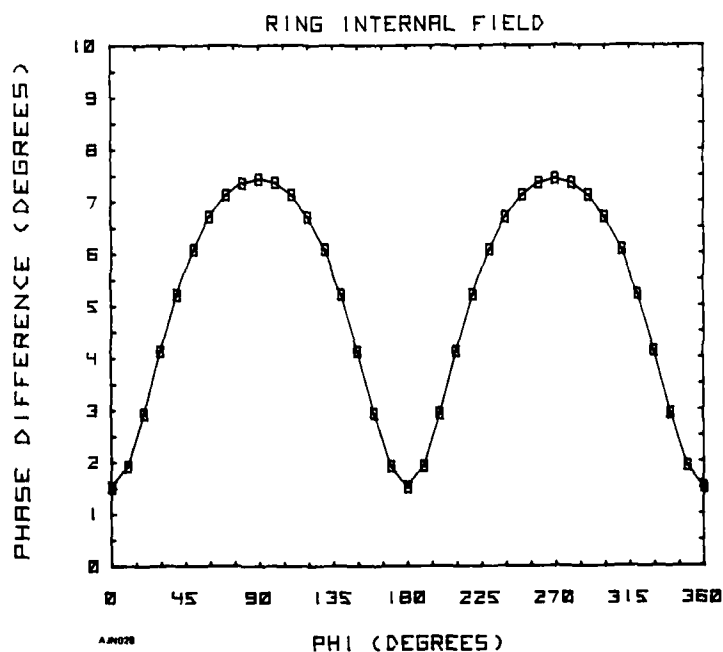


Figure 7-14. Computed Internal Field Phase as a Function of Azimuth for the Dielectric Ring of Figure 7-12. (O): Component of \underline{E}^T Parallel to \underline{E}^I ; (*): Component of \underline{E}^T Perpendicular to \underline{E}^I .

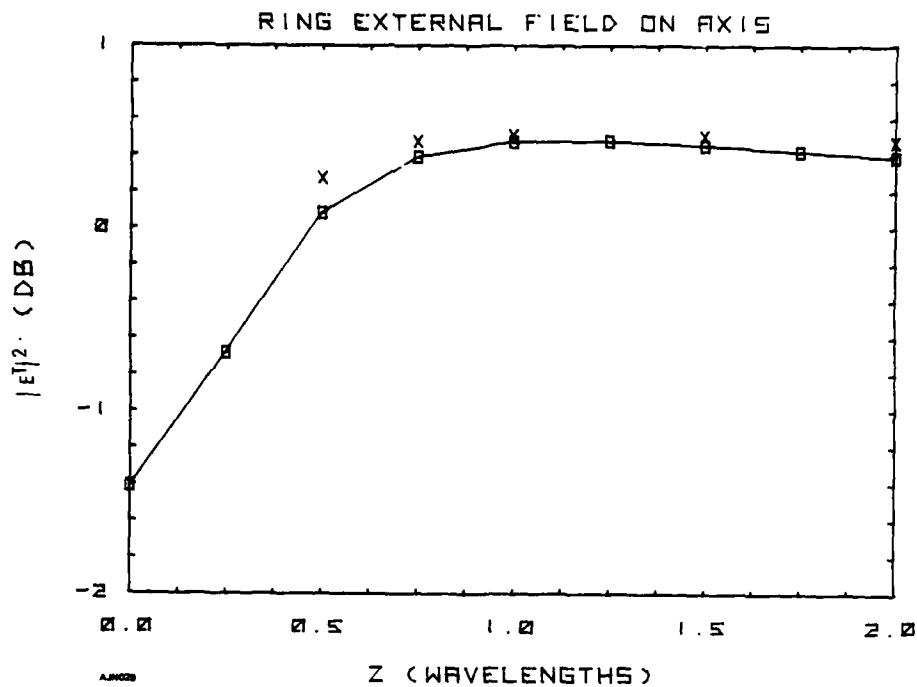


Figure 7-15. Total Field Intensity Behind Dielectric Ring.
(O): Computed; (X): Measured.

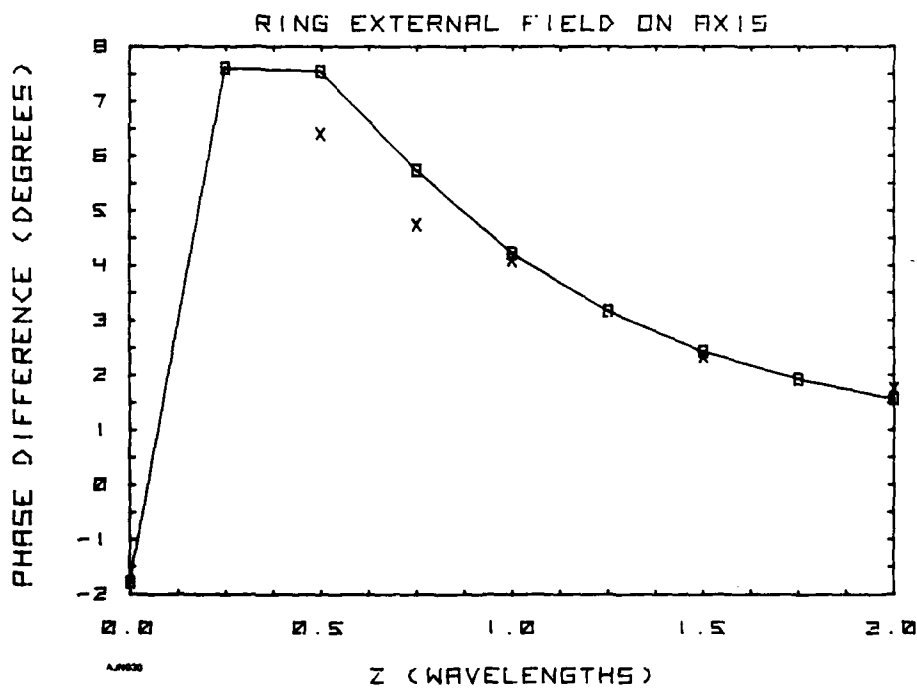


Figure 7-16. Total Field Phase Behind Dielectric Ring.
(O): Computed; (X): Measured.

AD-A106 762

GENERAL DYNAMICS SAN DIEGO CA ELECTRONICS DIV

F/G 17/9

WAVE PROPAGATION THROUGH AXIALLY SYMMETRIC DIELECTRIC SHELLS.(U)

JUN 81 G TRICOLES, E L ROPE, R A HAYWARD

N00019-79-C-0638

UNCLASSIFIED

R-81-125

NL

242

242



END

DATE

FILED

11-81

NTIC

APPENDIX A
EQUIVALENCE OF TENSOR AND SCALAR FORMULATIONS

In Equation 2-19 use Equations 2-9 and 2-10 so that

$$4 \pi \underline{E}^s = \int \left[i \omega \mu_0 \underline{g} \underline{J} + \epsilon_0^{-1} \rho \nabla \underline{g} \right] dV \quad (A-1)$$

The equation of continuity gives $\rho = (i\omega)^{-1} \nabla \cdot \underline{J}$; thus

$$4 \pi \omega \epsilon_0 \underline{E}^s = i \int \left[k_0^2 \underline{g} \underline{J} - (\nabla \cdot \underline{J}) \nabla \underline{g} \right] dV, \quad (A-2)$$

where k_0^2 is $\omega^2 \mu_0 \epsilon_0$, and observe the $\nabla \underline{g} = - \nabla g$.

The second term in Equation A-2 is ¹⁷

$$(\nabla \cdot \underline{J}) \nabla \underline{g} = \sum_{\alpha} \underline{J}_{\alpha} \nabla \cdot \left(\underline{J} \frac{\partial \underline{g}}{\partial x_{\alpha}} - (\underline{J} \cdot \nabla) \nabla \underline{g} \right) \quad (A-3)$$

In the volume integral of Equation A-1 the first term of Equation A-3 can be changed to surface integral. The surface integral vanishes outside a sphere that contains the sources. Therefore, Equation A-2 yields.

$$\underline{E}^s = i (4 \pi \omega \epsilon_0)^{-1} \int \left[k_0^2 \underline{g} \underline{J} + \underline{J} \cdot \nabla \nabla \underline{g} \right] dV \quad (A-4)$$

This expression is given in several references (see e.g., Reference 9).

REFERENCES

1. T. E. Fiscus, E. L. Rope, and G. Tricoles, "Radome Boresight Error From Wavefront Measurements," Proceedings Twelfth Symposium on Electromagnetic Windows, Georgia Institute of Technology, 1974.
2. J. H. Richmond, "Scattering by a Dielectric Cylinder of Arbitrary Cross Section Shape," IEEE Trans. Vol. AP-13, pp. 334-341 (1965).
3. R. A. Hayward, E. L. Rope, and G. Tricoles, "Accuracy of Two Methods for Radome Analysis," Digest IEEE Antennas and Propagation Symposium, June 1979, IEEE Catalog No. 79CH1456-3AP.
4. G. Tricoles and E. L. Rope, "Guided Waves in a Dielectric Slab, Hollow Wedge, and Hollow Cone," Jour. Opt. Soc. Am., Vol. 55, pp. 328-330 (1965).
5. G. Tricoles, E. L. Rope, and R. A. Hayward, "Wave Propagation Through Axially Symmetric Dielectric Shells", General Dynamics Electronics Report R-80-008. Feb. 1980 (Contract N000-19-78-C-0594).
6. G. Tricoles and E. L. Rope, "Scattering of Microwave by Hollow Dielectric Wedges," Jour. Opt. Soc. Am., Vol. 55, pp. 1479-1498 (1965).
7. G. Tricoles, "Application of Ray Tracing to Predicting the Properties of a Small Axially Symmetric Missile Radome," IEEE Trans. Vol. AP-14, pp. 244-246 (1966).
8. J. A. Stratton, Electromagnetic Theory, McGraw-Hill, p. 2 (1940).
9. W. K. Panofsky and M. Phillips, Classical Electricity and Magnetism, Addison-Wesley, p. 210 (1955).
10. Reference 8, p. 464.
11. H. Levine and J. Schwinger, Appendix I, in The Theory of Electromagnetic Waves, M. Kline, ed., Dover, New York (1965).
12. J. VanBladel, IRE Trans. on Antennas and Propagation, AP-9, p. 311 (1961).
13. J. D. Jackson, Classical Electrodynamics, 2nd Ed., p. 395, Wiley, New York, (1975).
14. Reference 8, p. 155.
15. Reference 8, p. 151.
16. E. M. Purcell and C. R. Pennypacker, Astrophysical J., 186, p. 705 (1973).
17. S. Silver, Microwave Antenna Theory and Design, p. 86, McGraw-Hill, New York (1949).

REPORT DOCUMENTATION PAGE		READ INSTRUCTIONS BEFORE COMPLETING FORM
1. REPORT NUMBER Final Report	2. GOVT ACCESSION NO. AD-A106762	3. RECIPIENT'S CATALOG NUMBER 2
4. TITLE (and Subtitle) Wave Propagation Through Axially Symmetric Dielectric Shells.		5. TYPE OF REPORT & PERIOD COVERED Final Technical Report, 12 December 1979 - 30 June 1981
7. AUTHOR(s) G. Tricoles, E. L. Rope, R. A. Hayward		6. PERFORMING ORG. REPORT NUMBER 114 R-81-125
9. PERFORMING ORGANIZATION NAME AND ADDRESS General Dynamics Electronics Division P.O. Box 81127 San Diego, CA 92138		10. PROGRAM ELEMENT, PROJECT, TASK AREA & WORK UNIT NUMBERS 11
11. CONTROLLING OFFICE NAME AND ADDRESS U.S. Naval Air Systems Command, Code 310B Washington, D. C. 20361		12. REPORT DATE June 1981
14. MONITORING AGENCY NAME & ADDRESS (if different from Controlling Office) 12 1 PP		13. NUMBER OF PAGES 89
		15. SECURITY CLASS. (of this report) None
		15a. DECLASSIFICATION/DOWNGRADING SCHEDULE
16. DISTRIBUTION STATEMENT (of this Report) Approved for public release; distribution unlimited.		
17. DISTRIBUTION STATEMENT (of the abstract entered in Block 20, if different from Report)		
18. SUPPLEMENTARY NOTES		
19. KEY WORDS (Continue on reverse side if necessary and identify by block number) radomes, diffraction, scattering, nearfield geometric diffraction theory moment method		
20. ABSTRACT (Continue on reverse side if necessary and identify by block number) Moment method calculations are given and compared with measured data for fields near dielectric slabs, hollow wedges, and hollow cones. A geometric diffraction theory interpretation is developed and quantitatively applied to slabs. Constituent waves including plane, slab-guided, cylindrical, and reflected waves are identified. The research is motivated by radome boresight error.		

147750

